ADAPTIVE AND INTELLIGENT SOFTWARE-RADIO DESIGN FOR ROBUST WIRELESS COMMUNICATIONS IN CHALLENGING ENVIRONMENTS

by

Adam Gannon

September 2018

A dissertation submitted to the
Faculty of the Graduate School of
the University at Buffalo, State University of New York
in partial fulfilment of the requirements for the
degree of

Doctor of Philosophy

Department of Electrical Engineering

To Dad.

Acknowledgments

First and foremost, I would like to express my most sincere gratitude to my advisor and mentor, Dr. Stella N. Batalama. From learning the basics of modulation in her undergraduate Introduction to Communication Systems class to publishing cutting-edge wireless communications research, she has provided invaluable guidance throughout my growth as a researcher. Despite the significant demands of her job first as Chair of the Department of Electrical Engineering at the State University of New York at Buffalo and now as Dean of the College of Engineering and Computer Science at Florida Atlantic University, she takes great effort to make time for meetings even if they must occur very early on Saturday morning!

I am very fortunate for the guidance of Dr. Dimitris A. Pados, formerly the Clifford C. Furnas Professor in the Department of Electrical Engineering at the State University of New York at Buffalo and now a Professor and I-SENSE Fellow in the Department of Computer and Electrical Engineering and Computer Science at Florida Atlantic University. I remain grateful for his detailed discussions, critical feedback, and infectious passion for our work. Finally, I owe my sincere gratitude to Dr. Weifeng Su, Professor in the Department of Electrical Engineering at the State University of New York at Buffalo and member of my committee, for his suggestions and guidance.

Working and studying at UB has been made more enjoyable by having excellent colleagues in the Department of Electrical Engineering, particularly current and former fellow graduate students Sarankumar Balakrishnan, Song-Wen Huang, Yi Cao, Konstantinos Tountas, Emrecan Demirors, Panos Markopoulos, and Nicholas Tsagkarakis as well as Professors Josep Jornet, Zhi Sun, Nicholas Mastronarde, Tommaso Melodia, Uttam Singisetti, and Victor Pogrebnyak. I especially acknowledge my collaborator on several projects, Georgios

Sklivanitis, who can always be counted on for attention to detail, spirited technical debate, and last-minute debugging of hardware and software. I would be remiss not to mention Kimberly Kriz, Bin Chen, Katharine Bartelo, Jason Tillman, and Mary Busch and their essential but often unsung contributions towards keeping the department running. I also appreciate the assistance of Gina Seits and Marilyn Cordy-Burrell at FAU for facilitating the scheduling of meetings with Dr. Batalama over the past year.

I would like to acknowledge our collaborators at the Air Force Research Laboratory, Information Directorate, including Stephen Reichhart, Michael Medley, Ngwe Thawdar, John Matyjas, Scott Pudlewski, and Ulysses Lee and our industry partners Andrew Drozd and Ashwin Amanna from ANDRO Computational Solutions. I greatly appreciate the financial support of the Air Force Research Laboratory for some of our laboratory's work. My graduate studies were financially supported by a fellowship from Moog Inc. and research and teaching assistantships from the State University of New York. I extend my gratitude to these organizations in addition to my teaching assistantship supervisors Professors Elena Bernal Mor and Pao-Lo Liu.

I have been lucky to hold several external internship and research assistantship positions throughout my graduate studies and offer my thanks to Jonathan Peck and Chris Schoneman at SRC, Inc. and Charles Archibald at Delphi Automotive for contributing to my professional growth. I owe special recognition to the Engineering Institute at Los Alamos National Laboratory for the excellent preparation for graduate school, particularly the encouragement of Eric Flynn.

I am especially grateful for the support of my colleagues at NASA Glenn Research Center who have provided a supportive and intellectually challenging work environment throughout several internship rotations. I would like to especially thank my mentors Joesph Downey, Rafael Apaza, and Dale Mortensen, my coworkers in the Communications & Intelligent Systems Division Janette Briones, James Downey, Mike Evans, Gilbert Clark, Rigoberto

Roche, David Chelmins, Marie Piasecki, Gene Fujikawa, David Buchanan, Denise Ponchak, Félix Miranda, and Dawn Emerson, and all the staff at the Pathways program office.

Finally, I would like to thank my family and friends; my gratitude for their unwaivering support extends far beyond what could fit in these pages.

Table of Contents

Chapter 1

Chapter 2

Chapter 3

Cognitive Coexistence Through All-Spectrum Waveform Design **27**

Chapter 4

Chapter 7

Appendix A

List of Tables

List of Figures

Abstract

The proliferation of wireless devices and the communication networks that enable them has created profound societal impact in recent years. As engineers and researchers look to build more capable and reliable communication systems, many questions remain open, such as how to best utilize the limited radio spectrum and how to maximize the efficiency of wireless devices and networks. While terrestrial communication capabilities continue to expand, even more ambitious frontiers remain to be explored towards realizing the vision of connecting humans, machines, and the world's information across land, air, space, and sea. Indeed, a great many transformative applications can be made possible by extending wireless network capabilities now commonplace in terrestrial systems to the oceans, skies, and cosmos. The wealth of information gathered can be made available in real-time and connectivity of people and devices can be enabled anytime, anywhere.

However, legacy technologies and systems are not able to adequately address the challenges related to the unique characteristics of a wireless channel in these environments and the dynamic nature of its conditions. At the same time, increased system complexity makes effective control and decision making by a human operator almost impossible. To enable robust communications, it is imperative that wireless devices are aware of and able to adapt to changing conditions. Such decisions must occur autonomously, without human intervention, in order to adequately respond to time-varying radio environments. The potentially large performance gains realized by autonomous and intelligent adaptation of system parameters are key for the efficiency and resilience of the wireless networks of the future.

This dissertation presents adaptive and intelligent techniques across the physical, medium access control, and network layers that enable cognitive, reliable, and efficient communications in challenging environments. Our implementation platform is software-defined radio. Spectrum access and cross-layer optimization in the presence of multi-user interference are key challenges. Theoretical developments for airborne communications are evaluated through extensive simulation studies and field testing of a hybrid ground-air cognitive radio network. Adaptive techniques to overcome the challenges of underwater acoustic communications are proposed and validated through simulation. Promising directions for agile and efficient space communications are investigated. Intelligence, autonomy, and adaptation are characteristics common to all systems and algorithms proposed.

A Note on Copyright

Portions of this dissertation have been adapted from my research published throughout my graduate school career, which has previously appeared in IEEE publications (namely [1–3]). Chapters containing previously published material are denoted by a footnote on the first page and reprinted images contain a copyright line in the caption. In reference to IEEE copyrighted material which is used with permission in this dissertation, the IEEE does not endorse any of the University at Buffalo, State University of New York's products or services. Internal or personal use of this material is permitted. If interested in reprinting/republishing IEEE copyrighted material for advertising or promotional purposes or for creating new collective works for resale or redistribution, please go to `http://www.ieee.org/publications_standards/publications/rights/rights_link.html` to learn how to obtain a License from RightsLink. If applicable, University Microfilms and/or ProQuest Library, or the Archives of Canada may supply single copies of the dissertation.

Chapter 1

Introduction

Next-generation wireless communication systems will be defined by the efficiency to operate at high data rates with limited spectrum availability and by the resiliency to maintain connectivity in dynamic channel and interference scenarios. Furthermore, future wireless network capabilities will extend far beyond the terrestrial domain into new and challenging environments. The work presented in this dissertation seeks to advance the current state-of-the-art wireless communications in the challenging environments of airborne, underwater, and space with broader implications towards communication system design as a whole.

Civilian air traffic is expected to steadily increase throughout the coming decade, subjecting already crowded aeronautical communication bands to increased congestion [4]. At the same time, ongoing efforts to provide airline pilots and operators with additional real-time information for enhanced situational awareness require improved broadband communication infrastructure [5]. Recent years have seen intense interest in unmanned aerial vehicles (UAVs) for search and rescue, surveillance, hazardous material delivery, emergency communications, and more [6]. Active development is underway to integrate UAVs into the national airspace, requiring highly robust communication capabilities [7].

Yet the airborne environment also presents many challenges. High relative velocities produce large Doppler shifts. High mobility subjects airborne platforms to interference levels that are time-varying and location-dependent [8]. Many compelling UAV applications involving swarm networks and multi-hop ad-hoc routing require highly efficient schemes to handle additional overhead from control information [6]. Networks must adapt quickly to changing topologies and be ready to compensate for disruptions that cause temporary loss of communication with an airborne node [9]. It is clear that adaptation and interference mitigation across several layers of the protocol stack are required to maximize efficiency in this environment.

Many compelling applications arise from enhanced wireless networking underwater. Like in the airborne domain, unmanned systems such as autonomous underwater (AUV) and autonomous surface (ASV) vehicles have a range of applications spanning military surveillance, marine mapping, underwater data collection, search and rescue, and more [10]. At the same time, aquatic sensors providing real-time data are becoming increasingly critical for environmental and public safety applications [11]. Successes in early-warning systems can be expanded to new environments and greatly enhanced with increased networking capability among sensor nodes. As a specific example, consider the harmful algal blooms becoming an all too common phenomenon in the Great Lakes of North America. In 2014, high levels of microcystin, a toxin secreted by algae, forced the city of Toledo, Ohio to warn 500,000 residents against drinking tap water for several days [12]. Though monitoring efforts are in place, enhanced communications could greatly expand their capability, scale, and connectivity resulting in large sensor networks throughout the world's oceans and lakes providing real-time remote monitoring of conditions with accuracy far superior to current methods.

As high frequency radio waves do not propagate far underwater, acoustics is the preferred wireless technology. However, acoustic signals travel at the speed of sound, producing propagation delays many orders of magnitude greater than terrestrial wireless communications. Furthermore, the underwater medium is highly dynamic and characterized by severe multipath reflections, large Doppler spread, and limited bandwidth [13]. Adaptive transmitter and receiver designs are attractive options for this time-varying environment.

Since the first radio signals were bounced off the Echo 1 satellite in 1960, space communications has become an important technology for connecting people and sharing information all over the world. Networks of small communication satellites ("constellations") currently under development hold the promise to greatly expand the availability of high-speed Internet access [14]. Small satellites with inter-satellite links and networking capabilities are also being leveraged for scientific missions in which a constellation or cluster creates a distributed sensor network [15]. At the same time, large spacecraft built for scientific and human exploration are being outfitted with more numerous and increasingly complex instruments which require higher bandwidth communications. As the number of spacecraft throughout the solar system increases, attention is turning to the development of an interconnected "solar system Internet" capable of routing packets through multi-hop routes at interplanetary distances [16].

Links between Earth and space are subject to high path loss, fading from weather, absorption from atmospheric gases, and large propagation delays at high orbits and especially at interplanetary distances [17]. Many frequency bands desirable for satellite communications are also allocated to terrestrial services, requiring sharing and interference mitigation techniques [18]. Though in-space networking holds great promise for more efficient data transfer, it requires the use of protocols specifically designed to route packets across links subject to large delays due to distance and frequent disruptions from blockage [19].

1.1 Cross-Layer Cognitive Radio

Future wireless systems operating both terrestrially and in the environments described above will be defined by the capability to establish efficient communications and maintain robust links despite limited spectrum availability, dynamic channel conditions, and time-varying interference. Traditional wireless devices, with static hardware and inflexible signal processing fail to achieve optimal performance in extreme environments. The work in this dissertation builds upon two transformative concepts in wireless communications: software-defined radio and cognitive radio.

In contrast to wireless devices with inflexible purpose-built hardware, software-defined radio (SDR) implements the majority of its signal processing algorithms in easily-reconfigurable software [20]. A software-defined radio combines tunable analog (front-end) hardware with programmable digital devices (back-end) such as field-programmable gate arrays (FPGAs) and general-purpose processors (GPPs) whose operation can be changed through software updates [1]. Many waveforms can be deployed on the same SDR platform, making the technology ideal for all stages of wireless design: from development to deployment. Most importantly to the work in this dissertation, software-defined radio exposes all parameters of a wireless link to observation and adjustment in response to changing conditions. To take full advantage of this flexibility, the related technology of cognitive radio has been the subject of intense interest in recent years.

As defined by seminal works in the field, a cognitive radio is a software-defined radio capable of learning from and adapting to its operational environment to establish reliable communications and efficiently use spectrum [21, 22]. By itself, a software-defined radio provides only the potential of reconfigurability. Through increasingly complex algorithmic developments a software-defined radio can become aware of its environment, adaptive to changes that effect its performance, and able to cognitively learn from past decisions [23]. Though the last step represents the culmination of Mitola's vision of an ideal cognitive radio (iCR), the spectrum of aware, adaptive, and cognitive radio (AACR) can represent a significant enhancement over current state-of-the-art wireless devices.

The interaction between cognitive radio functionalities at the physical, medium access control, and network layers is a critical consideration for optimal performance. Cross-layer techniques can significantly enhance performance and further progress towards a fully-adaptive and cognitive radio. An important development in this area is all-spectrum cognitive networking: a technique to jointly optimize physical-layer waveforms and network-layer route selection [24]. In this distributed optimization scheme, user transmissions occupy the entire available bandwidth and waveforms are designed so as to mitigate interference between users. Therefore, the scheme is compatible with the "underlay" concept of dynamic spectrum access: in which radio users access spectrum opportunistically provided they limit interference to licensed or priority users operating in these bands [25].

1.2 Dissertation Overview

Chapter 2 discusses in detail how software-defined and cognitive radio can be applied to address next-generation wireless challenges. Extensions of all-spectrum cognitive networking towards practical realization in congested and contested environments are presented in Chapter 3 along with results demonstrating low-complexity waveform design algorithms. Chapter 4 details important development work that takes all-spectrum cognitive networking from simulation through design, development, and deployment. In this section, the first implementation and validation of this cross-layer cognitive radio technology in a large hybrid ground-air testbed is presented. The resilience of the concept is demonstrated by subjecting the network to external physical-layer interference and internal network-layer congestion.

Turning attention to promising techniques in underwater communications, Chapter 5 discusses signal processing techniques for robust underwater acoustic links. A semi-blind receiver based on L1-norm principal component analysis is developed to recover signals in impulsive site-specific noise. An adaptive spread-spectrum system is proposed with a feedback link to update spreading code length to dynamic channel conditions. A receiver based on the auxiliary-vector filter is designed to handle short packets critical to establishing a feedback-based system underwater. Chapter 6 includes a comprehensive discussion of cognitive radio applications in space communications and presents preliminary simulation results in this rapidly developing area. Finally, Chapter 7 provides a summary of contributions, recommendations for future work, and concluding remarks.

Chapter 2

Software-Defined & Cognitive Radio

2.1 Introduction

Software-defined radio (SDR) leverages the flexibility of programmable, software-reconfigurable hardware [20]. In SDRs, the signal processing of communications protocols is performed in reprogrammable devices such as general-purpose-processors (GPPs), digital-signal-processors (DSPs), field-programmable-gate-arrays (FPGAs), or, increasingly, a combination of these devices. There now exists a wide variety of commercially-available SDR platforms and associated software tools that can be used for rapid prototyping and development of novel radio designs. Most importantly, SDR platforms expose channel measurement and waveform parameter adjustment functionalities to real-time software control. Therefore, software-defined radio is a critical enabling technology to the spectrum of aware, adaptive, and cognitive radio.

A large portion of the work presented in this dissertation leverages software-defined radio capabilities for both rapid testing and cognitive radio design. This chapter will provide a comprehensive discussion of software-defined radio architecture and analyze trade-offs among heterogeneous processing options. Existing state-of-the-art SDR platforms and software

---

Portions of this chapter are adapted from the author's published work in [1] (©2016 IEEE), a version of which also appeared in [26].

tools will be discussed and compared with respect to their capabilities and limitations in light of the adaptive and cognitive radio capabilities discussed later in this dissertation. To frame the discussion of cognitive radio in this document, this chapter concludes with an overview of cognitive radio concepts and recent results.

2.2 Software-Defined Radio Architecture

Software-defined radio proposes a paradigm shift from inherently inflexible, dedicated-functionality hardware radio platforms by combining analog static or parameterizable (front-end) circuits and software reprogrammable digital hardware (back-end) components that are easily reconfigurable via software updates. Software-defined architectures are therefore ideal for rapid prototyping, and testing of new military applications and commercial standards. In the context of this work, the term front-end describes the analog signal processing stages between the antenna and analog-to-digital-converters (ADCs) or digital-to-analog-converters (DACs), and the term back-end refers to software re-programmable digital processing platforms such as GPPs, DSPs, and FPGAs.

Figure 2.1 illustrates a generic SDR architecture adopted by the majority of commercially available SDRs, consisting of an analog front-end interfaced with ADC/DAC converters, an FPGA, and a GPP. The SDR front-end consists of analog circuitry responsible for up/down-conversion of analog information signals either directly to passband and baseband, respectively, (homodyne, zero-IF architecture), or to an intermediate frequency (IF) ((super-)heterodyne architecture). Bandpass and lowpass filters, and amplifiers in the front-end are used for signal conditioning. The analog front-end is interfaced with high sample-rate/resolution ADCs that sample the baseband signal, and DACs that convert digital samples to analog waveforms for transmission. As a result, analog passband signals that arrive at the receiver antenna(s) are first bandpass filtered, then amplified via a low-noise-

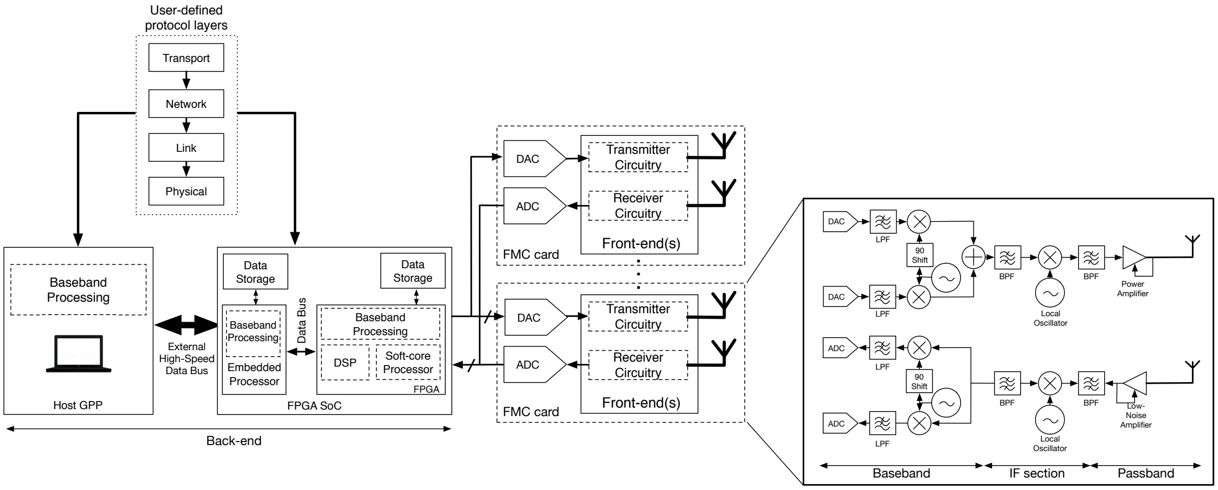

Figure 2.1: Generic software-defined radio architecture. Static analog transmit/receive circuitry (front-end) is interfaced with programmable hardware processing platforms (back-end) through ADCs/DACs. Analog-to-digital-converters (ADCs)/ digital-to-analog-converters (DACs) and analog front-end radio circuitry may be featured under the same compact card, referred to as FPGA mezzanine card (FMC). ©2016 IEEE.

amplifier (LNA), down-converted directly to baseband or optionally to an IF, lowpass filtered, and finally amplitude leveled/power normalized by an automatic-gain-control (AGC) before sampled at the Nyquist rate by the ADC. The reverse process is followed at the transmit chain of the front-end, where incoming complex baseband signals from the DAC are filtered, up-converted, and amplified for passband transmission.

Baseband signal processing on the ADC output and DAC input digital samples is handled by the SDR back-end. User-defined protocol functionalities (Fig. 2.1) at different layers of the network protocol stack exhibit variable latency and memory requirements for multiple communication standards, therefore the wireless system designer may decide to split the execution of certain functionalities to heterogeneous hardware platforms (e.g. GPP, FPGA). High parallelism offered by the FPGA is usually leveraged to accelerate the implementation of computationally-demanding signal processing operations (e.g. filters) on incoming/outgoing data from/to the ADC/DAC at the expense of increased implementation complexity. Digital data can be transferred and long-term stored to an external storage medium such as a secure-digital (SD) card or an on-board synchronous-dynamic-access-memory (SDRAM) for faster access, while upper layer (e.g. link and network layer) functionalities may be handled by either a software co-processor implemented in the FPGA, or an embedded DSP, or a GPP (as depicted in Fig. 2.1). GPPs are well-suited for the implementation of highly branching programs and offer short-development times by exploiting high-level software programming languages. However, real-time operating systems at GPPs offer low resolution in strict real-time data flow constraints. Typical SDR designs implement physical layer functionalities and handle the data at the packet level at a GPP. Digital samples are then transferred to the FPGA through an external high-speed data bus connection (e.g. Gigabit Ethernet). GPPs are either external host-PCs or embedded System-on-Chip (SoC) processors, sometimes even incorporated in the same integrated-circuit (IC) package with the FPGA.

2.3 Software-Defined Radio Challenges in Next-Generation Wireless Systems Prototyping

Next-generation wireless networking protocols and sophisticated network topologies such as multi-user MIMO are difficult to model and test in a software simulation environment. For example, software simulation mostly relies on simplified channel fading models that do not incorporate critical real-world networking conditions or hardware impairments. As a result, researchers can either loosely emulate in software the performance of new signal processing and wireless networking algorithms, or experimentally validate them in heterogeneous multiprocessing hardware platforms consisting of application-specific-integrated-circuits (ASICs), FPGAs, GPPs, and DSPs. Figure 2.2 illustrates the trade-off between reconfigurability and development time for FPGA, ASIC, DSP, GPP, and hybrid GPP/FPGA-centric SDR architectures.

ASIC implementations have a static, application-specific architecture and provide tailored processing units to optimize computational efficiency and power consumption for dedicated functionalities. On the other hand, FPGAs are field-programmable for different applications and provide rapid reconfiguration between different signal processing designs, thus, enabling the development of software programmable SDR platforms at the expense of increased power consumption, and circuit area. Reconfigurable SDR platforms aim to minimize the utilization of ASIC modules such as analog filters, amplifiers, digital down and up converters (DDC and DUC) due to their limited flexibility, or allow their parametrization and runtime reconfiguration through primitive functions that are activated by a processor such as a DSP or a GPP. DSPs offer the best trade-off between processing power and power consumption by providing optimized features especially targeted for digital signal processing operations, e.g. combined multiply-accumulate operations. They are usually embedded in FPGA hardware platforms to efficiently address signal processing tasks that can be pipelined i.e. sequenced and repeated for each sample in a buffer. In addition, GPPs are real-time re-programmable processing alternatives, that can handle processing of a wide variety of applications at low implementation complexity. Furthermore, multi-core architectures of DSPs and GPPs can enhance processing performance by executing multiple operations in parallel.

The rest of this section reviews and discusses the major emerging hardware and software challenges in existing commercially available SDRs, towards accelerating experimental assessment and testing of novel wireless networking protocols. In this context, this chapter studies and classifies SDR systems according to the following criteria: (i) level of flexibility and efficient interaction between analog front-end and digital back-end hardware technologies; (ii) multiprocessing capabilities in heterogeneous hardware platforms; (iii) level of abstraction between software environments and hardware platforms.

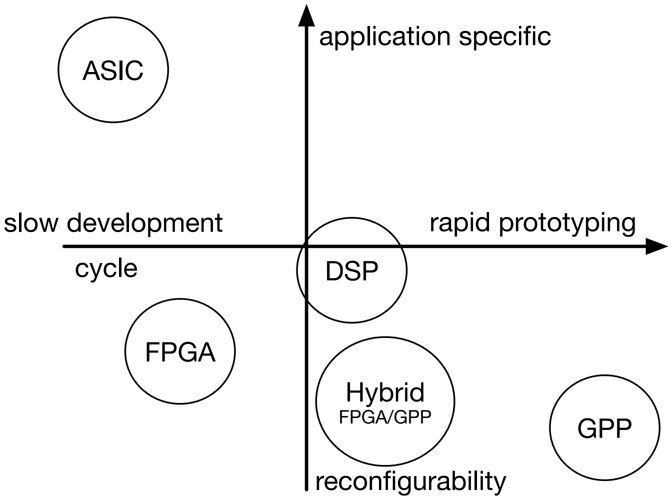

Figure 2.2: Trade-off between reconfigurability and development time for FPGA, ASIC, DSP, GPP, and hybrid GPP/FPGA-centric SDR architectures. ©2016 IEEE.

Analog/Digital Hardware–The analog nature of the transmission medium (i.e. air, water, soil, etc.) as well as the requirements for multi-band support to accommodate multiple standards challenge the design of reconfigurable SDR architectures with respect to both the design of the analog front-end circuitry and their respective physical interface with back-end digital processing platforms. As an example, the (super)-heterodyne transceiver architecture depicted in the circuitry design of Fig. 2.1, fails to reconfigure its fixed narrowband components, such as channel selective filters, to meet the broad-band requirements of multiple standards. On the other hand, the homodyne (zero-IF) transceiver architecture minimizes the number of analog (fixed) components and is a flexible design alternative to the (super)-heterodyne architecture at the expense of increased baseband interference and phase noise (DC offset due to local oscillator leakage and IQ imbalance, respectively) that can be partially compensated for in the digital domain. Flexible receiver design implementation with minimal analog components requires ADCs with high dynamic range, to be able to detect weak desired signals, in the presence of possibly strong undesired in-band signal interference. Furthermore, the effective (useable) bandwidth of the SDR system of Fig. 2.1 is defined as the minimum of (i) the radio's analog bandwidth which should not exceed the ADC/DAC sample rate, (ii) the FPGA processing bandwidth that depends on the FPGA clock rate, and (iii) the host-GPP bandwidth. Typical commercial SDR platforms either include a high-speed 1/10 Gigabit Ethernet (GigE) connection to address the host GPP-FPGA communication or implement FPGA-based soft-core processors or select wireless-focused embedded hard processors (e.g. ARM). In this way, the FPGA is able to handle GPP-like branching logic. Therefore, performance efficiency for multiple standards entails effective interaction and data transfer optimization between different hardware platforms at the SDR back-end.

Heterogeneous Multiprocessing−Multiprocessing is an SDR intrinsic requirement that aims to enhance SDR computational efficiency by off-loading complex signal processing operations such as finite-impulse-response (FIR) filtering or fast Fourier transform (FFT) to heterogeneous hardware platforms. However, software development of such architectures suffers from increased implementation complexity and lack of a standard methodology for partitioning the implementation of signal processing functionalities to heterogeneous hardware platforms [27]. As an example, GPPs or DSPs have memory architectures well-suited for streaming data and rely on sequential execution of a single instruction stream. They are single-instruction-multiple-data (SIMD) units where each processor is constrained to execute the same instruction at a single program but operate over multiple data streams in parallel. Therefore, GPPs and DSPs are suitable for simple computational tasks such as modulation/demodulation and encoding/decoding, higher level logic applications, network and medium access layer functions. On the other hand, FPGAs are well-suited for implementation of logical functions that can be separated and run simultaneously or for execution of tasks that use non-standard data-type representations (i.e. 12 or 14-bit ADC/DAC), however, they exhibit increased development time and complexity. Data-type consistency, sampling rate adaptation, and resource mapping and scheduling of software applications for heterogeneous hardware are additional architectural considerations in the development of heterogeneous multiprocessing platforms. Exchanging a common data stream between multiple hardware architectures that use different data-type representations say, for example, between a GPP that utilizes floating-point SIMD instruction sets, and a DSP or FPGA that uses fixed-point representations requires data-type conversions. Data-type conversions, for example, conversion of a 12/14-bit ADC output to 16-bit short at GPP input lead to increased processing load. Furthermore, sampling rate adaptation is necessary for interfacing multiple sub-systems with different clock rates as well as for fine tuning to the sampling rate of multiple communication standards. Implementation of reconfigurable sampling rate adaptors suffers from the design of highly dynamically adaptive and computationally efficient FIR filters. Thus, existing SDR architectures assign the implementation of sampling rate adaptors to the FPGA. Finally, automatic instead of ad-hoc resource mapping for heterogeneous multiprocessing, may enable adaptation of protocol execution speeds that can be traded-off during runtime to satisfy pertinent latency requirements of the specific communication standard.

Hardware Abstraction−The majority of existing SDR software tools are tightly integrated with specific hardware platforms with little or no abstractions available to the wireless system designer. As a result, optimization of the system design flow at high level depends on software-hardware co-design for objects executed in processors and FPGAs, respectively. As an example, a researcher willing to develop and experimentally evaluate a complex modulation waveform or channel/source coding scheme is required to develop and optimize signal processing components, as well as to decide on the optimal execution architecture according to the available hardware platforms and the respective software tools. Nevertheless, the implementation of abstract hardware application-program-interfaces (APIs) that offer granular control and separate the execution architecture from signal processing may allow trading off prototyping time for optimization of platform resources and vice versa. In addition, the availability of dedicated software tools for particular hardware platforms, in combination with hardware abstractions may give the opportunity to the wireless system designer to integrate optimized intellectual property (IP-protected) processing components developed by domain specialists or third party developers, and rely only on abstract characteristics such as memory use, and execution speed. Multiple levels of granularity in hardware control may also accelerate the transition from simulation to prototyping by providing bit level visibility into the design and the capability to quickly test its functional behavior. FPGA software development will definitely benefit from such abstractions as, currently, long compile times, synthesize times, and place-and-route times are prohibitive for trial-and-error performance assessment of new wireless designs.

Table 2.1: Software/Hardware compatibility for state-of-art commercial SDR platforms.

	Ettus/NI USRP		**Nutaq**		**Mango WARP**		**Per Vices**		**Epiq**	
	GPP	**FPGA**	**GPP**	**FPGA**	**GPP**	**FPGA**	**GPP**	**FPGA**	**GPP**	**FPGA**
GNU Radio	●	N/A	●	N/A	○	N/A	●	N/A	●	N/A
Mathworks	●	○	●	●	●	●	○	○	○	○
NI LabVIEW	●	●	○	○	○	○	○	○	○	○

●: Compatible option; ○: Incompatible option; N/A: option is not available.

2.4 Commercial Software-Defined Radio Platforms

For small-scale laboratory testbed setups, commercially available SDR platforms offer low-cost hardware and software solutions for rapid experimental assessment of programmable wireless networks. This section discusses the strengths and limitations of both software frameworks and hardware architectures with respect to rapid prototyping and testing of next-generation wireless systems. A compatibility overview between the available software tools and heterogeneous SDR platforms is provided in Table 2.1.

2.4.1 Software Frameworks

GNU Radio−GNU Radio is an open-source software framework that follows a component-based design, where signal processing chains are broken into primitive components/blocks, therefore enabling code re-usability and rapid block reconfiguration. Each block is assigned to a dedicated processor thread, while data exchange between blocks is achieved through shared memory buffers. GNU Radio applications are only supported by GPPs (see Table 2.1) as well as embedded processors that support floating point SIMD instruction sets. New GNU Radio applications, called flow graphs, are programmed in Python and C++. The API of the GNU Radio framework enables integration of optimized signal processing blocks (GNU Radio IP) such as modulators and demodulators. The framework allows simulation of the performance of new physical layer communication designs through an XML-based graphical-user-interface (GUI), called GNU Radio Companion (GRC). With respect to performance acceleration of pure GPP-centric designs, GNU Radio provides a programming tool, named VOLK (vector-optimized library of kernels) [28], that enables vectorized mathematical operations and is independent of the processor's architecture. VOLK offers an abstraction layer to hardware-specific SIMD implementations which vary across different processor families and vendors. Packet-based processing in upper layers is enabled by stream tagging and asynchronous message passing software APIs. More specifically, stream tags enable sample streams to carry metadata information (e.g. information on packet boundaries), while message passing enables asynchronous parameter reconfiguration in flow graph blocks regardless of their location in the data flow (upstream or downstream blocks). As a result, GNU Radio provides rapid software simulation and testing of new GPP-centric wireless system designs.

Table 2.2: Ettus USRP Daughterboards.

Daughterboard	**Function**	**Freq. Low**	**Freq. High**	**Max RF Bandwidth per channel**
UBX[*]	Transceiver	10 MHz	6 GHz	40 MHz 160 MHz
WBX[*]	Transceiver	50 MHz	2.2 GHz	40 MHz 120 MHz
CBX[*]	Transceiver	1.2 GHz	6.0 GHz	40 MHz 120 MHz
SBX[*]	Transceiver	400 MHz	4.4 GHz	40 MHz 120 MHz
XCVR	Transceiver[†]	2.4 GHz 4.9 GHz	2.5 GHz 5.9 GHz	36 MHz (RX) 48 MHz (TX)
Basic RX	Receiver	1 MHz	250 MHz	100 MHz
Basic TX	Transmitter	1 MHz	250 MHz	100 MHz
LFRX	Receiver	DC	30 MHz	30 MHz
LFTX	Transmitter	DC	30 MHz	30 MHz
DBSRX2	Receiver	800 MHz	2.3 GHz	60 MHz
TVRX2	Receiver	50 MHz	860 MHz	10 MHz

Note[*]: The N-series family of USRPs is compatible only with the 40 MHz bandwidth daughterboards, while the X-series can support both 40 MHz and 120/160 MHz daughterboards.

Note[†]: TVRX2 supports half-duplex operation only.

Table 2.3: State-of-art tabletop SDR platforms.

SDR Platform	**Hardware**	**Number of TX/RX Ant.**	**Freq. Low**	**Freq. High**	**Max. RF BW per IQ channel**	**ADC speed (MS/s, bits)**	**DAC speed (MS/s, bits)**	**Ext. Data Bus Host Connections**	**Max Host Throughput**
Ettus USRP B−*	Xilinx Spartan 6 FPGA with integrated radio chipset	2/2	70 MHz	6 GHz	56 MHz	61.44, 12	61.44, 12	USB 3.0	1.96 Gbps
Ettus USRP N−*	Xilinx Spartan 3A-DSP FPGA	1/1	DC	6 GHz	40 MHz	100, 14	400, 16	GigE	0.8 Gbps
Ettus USRP X−*	Xilinx Kintex 7 FPGA	2/2	DC	6 GHz	160 MHz	200, 14	800, 16	Dual 1/10 GigE PCIex4	6.4 Gbps
Nutaq PicoSDR†	Xilinx Virtex 6 FPGA	2/2	300 MHz	3.8 GHz	28 MHz	80, 12	80, 12	Dual GigE PCIex4	6.4 Gbps
Nutaq ZeptoSDR	Xilinx Zynq 7020 SoC (Dual-core ARM Cortex-A9)	1/1	300 MHz	3.8 GHz	28 MHz	80, 12	80, 12	GigE	0.8 Gbps
Mango WARP v3	Xilinx Virtex 6 FPGA	2/2	2.4 GHz 4.9 GHz	2.5 GHz 5.8 GHz	40 MHz	100, 12	170, 12	Dual GigE	0.8 Gbps
Epiq Maveriq	Dual-core Intel Atom processor Xilinx Spartan 6 FPGA	2/2	70 MHz	6 GHz	50 MHz	50, 12	50, 12	GigE Dual USB	0.8 Gbps
Epiq Sidekiq	Xilinx Spartan 6 FPGA	1/2	70 MHz	6 GHz	50 MHz	61.44, 12	61.44, 12	PCIex1 USB 2.0	1.6 Gbps
Per Vices Noctar	Altera Cyclone IV FPGA	1/1	100 kHz	4.4 GHz	200 MHz	125, 12	250, 16	PCIex4	6.4 Gbps
Per Vices Crimson	Altera Arria V ST SoC (Dual-core ARM Cortex-A9 MP)	4/4	100 kHz	6 GHz	322 MHz	370, 16	2500, 16	Dual 1/10 GigE USB	6.4 Gbps

Note*: Larger scale antenna system setups with USRP X or N-series require additional hardware such as an OctoClock(-G) which is a clock distribution system for coherent operation of multiple SDRs under external clock reference.

Note†: PicoSDR is also available in a 4 × 4 MIMO antenna configuration and a 2 × 2 embedded-PC (Quad-core i7) configuration.

Table 2.4: Portable small-form-factor SDR platforms.

SDR Platform	**Hardware**	**Number of TX/RX Antennas**	**Freq. Low**	**Freq. High**	**RF BW per IQ channel**	**ADC speed (MS/s, bits)**	**DAC speed (MS/s, bits)**	**Form Factor**
Ettus USRP E310	Xilinx Zynq 7020 SoC (Dual-core ARM Cortex-A9) with integrated radio chipset	2/2	70 MHz	6 GHz	56 MHz	61.44, 12	61.44, 12	133 × 68 × 26.4 mm
Epiq Matchstiq S10	Xilinx Spartan 6 FPGA Quad-core ARM Cortex-A9	1/1	70 MHz	6 GHz	50 MHz	61.44, 12	61.44, 12	114.3 × 40.6 × 27.9 mm

Mathworks/LabVIEW−Mathworks provides rapid radio prototyping solutions [29] by building a bridge between simulation at the Simulink environment and execution on heterogeneous hardware platforms, such as an FPGA interfaced with a DSP or GPP. More specifically, Simulink follows a graphical, high-level modeling design approach that enables fast building and simulation of new designs based on Mathworks libraries. Simulation models are then linked to C-based DSPs or GPPs through the Mathworks RealTime Workshop tool that enables automatic translation of Simulink simulation models into C-code. Simulink has the ability to interface with System Generator, a Xilinx DSP design tool reducing this way the FPGA software development time. System Generator contains platform-specific sets of Xilinx FPGA IP blocks such as FFT, filters, and memory blocks that are guaranteed to exhibit equivalent cycle accuracy to the IP blocks available at Simulink. Mathworks, therefore, provides the required hardware abstractions to the SDR system designer to effectively integrate heterogeneous processing elements at the Simulink model-based environment and thus, accelerate transition from simulation to real-world testing. However, the available hardware APIs are constrained by the FPGA provider and technology. Another Mathworks tool that requires no prior experience with low-level FPGA or register-level (RTL) programming is HDL (hardware-description-language) coder. The HDL coder enables automatic conversion of floating-point MATLAB or Simulink simulation models into fixed-point FPGA designs that are ready to be synthesized. Similar programming approaches are followed by the LabVIEW software tools, which target rapid development of heterogeneous multiprocessing system designs that is hybrid GPP-FPGA-centric architectures restricted to Ettus/National Instruments SDR platforms (Table 2.1).

2.4.2 Hardware Architectures

Ettus/NI–Ettus/National Instruments (NI) Universal-Software-Radio-Peripherals (USRPs) are a family of heterogeneous hardware SDR platforms. They are classified into the Networked (N)-series, the Bus (B)-series, the Embedded (E)-series, and the X-series. USRP N- and X-series consist of an FPGA-based motherboard that is interfaced with a single-input-single-output (SISO) daughterboard and multiple daughterboard(s) (MIMO capable), respectively, through high sample rate ADCs and DACs. Table 2.2 lists the frequency range (DC-6.0 GHz) and bandwidth capabilities (10 MHz – 160 MHz) of Ettus daughterboards, which allow for flexible, interchangeable analog front-end circuitry for a variety of applications. FPGA-based signal processing designs are either controlled by host GPPs via external high-speed data bus connections (Table 2.3, USRP X, N, and B-series), or by soft-core processor cores implemented at the FPGA (e.g. 32-bit AeMB, MicroBlaze soft-processor cores), or by wireless-focused embedded (SoC) processors such as ARM Cortex-A9, that enable small-form-factor, portable SDR solutions (Table 2.4, USRP E310). Transceiver architectures such as homodyne, or (super)-heterodyne vary across different daughterboards, while ADC, DAC sample rates and bit resolutions vary across different models of the USRP-series. The USRP family is compatible with the majority of software frameworks as seen in Table 2.1 through the USRP-Hardware-Driver (UHD) software API that acts as a host communication driver for controlling Ettus SDRs. Furthermore, Ettus introduces a novel Network-on-Chip mechanism (RFNoC) [30], which enables integration of heterogeneous processing components into a GNU Radio flow graph by providing a standard method for consistently routing data and distributing processing throughout complex heterogeneous hardware platforms (i.e. FPGA and GPP). As a result, a researcher is able to minimize development time by integrating modular IP blocks that are executed in heterogeneous hardware. At the same time, he is able to maintain system design flexibility during runtime for performance demanding protocols by moving timing critical and computationally complex functionalities (e.g. lower medium access control and physical layer) at the FPGA, and implementing high-level control (e.g. upper medium access control) functionalities at the GPP. However, testbed requirements pertinent to specific applications entail proper selection and combination of daughterboards, USRP hardware back-end, and software.

Nutaq−Table 2.3 depicts two heterogeneous hardware SDR platforms provided by Nutaq, called PicoSDR (FPGA interfaced with an embedded-PC or host-PC) and ZeptoSDR (SoC-FPGA platform). Instead of using interchangeable analog front-ends or integrated radio chipsets, Nutaq SDRs use an FPGA mezzanine card (FMC) radio card solution that features ADCs/DAcs on the same compact card with analog front-end circuitry. The FMC card's transceiver follows a homodyne architecture with software selectable bandpass and baseband filters which enable easy runtime adaptation of the analog front-end to multiple communication standards. Furthermore, the separation of SDR back-end from the ADC/DAC and front-end circuitry enables hardware interoperability to deal with challenges imposed by different channel environments, on the condition that software APIs are backwards compatible with different analog components. Nutaq provides an FPGA framework for embedded applications development (board-software-development-kit (BSDK)) that includes custom-built hardware IPs and software APIs to enable efficient interaction with both Mathworks and GNU Radio software tools. In addition, Nutaq provides a set of custom blocks to control and handle real-time data exchange between the host or embedded processor and FPGA, therefore enabling easy synthesis and testing of heterogeneous multiprocessing designs through the Simulink's model-based design approach.

Others−Tables 2.3 and 2.4 present additional tabletop and small-form-factor SDR platforms. Particularly, the third revision of wireless-open-access-research-platform (WARP) provides an FPGA-based SDR architecture with two integrated ADC/DAC and homodyne radio transceiver chipsets. The WARP platform allows expansion to four radio transceivers through FMC expansion ports, while rapid software development of new wireless designs is enabled through the WARPLab framework. WARPLab provides online and offline processing capabilities by allowing rapid physical layer prototyping with MATLAB at the host-PC. Real-time online processing requires user modifications to existing WARPLab reference designs, which are implemented in MATLAB and System Generator. Epiq provides low-power, portable SISO and MIMO-capable SDR platforms with proprietary IPs to reduce development time. More specifically, Maveriq's package features an FPGA interfaced with two homodyne wideband radio transceivers, an embedded Intel processor and an internal hard drive for recording and playback operations. Sidekiq and Matchstiq are small-form-factor, SISO-capable alternatives that provide host and embedded multi-core processing capabilities, respectively. Per Vices offers both a SoC-based wideband SDR platform (Table 2.3, Crimson) equipped with four integrated homodyne radio transceivers, as well as a low-cost, peripheral-component-interconnect-express (PCIe)-based alternative (Table 2.3, Noctar), that can be controlled and re-programmed by custom web or Python-based GUIs. Both Epiq and Per Vices SDR platforms can be interfaced with GNU Radio, however, they currently lack the software abstractions to accelerate complex algorithmic developments on either the FPGA or GPP.

2.5 Overview of Cognitive Radio

Cognitive radio (CR) has generated intense research interest primarily for terrestrial wireless applications. As defined by seminal works in the field, cognitive radios are capable of adjusting to and learning from their environments to establish reliable communications and efficient use of spectrum [21,22]. A significant aspect of cognitive radio is the ability to access radio spectrum dynamically [31,32]. In contrast to static frequency allocations commonplace today, dynamic spectrum access allows opportunistic sharing of spectrum among users. A common scenario considers lower priority ("secondary") users opportunistically accessing shared spectrum in the presence of higher priority ("incumbent" or "primary") users who may hold a license for the band of interest. Access between users of equal priority ("co-primary") has also been studied. By allowing secondary transmissions in unused or underutilized bands, radio spectrum (a limited natural resource) can be utilized more efficiently. Practical realization of dynamic spectrum access requires obtaining knowledge of a primary user's transmissions though explicit cooperation, spectrum sensing, or interference measurements [33].

However, the cognitive radio concept includes capabilities not only for spectrum access, but at all layers of the protocol stack. Cognitive radio can be used to dynamically adapt physical layer parameters such as transmit power, modulation, error correcting codes, or data rate to observed conditions in the communication environment. Cognitive networks, comprised of many cognitive radios with dynamic and adaptive routing capabilities, have also generated significant interest [34].

2.5.1 Enhancing Spectral Efficiency Through Dynamic Access

Dynamic spectrum access in cognitive radio is generally organized into three paradigms: overlay, underlay, and interweave [25]. In interweave schemes, secondary users search for and opportunistically transmit over "white-spaces" or "spectrum holes", spectrum currently unoccupied by primary users. Secondary transmissions may use several non-continuous spectrum holes [35]. The secondary system generally transmits with high power and must immediately cease transmissions if the primary user resumes transmission. In contrast, underlay schemes coexist at the same time and frequency as primary users provided they keep interference levels at all primary users below a predefined tolerable threshold, or "interference temperature". Underlay transmissions in so-called "gray spaces" will typically be of wider bandwidth, lower power, and designed so as to mitigate interference to the primary [36]. Finally, in overlay schemes the secondary will compensate for the interference caused to primary systems by using its own equipment to retransmit or amplify transmissions from primary users. To do so, secondary systems require cooperation with primary users or at least a priori knowledge of their signal parameters.

In each case, the secondary system must acquire some knowledge of the primary system. As a starting point, spectrum measurements may be combined into a radio environment map or spectrum database showing the locations of primary transmitters and signal strength at increasing distance [37]. A secondary user with access to a radio environment map, either locally or through a remote database, will focus its attention on channels that are known to be infrequently used or present minimal interference. However, spectrum database use alone may not be enough to gain sufficient knowledge of primary users. Explicit cooperation with primaries [38] or notification of spectrum access opportunities through a shared database [39] is an enhancement allowing more control over spectrum access.

To properly assess spectrum occupancy, many cognitive radio systems gather up-to-date information on the radio frequency (RF) environment through spectrum sensing [40]. A wide variety of sensing techniques to be executed at a secondary node have been explored in the cognitive radio literature. Furthermore, cooperative spectrum sensing may be used to combine the sensing results of many nodes at a fusion center [41]. Cooperative sensing among geographically distributed nodes can improve the probability of detecting primary transmitters that may not be overheard at all nodes in the secondary system (a type of hidden node problem often called the "hidden incumbent" problem) [42]. A practical example of database and distributed spectrum sensing deployed in an interweave cognitive radio system is the IEEE 802.22 cognitive wireless regional area network (WRAN) standard which opportunistically uses white spaces in the terrestrial TV broadcast spectrum [43].

2.5.2 Beyond Dynamic Access: The Ideal Cognitive Radio

In Haykin's terminology in [22], a cognitive radio is "brain-empowered", capable of not only reacting to its environment but of learning from it and improving future communications. In [44] Mitola describes a radio with the ability to observe, orient, plan, decide, act, and learn. Thus, the application of machine learning to better control radio parameters is in integral part of a radio which is fully cognitive, sometimes called an ideal cognitive radio (iCR) or a "Mitola radio". Machine learning is of intense interest in the fields of computer vision and robotics, to name a few, and has generated a significant body of research in recent years. Of particular interest to cognitive radio use are neural networks [45, 46] and reinforcement learning [47, 48].

Since a fully cognitive radio would be capable of intelligently adjusting all operational parameters, its capabilities extend beyond dynamic spectrum access. In modern protocols each point-to-point link has many parameters that could be dynamically adjusted including modulation, error correction coding, transmit power, and data rate. Further, intelligence can be applied at all layers of the protocol stack including making routing decisions or resource allocation and system-wide management. Following this line of thought, Fig. 2.3 provides a hierarchy of cognitive radio techniques organized by the scale of application. Each radio must analyze and gain access to radio spectrum. Once the physical transmission medium has been accessed, a pair or cluster of radios can begin communicating (and intelligently adjusting link parameters). With a cognitive radio network of point-to-point links formed, cognition can be applied to routing and other networking tasks. Finally, cognitive radio techniques

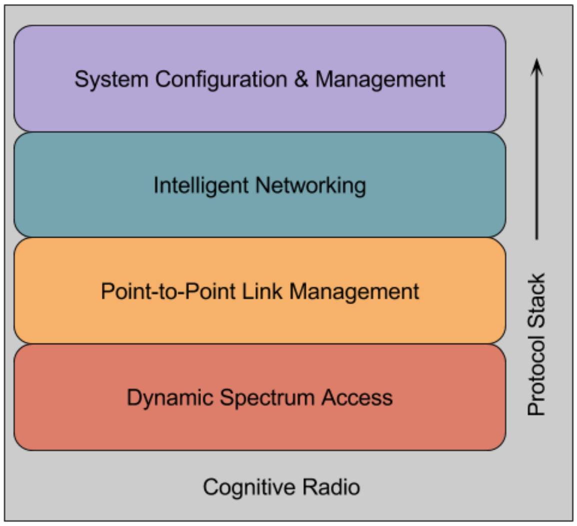

Figure 2.3: Cognitive radio functionalities encompass all layers of the protocol stack, including but not limited to dynamic spectrum access.

can be integrated into an entire system of networks. This hierarchy bears resemblance to the Open Systems Interconnection (OSI) model, though promising performance improvement has been demonstrated with cross-layer designs which jointly optimize parameters across several layers [24, 49].

Mitola describes the progression from radios that are *aware* of their environment to those which can *adapt* to it before finally integrating learning and improvement from past actions to become *cognitive* [23]. Therefore, work in this dissertation will consider research on the spectrum of aware, adaptive, and cognitive radio (AACR). In order to transition radio systems from inherently inflexible to fully cognitive, the radio platform must include “meters” to read and “knobs” to turn [50]. Thus, building a fully realized iCR will require many enabling technologies which may themselves yield improvements on the state-of-the-art even before the integration of cognition.

Chapter 3

Cognitive Coexistence Through All-Spectrum Waveform Design

3.1 Introduction

Though cognitive radio has been extensively studied in the literature, most work independently considers the optimization of spectrum access, physical link parameters, and network route selection. These approaches fail to account for the inherent interdependencies between the physical (PHY), medium access control (MAC), and network (NET) layers of the protocol stack. Therefore, cross-layer joint optimization frameworks can provide significant performance increases over state-of-the-art cognitive radio techniques.

The theoretical foundation of the work presented in the first half of this dissertation is a joint PHY/NET optimization scheme presented in [51], which builds upon the concept of dynamic back-pressure [52]. The authors prove the formulation is throughput optimal, in the sense that network queues are kept finite for any traffic level within the network capacity region. More specifically, the algorithm first assigns physical-layer resources to maximize the capacity of each link in the network. This can be power allocation or, more generally, any

---

Portions of this chapter are adapted from the author's published work in [2] (©2018 IEEE), a version of which also appeared in [26].

combination of PHY-layer parameters which increases the signal-to-interference-plus-noise ratio (SINR) and therefore the Shannon capacity of the link. Differential backlogs, denoting the difference in queue size between a source node and potential destination node, are calculated. Routes are assigned to maximize the weighted sum of differential backlogs with weights given by the optimized capacity of the link.

The integration of spectrum access into the cross-layer optimization problem stems from the notion that spread-spectrum code-waveforms (spreading codes) can be designed to minimize mutual interference between links [36]. In all-spectrum cognitive networking [24], time and frequency is treated as one unified resource. Each network node accesses spectrum whenever it has data to transmit and occupies the entire available bandwidth. Interference between nodes operating at the same time and frequency is mitigated by waveform design. More specifically, each link operates with a binary antipodal spread-spectrum code-waveform calculated at the receiver from local spectrum sensing measurements. The code-waveform is designed to maximize SINR for all links in the secondary network while keeping interference to all nodes in the primary network below a predefined threshold ("interference temperature"). Each sending node in the network calculates the differential backlog to each candidate next-hop receiving node. The route which maximizes the product of capacity and differential backlog is selected as the next-hop.

This chapter will begin with the original all-spectrum signal model in Section 3.2. The goal of this formulation is to maximize the throughput of a secondary network while maintaining interference to users of a primary network below a threshold. To begin, it is assumed that all users employ spread-spectrum signals and that the code-waveforms of all secondary and primary users are perfectly known. Section 3.3 discusses a revised formulation of the original model in which primary user signals may be wideband (spread-spectrum) or narrowband (non-spread) and unknown to secondary users. While the scenarios above consider congested spectrum, Section 3.4 will prove the same optimization problem can be used in contested spectrum. Rather than a primary network, this model considers a PHY-layer interference source intentionally trying to disrupt secondary transmissions. The goal of the secondary network is to maintain connectivity by avoiding interference. Section 3.5 discusses the code-waveform design process itself and presents results comparing waveform design algorithms. Finally, Section 3.6 presents an extension of the signal model to secondaries with multiple antennas using a unique code-waveform per antenna for additional diversity.

3.2 All-Spectrum Cognitive Networking Model

A general representation of the network of interest is presented in Fig. 3.1. Each network node is responsible for forwarding its own traffic and the traffic of neighboring nodes. The sending node TX_1 must optimize the capacity of each potential link through waveform design and decide which node (RX_1 or RX_2) is selected as next hop.

3.2.1 Physical-Layer Model

Let (i, j) denote a wireless data link between transmitter i and receiver j. A data frame of N unit-energy information symbols drawn from a constellation $\mathcal{A}$ modulate a code-waveform $\psi_{ij}(t)$ of duration T. The transmitted signal for the link (i, j) is

$$x_{ij}(t) \triangleq \sqrt{E_i} \sum_{n=0}^{N-1} b_i[n]\psi_{ij}(t - nT)e^{j(2\pi f_c t + \phi_i)} \tag{3.1}$$

where $0 < E_i \leq E_{max}$ denotes the transmitted energy per symbol, $b_i[n] \in \mathcal{A}$ is the n-th information symbol and ϕ_i is the carrier phase related to carrier frequency f_c at the i-th

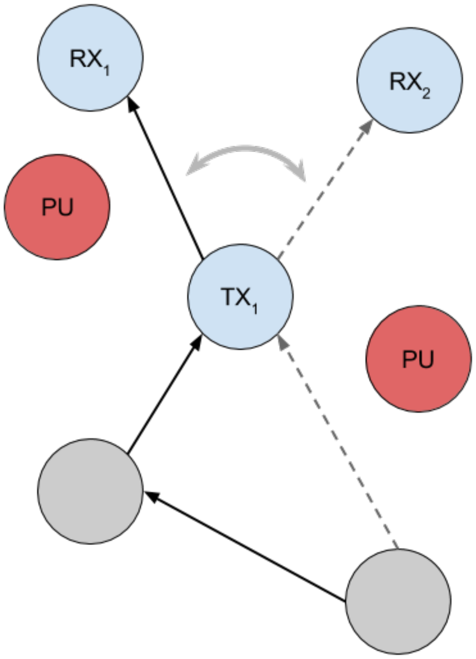

Figure 3.1: Generic ad-hoc secondary network coexisting with primary users (or equivalently, intentional interferers).

transmitter. The modulating waveform for link (i, j) is given by

$$\psi_{ij}(t) \triangleq \sum_{l=0}^{L-1} s_{ij}[l] g_{T_c}(t - lT_c) \tag{3.2}$$

where $s_{ij}[l] \in \left\{\pm 1/\sqrt{L}\right\}$ is the l-th bit of a length-L binary code vector $\mathbf{s}_{ij}$, and $g_{T_c}(\cdot)$ is a square-root-raised-cosine (SRRC) pulse with roll-off factor α and duration T_c, such that symbol duration $T = LT_c$ and bandwidth $B = (1 + \alpha)/T_c$.

Transmitted signals are considered to propagate over Rayleigh fading channels with M resolvable paths. Multipath fading is modeled by a linear tapped-delay line with taps that are spaced at intervals of T_c and are weighted by independent fading coefficients. Received signals include additive white Gaussian noise with variance σ_z^2 and interference from both primary and secondary links. Denote the set of active primary links as $\mathcal{PU}$ and the set of active secondary links as $\mathcal{SU}$.

Ignoring for the moment carrier and timing synchronization, the signal received at the j-th secondary receiver over the link of interest $(i,j) \in \mathcal{SU}$ after carrier downconversion, pulse-matched filtering, and sampling at the multipath-extended symbol duration of $(NL{+}M{-}1)T_c$ seconds is

$$\mathbf{y}^{(s)}_{(i,j)}[n] = \sqrt{E_i}\mathbf{H}_{ij}\mathbf{s}_{ij}b_i[n] + \sum_{(c,q)\in\mathcal{PU}} \sqrt{E_c}\mathbf{H}_{cj}\mathbf{s}_{cq}b_c[n] + \sum_{\substack{(a,g)\in\mathcal{SU}\\(a,g)\neq(i,j)}} \sqrt{E_a}\mathbf{H}_{aj}\mathbf{s}_{ag}b_a[n] + \mathbf{z}_j \quad (3.3)$$

where $\mathbf{z}_j$ is an additive white Gaussian noise vector and $\mathbf{H}_{ij}$ is the multipath fading channel matrix between transmitter i and receiver j given by

$$\mathbf{H}_{ij} \triangleq \sum_{m=0}^{M-1} h_{ij}[m] \begin{bmatrix} \mathbf{0}_{m\times L} \\ \mathbf{I}_{L\times L} \\ \mathbf{0}_{(M-m-1)\times L} \end{bmatrix} \in \mathbb{C}^{L_M\times L} \quad (3.4)$$

with $(L_M \triangleq L + M - 1)$. Block fading channels are considered, where $\{h_{ij}[m]\}_{m=0}^{M-1}$ are independent zero-mean complex Gaussian random variables that model the fading phenomena and are assumed to remain constant over a coherence time interval $T_d = N \cdot T$. Likewise, the signal received at the v-th primary receiver over the link of interest (u,v) is

$$\mathbf{y}^{(p)}_{(u,v)}[n] = \sqrt{E_u}\mathbf{H}_{uv}\mathbf{s}_{uv}b_u[n] + \sum_{\substack{(c,q)\in\mathcal{PU}\\(c,q)\neq(u,v)}} \sqrt{E_c}\mathbf{H}_{cv}\mathbf{s}_{cq}b_c[n] + \sum_{(a,g)\in\mathcal{SU}} \sqrt{E_a}\mathbf{H}_{av}\mathbf{s}_{ag}b_a[n] + \mathbf{z}_v. \quad (3.5)$$

In (3.5), the first term denotes the signal of interest, the second term represents the sum interference from all other primary links, and the third term the sum interference from all secondary links. Pre-detection SINRs at the output of the maximum-SINR RAKE filter [53] applied at the receiver for link (i,j) and (u,v) are, respectively,

$$\mathrm{SINR}_{ij} = E_i \mathbf{s}_{ij}^T \mathbf{H}_{ij}^H \mathbf{A}_{\backslash(i,j)}^{-1} \mathbf{H}_{ij}^H \mathbf{s}_{ij} \tag{3.6}$$

$$\mathrm{SINR}_{uv} = E_u \mathbf{s}_{uv}^T \mathbf{H}_{uv}^H \mathbf{A}_{\backslash(u,v)}^{-1} \mathbf{H}_{uv}^H \mathbf{s}_{uv} \tag{3.7}$$

where $\mathbf{A}_{\backslash(i,j)}$ and $\mathbf{A}_{\backslash(u,v)}$ are the noise-plus-interference matrices measured at the receiver for link (i,j) and (u,v), respectively,

$$\mathbf{A}_{\backslash(i,j)} \triangleq \sum_{(c,q)\in\mathcal{PU}} E_c \mathbf{H}_{cj} \mathbf{s}_{cq} \mathbf{s}_{cq}^T \mathbf{H}_{cj}^H + \sum_{\substack{(a,g)\in\mathcal{SU} \\ (a,g)\neq(i,j)}} E_a \mathbf{H}_{aj} \mathbf{s}_{ag} \mathbf{s}_{ag}^T \mathbf{H}_{aj}^H + \sigma_z^2 \mathbf{I} \tag{3.8}$$

$$\mathbf{A}_{\backslash(u,v)} \triangleq \sum_{\substack{(c,q)\in\mathcal{PU} \\ (c,q)\neq(u,v)}} E_c \mathbf{H}_{cv} \mathbf{s}_{cq} \mathbf{s}_{cq}^T \mathbf{H}_{cv}^H + \sum_{(a,g)\in\mathcal{SU}} E_a \mathbf{H}_{av} \mathbf{s}_{ag} \mathbf{s}_{ag}^T \mathbf{H}_{av}^H + \sigma_z^2 \mathbf{I}. \tag{3.9}$$

The capacity of link (i,j) is $C_{ij} = B\log_2(1+\mathrm{SINR}_{ij})$ for fixed bandwidth B and instantaneous SINR_{ij}.

3.2.2 Network-Layer Model

With code-division multiple access providing diversity, each network node employs a random access MAC protocol whereby a network node accesses spectrum immediately whenever there are packets in its queue. Each network node maintains a separate queue for each session d for which it is either a source or an intermediate node. The queue size at the i-th network node is updated as follows

$$Q_i^d(t+1) \triangleq \left[Q_i^d(t) + \sum_{k,k\neq i} R_{ki}^d(t) - \sum_{j,j\neq i} R_{ij}^d(t) + \mu_i^d(t) \right]^+ \tag{3.10}$$

where $Q_i^d(t)$ is the number of queued frames of session d waiting for transmission, $\mu_i^d(t)$ is the endogenous traffic arrival rate of session d, and $R_{ij}^d(t)$ is the transmission rate (in packets/s) on link (i,j) for session d at time t. The differential backlog between $Q_i^d(t)$ and $Q_j^d(t)$ is defined as $\Delta Q_{ij}(t) \triangleq \max_d[Q_i^d(t) - Q_j^d(t)]^+$.

3.2.3 Joint Optimization

At each time slot t, a centralized controller with global knowledge of the network can optimize throughput by selecting the set of active secondary links $\mathcal{SU}(t)$ and their respective code-waveforms $\mathbf{s}(t) = \{\mathbf{s}_{ij}(t) : (i,j) \in \mathcal{SU}(t)\}$, and symbol energies $E(t) = \{E_i(t) : i \in \mathcal{SU}(t)\}$ to maximize the weighted sum of differential backlogs. The optimization problem can be written as [24]

$$\underset{\mathbf{s}(t),E(t)}{\text{maximize}} \quad \sum_{i\in\mathcal{SU}} \sum_{\substack{j\in\mathcal{SU}\\ i\neq j}} C_{ij}(\mathbf{s}(t),E(t)) \cdot \Delta Q_{ij}(t) \tag{3.11}$$

$$\text{subject to} \quad \text{SINR}_{ij} \geq \text{SINR}_{th}^{\mathcal{SU}}, \quad \forall(i,j) \in \mathcal{SU} \tag{3.12}$$

$$\text{SINR}_{uv} \geq \text{SINR}_{th}^{\mathcal{PU}}, \quad \forall(u,v) \in \mathcal{PU} \tag{3.13}$$

$$\mathbf{s}_{ij}^T\mathbf{s}_{ij} = 1,\ E_i \leq E_{max}, \quad \forall(i,j) \in \mathcal{SU} \tag{3.14}$$

with constraints (3.12) and (3.13) ensuring predefined quality of service thresholds $\text{SINR}_{th}^{\mathcal{SU}}$ and $\text{SINR}_{th}^{\mathcal{PU}}$ are met for all secondary and primary users, respectively.

However, this centralized optimization is NP-hard in general. In [24] the authors propose a decentralized version of the algorithm solved independently at each network node. Particularly, the i-th backlogged node, at each decision period, implements the following algorithm:

1) Find the set of feasible next hops for each session d that are neighbors to node i.

2) Maximize link-capacity C_{ij} by optimizing code-waveforms $\mathbf{s}_{ij}$ for each of the feasible next hop links (i,j).

3) Schedule the session d^* with next hop j^* such that the utility $U_{ij} = C_{ij} \cdot \Delta Q_{ij}$ is maximized.

A detailed derivation in [24] produces an algorithm for optimizing code-waveforms (Step 2) that is solvable in polynomial time. However, the theoretical work assumes exact knowledge of the spread-spectrum transmissions of the primary users. In the following section, a modified version of the problem is discussed which uses spectrum sensing to coexist with wideband (spread-spectrum) and narrowband primaries with unknown channels [54].

3.3 Extension to Wideband & Narrowband Primaries

Work in [54] considers a much simpler network with multiple primary transmitters, one primary receiver, and only one secondary link. With no routes to choose, the all-spectrum cognitive channelization algorithm adapts bit energy and code-waveform to maximize pre-detection SINR subject to a primary interference threshold.

3.3.1 Revised Signal Model

The simplified signal model considering this scenario is

$$\mathbf{y}_{(i,j)}^{(s)}[n] = \sqrt{E_i}\mathbf{H}_{ij}\mathbf{s}_{ij}b_i[n] + \mathbf{p}_j[n] + \mathbf{z}_j[n] \tag{3.15}$$

where $\mathbf{s}_{ij}$ is the code-waveform of the secondary link (i,j) and $\mathbf{p}_j$ is sum of interference from all active primary links as received at the secondary receiver j. After applying the maximum-SINR filter, pre-detection SINR of link (i,j) at the secondary receiver is

$$\mathrm{SINR}_{ij} = E_i\mathbf{s}_{ij}^T\mathbf{H}_{ij}^H\mathbf{R}_{I+N}^{(s)-1}\mathbf{H}_{ij}\mathbf{s}_{ij} = E_i\mathbf{s}_{ij}^T\mathbf{P}_s\mathbf{s}_{ij} \tag{3.16}$$

where $\mathbf{P}_s \triangleq \mathbf{H}_{ij}^H \mathbf{R}_{I+N}^{(s)-1} \mathbf{H}_{ij}$, $\mathbf{P}_s \succ 0$ is the channel-processed version of the inverse noise-plus-interference autocorrelation matrix

$$\mathbf{R}_{I+N}^{(s)} \triangleq E\left\{\left|(\mathbf{p}_j + \mathbf{z}_j)\right|^2\right\}. \tag{3.17}$$

which can contain either wideband or narrowband primary user transmissions. In practice, $\mathbf{R}_{I+N}^{(s)}$ is estimated by a sample-average estimate

$$\widehat{\mathbf{R}}_{I+N}^{(s)} = \frac{1}{N_{avg}} \sum_{n=1}^{N_{avg}} (\mathbf{p}_j[n] + \mathbf{z}_j[n])(\mathbf{p}_j[n] + \mathbf{z}_j[n])^H \tag{3.18}$$

calculated over N_{avg} averages.

3.3.2 Primary Interference Constraint

When the secondary transmitter is operational, it increases the interference level at the primary receiver v by the quantity $E_i \mathbf{s}_{ij}^T \mathbf{H}_{iv}^H \mathbf{H}_{iv} \mathbf{s}_{ij}$. The constraint in (3.13) requires that the SINR at the primary receiver is kept above a threshold $\mathrm{SINR}_{th}^{\mathcal{PU}}$ or, equivalently, that the noise and interference level at the primary receiver is kept below a tolerable interference temperature limit $T_L(f_c)$ in Kelvin (K). Meeting this constraint in practical systems is challenging since the secondary transmitter does not explicitly know (i) the level of interference from other sources operating in the vicinity nor (ii) the channel $\mathbf{H}_{iv}$ between the secondary transmitter and the primary receiver.

Interference temperature $T_I(f_c, B)$ is specified for a given carrier frequency f_c and bandwidth B, and can characterize both interference and noise in a particular location [55]. More specifically,

$$T_I(f_c, B) \triangleq \frac{P_I(f_c, B)}{kB} \tag{3.19}$$

where $P_I(f_c, B)$ is the average interference power in Watts, centered at f_c and covering bandwidth of B Hertz and $k = 1.38 \cdot 10^{-23}$ Joules/K is the Boltzmann constant. Since the primary users do not communicate with the secondary user, $T_I(f_c, B)$ is estimated using the parameter values for f_c and B evaluated at the secondary user during its silent periods,

$$\widehat{T}_I(f_c, B) = \frac{1}{kB^2} \int_{f_c - B/2}^{f_c + B/2} S_p(f)\mathrm{d}f \tag{3.20}$$

where $S_p(f)$ is the measured power spectral density (PSD) of the primary transmitted signals.

3.3.3 Revised Optimization Problem

With the interference temperature formulation, the optimization problem is rewritten [54]

$$\underset{E_i, \mathbf{s}_{ij}}{\text{maximize}} \quad E_i \mathbf{s}_{ij}^T \mathbf{P}_s \mathbf{s}_{ij} \tag{3.21}$$

$$\text{subject to} \quad \widehat{T}_I(f_c, B) + \frac{2\mu E_i}{(1+\alpha)k} \leq T_L(f_c) \tag{3.22}$$

$$E_i \mathbf{s}_{ij}^T \mathbf{P}_s \mathbf{s}_{ij} \geq \text{SINR}_{th}^{\mathcal{SU}} \tag{3.23}$$

$$\mathbf{s}_{ij}^T \mathbf{s}_{ij} = 1, \quad 0 < E_s \leq E_{max} \tag{3.24}$$

where the second term in (3.22) is the interference temperature of the secondary transmitter at the primary receiver with α the roll-off factor of the square-root raised cosine pulse shaping and $\mu \in [0, 1]$ modeling attenuation due to fading and path loss between the secondary transmitter and primary receiver. The authors in [54] suggest the parameter μ can be selected based on distance between the secondary transmitter and primary receivers.

The optimization problem in (3.21) becomes separable only if the secondary QoS constraint (3.23) is dropped. Since the problem is only feasible if the solution satisfies the secondary QoS constraint, the optimal solution, if it exists, is not affected by dropping the constraint in (3.23). Therefore, the optimal transmitting energy can be calculated as

$$E_{opt} = \frac{(1+\alpha)k}{2\mu}(T_L(f_c) - T_I(f_c, B)). \tag{3.25}$$

Applying (3.25) to (3.21) produces a new optimization problem

$$\underset{\mathbf{s}_{ij}}{\text{maximize}} \;\; \mathbf{s}_{ij}^T \mathbf{P}_s \mathbf{s}_{ij} \tag{3.26}$$

$$\text{subject to } \mathbf{s}_{ij}^T \mathbf{s}_{ij} = 1. \tag{3.27}$$

In practice, the optimization problem in (3.26) is solved and then the inequality in (3.23) is evaluated. If the constraint is not satisfied, the problem is infeasible and adaptation is paused for a given time period. This procedure can be repeated in an adaptive fashion by revising the problem in (3.21) every time the power profile of the primary users change.

3.4 Expansion to Contested Environments

It is straightforward to prove that the signal model in (3.15) will also apply to harmful interference in a contested radio environment scenario. In this formulation, $\mathbf{p}_j$ now models deliberate interference received at the friendly receiver. The structure of the interference source is reflected in the interference-plus-noise autocorrelation matrix $\mathbf{R}_{I+N}^{(s)}$. With no primary user network to protect, the friendly link no longer tries to optimize its energy to limit interference and sets $E_i = E_{max}$. The optimization problem then becomes

$$\underset{\mathbf{s}_{ij}}{\text{maximize}} \quad \mathbf{s}_{ij}^T \mathbf{P}_s \mathbf{s}_{ij} \tag{3.28}$$

$$\text{subject to} \quad \mathbf{s}_{ij}^T \mathbf{s}_{ij} = 1. \tag{3.29}$$

which is identical to (3.26) and can be solved in the same way. This formulation is the basis for the physical-layer interference avoidance capability developed and experimentally evaluated in Chapter 4.

3.5 Code-Waveform Optimization

Up to this point, discussion in this chapter has presented optimization problems which, when solved, will produce an optimal waveform $\mathbf{s}_{opt}$ for a set of goals and constraints. This section will evaluate the procedures for generating $\mathbf{s}_{opt}$.

Consider the optimization problem in (3.26). At the j-th receiver of a secondary link (i, j), a binary waveform $\mathbf{s}$ is designed to maximize $\mathrm{SINR_{ij}}(\mathbf{s})$ at the output of the maximum-SINR filter

$$\mathbf{s}_{opt} \triangleq \underset{\mathbf{s}_{ij} \in \left\{\pm \frac{1}{\sqrt{L}}\right\}^{L}}{\operatorname{argmax}} \ \mathrm{SINR}_{ij}(\mathbf{s}_{ij}) = \underset{\mathbf{s}_{ij} \in \left\{\pm \frac{1}{\sqrt{L}}\right\}^{L}}{\operatorname{argmax}} \ \mathbf{s}_{ij}^{T}\mathbf{P}_{s}\mathbf{s}_{ij}. \tag{3.30}$$

The problem of obtaining the optimal waveform for link (i, j) is NP-hard [56, 57] and can be solved through exhaustive search over all possible L-waveform-bit combinations. In the next two subsections, two computationally efficient methods for optimizing waveform $\mathbf{s}$ for link (i, j) are presented.

3.5.1 Rank-1 Waveform Design

Given the eigendecomposition of $\mathbf{P}_s$, where $\mathbf{q}_1, \mathbf{q}_2, \ldots, \mathbf{q}_L$ are the eigenvectors, and $\lambda_1 \geq \lambda_2 \geq \cdots \geq \lambda_L > 0$ are the corresponding eigenvalues of $\mathbf{P}_s$, the optimization problem in

Single-bit Flipping (SBF) Waveform Design Algorithm

```
$p := 0$; input $\mathbf{P}_s$ and $\mathbf{s}_{ij}^{(0)} \in \left\{\pm 1/\sqrt{L}\right\}^L$
$p := p + 1$;
    $\alpha^{(p)}[k] \leftarrow s_{ij}^{(p)}[k] \left(\sum_{l \neq k} s_{ij}^{(p)}[l] \Re\left\{[\mathbf{P}_s]_{k,l}\right\}\right)$
    $(v, q) \leftarrow \min(\boldsymbol{\alpha}^{(p)})$
    if $v < 0$ then
        $s_{ij}^{(p)}[q] \leftarrow -s_{ij}^{(p)}[q]$
    else
        return $\widehat{\mathbf{s}}_{opt} = \mathbf{s}_{ij}^{(p)}$
```

Figure 3.2: Single-bit flipping (SBF) waveform design algorithm. ©2018 IEEE.

(3.30) is rewritten as

$$\mathbf{s}_{opt} \triangleq \underset{\mathbf{s}_{ij} \in \left\{\pm \frac{1}{\sqrt{L}}\right\}^L}{\operatorname{argmax}} \left\{\sum_{i=1}^{L} \lambda_i \left\|\mathbf{s}_{ij}{}^T \mathbf{q}_i\right\|^2\right\} \tag{3.31}$$

where $0 \leq \left\|\mathbf{s}_{ij}{}^T \mathbf{q}_i\right\|^2 \leq 1$, for $i = 1, 2, \cdots, L$. Simplifying the problem by keeping only the strongest term, $\lambda_1 \left\|\mathbf{s}_{ij}^T \mathbf{q}_1\right\|^2$, the rank-1 optimized waveform is obtained

$$\widehat{\mathbf{s}}_{opt} \triangleq \underset{\mathbf{s}_{ij} \in \left\{\pm \frac{1}{\sqrt{L}}\right\}^L}{\operatorname{argmax}} \left\{\left\|\mathbf{s}_{ij}^T \mathbf{q}_1\right\|^2\right\} = \pm \frac{1}{\sqrt{L}} \operatorname{sgn}\left(\Re\left\{\mathbf{q}_1\right\}\right) \tag{3.32}$$

where sgn$(\cdot)$ denotes the sign operator. Hence, a rank-1 optimal waveform is acquired by first relaxing the binary constraint in the waveform optimization problem in (3.30) and solving optimally the relaxed problem. Finally, the minimum-eigenvalue eigenvector of $\mathbf{P}_s$ is simply mapped (quantized) to the binary field, by taking the sign of its components [54, 58].

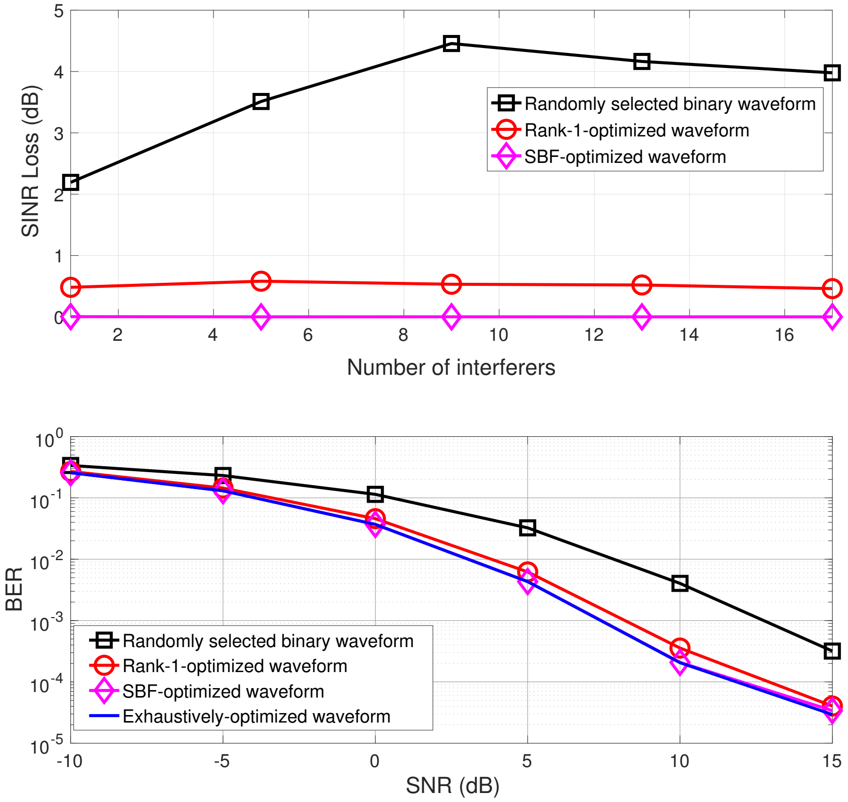

Figure 3.3: Post-filtering SINR loss of a randomly selected, a rank-1, and a SBF-optimized waveform versus the number of interferers (top). BER versus SNR of the user of interest for different waveform optimization techniques (bottom). ©2018 IEEE.

3.5.2 Single-Bit Flipping (SBF) Waveform Design

A second lightweight algorithm for finding a near-optimal solution to the binary code-waveform that maximizes SINR at the output of the maximum-SINR filter is based on iterative single-bit flipping (SBF). Similar algorithms have been studied in L_1-subspace decomposition [59, 60] and channel coding [61] literature. The steps of the SBF algorithm are described in detail in Fig. 3.2.

More specifically, SINR at the output of the maximum-SINR filter can be written as

$$\begin{aligned}
\mathbf{s}_{ij}^{(p)^T}\mathbf{P}_s\mathbf{s}_{ij}^{(p)} &= \mathbf{s}_{ij}^{(p)^T}\left(\Re\left\{\mathbf{P}_s\right\} + \mathrm{j}\Im\left\{\mathbf{P}_s\right\}\right)\mathbf{s}_{ij}^{(p)} \\
&= \mathbf{s}_{ij}^{(p)^T}\Re\left\{\mathbf{P}_s\right\}\mathbf{s}_{ij}^{(p)} = \frac{1}{L}\,\mathrm{Tr}\left(\Re\left\{\mathbf{P}_s\right\}\right) + \\
&+ \sum_k 2s_{ij}^{(p)}[k]\left(\sum_{l>k} s_{ij}^{(p)}[l]\Re\left\{[\mathbf{P}_s]_{k,l}\right\}\right)
\end{aligned} \tag{3.33}$$

where $\Re\{\cdot\}$ and $\Im\{\cdot\}$ denote the real and complex part of a vector or matrix, respectively. Appendix A presents a more detailed derivation of this equation. By changing the sign of the k-th waveform bit $s_{ij}^{(p)}[k]$ in the p-th iteration of the SBF algorithm, the post-filtering SINR value will change by

$$\alpha^{(p)}[k] \triangleq \pm 4s_{ij}^{(p)}[k]\left(\sum_{l\neq k} s_{ij}^{(p)}[l]\Re\left\{[\mathbf{P}_s]_{k,l}\right\}\right). \tag{3.34}$$

Consequently, if the result in (3.34) is negative, then flipping the k-th code-waveform-bit from $s_{ij}^{(p)}[k]$ to $-s_{ij}^{(p)}[k]$ will increase the post-filtering SINR value in (3.33). Obviously, flipping the waveform-bit with the highest negative contribution will offer the biggest SINR increase. On the other hand, if there is no bit flip that will increase the SINR value in (3.33), then the SBF algorithm terminates.

Fig. 3.3 compares the post-filtering SINR loss of a randomly generated binary code-waveform to a rank-1 optimal and an SBF-optimized binary waveform as a function of the number of interferers. Particularly, SINR loss is evaluated with respect to the SINR of the optimal binary waveform $\mathbf{s}_{opt}$ that is obtained through exhaustive search over all possible L waveform-bit combinations. Additionally, bit error rate (BER) versus SNR for the user of interest is depicted for the different waveform optimization techniques and fixed number of interferers equal to the code-waveform length $L = 8$. In both simulations, the SNR for the user of interest is fixed to 8 dB, while the SNRs of the interferers are uniformly spaced between 8 and 11 dB. It can be observed that the performance of the SBF-optimized waveform closely approaches that of the exhaustively-optimized for the parameters considered in this simulation.

3.6 MIMO Code-Waveform Optimization

Lastly, this section will extend the signature design problem in 3.5 to consider multiple antennas at each secondary user. A major advantage of multiple-input and multiple-output (MIMO) links is the increased capacity over single-input and single-output (SISO) links. When MIMO links exist in the presence of rich multipath scattering the channels between antenna elements can be considered independent and channel capacity is proportional to the minimum number of transmit and receive antennas [62]. However, this assumption may not hold in physical systems where capacity grows at a less-than-linear rate with the number of antennas [63]. Both time-varying spatial correlation and structural spatial correlation between channels causes rank loss in the channel correlation matrix [64]. The cause of spatial correlation can be attributed to a number of factors including insufficient antenna spacing or lack of rich multipath scattering in the propagation environment [65]. When the instantaneous channels of transmit antennas become quasi-identical due to high correlation, the MIMO system becomes an equivalent single-input-multiple-output (SIMO) system [66].

Space-time block coding (STBC) can be used as a method to recover bits even in highly correlated channels [67]. The design of such codes has been extensively studied in the literature [68]. However, few methods exist that combine adaptive multiuser diversity and interference avoidance with coding. To address related work, the combination of an Alamouti STBC and a transmit precoding matrix to cancel out interference from other users is discussed in [69]. The problem of jointly designing signature sets and beamformer weights in the context of a cellular base station is considered in [70]. In [71] a different technique to combine MIMO and CDMA is proposed. A set of Walsh-Hadamard codes are used to multiplex a number of symbols at each antenna. After multiplexing, the resulting signal is multiplied with a pseudo-random sequence such that the signatures can be modeled as random and reused for each antenna. This section will describe how the waveform design problem in Section 3.5 can be expanded to consider the design of a set of code-waveforms, one per antenna.

3.6.1 System Model

Consider the (i, j) link between transmitter i and receiver j and drop the subscripts (e.g. $\mathbf{s}_{ij} \to \mathbf{s}$) for simplicity. Without loss of generality, the link operates with two transmit and two receive antennas (2 × 2 MIMO) and channel matrix

$$\mathbf{H} = \begin{bmatrix} h_{11} & h_{12} \\ h_{21} & h_{22} \end{bmatrix} \tag{3.35}$$

where h_{mn} denotes the channel impulse response between the n-th transmit antenna and the m-th receive antenna, assumed to model frequency nonselective Rayleigh fading. Two independent streams of information symbols $b_a \in \{\pm 1\}$, $a = 1, 2$ modulating binary code-waveforms $\mathbf{s}_a \in \left\{\pm 1/\sqrt{L}\right\}^L$, $a = 1, 2$ are transmitted one stream per antenna. The received signal vectors at each antenna are

$$\begin{aligned} \mathbf{y}_1 &= h_{11}\mathbf{s}_1 b_1 + h_{12}\mathbf{s}_2 b_2 + \mathbf{p}_1 + \mathbf{z}_1 \\ \mathbf{y}_2 &= h_{21}\mathbf{s}_1 b_1 + h_{22}\mathbf{s}_2 b_2 + \mathbf{p}_2 + \mathbf{z}_2 \end{aligned} \tag{3.36}$$

where $\mathbf{p}_a$ and $\mathbf{z}_a$ denote external interference and white Gaussian noise measured at the a-th receive antenna, respectively.

3.6.2 2x2 MIMO Signature Design

3.6.2.1 System Matrix Representation

Starting with the system model in (3.36) the received signal vectors can be written as

$$\begin{bmatrix} \mathbf{y}_1 \\ \mathbf{y}_2 \end{bmatrix} = \begin{bmatrix} h_{11}\mathbf{I}_L & h_{12}\mathbf{I}_L \\ h_{21}\mathbf{I}_L & h_{22}\mathbf{I}_L \end{bmatrix} \begin{bmatrix} \mathbf{s}_1 & \mathbf{0}_L \\ \mathbf{0}_L & \mathbf{s}_2 \end{bmatrix} \begin{bmatrix} b_1 \\ b_2 \end{bmatrix} + \begin{bmatrix} \mathbf{p}_1 \\ \mathbf{p}_2 \end{bmatrix} + \begin{bmatrix} \mathbf{z}_1 \\ \mathbf{z}_2 \end{bmatrix} \tag{3.37}$$

where $\mathbf{I}_L$ is an $(L \times L)$ identity matrix and $\mathbf{0}_L$ is an $(L \times 1)$ zero vector. Let $\bar{\mathbf{H}}$ denote the block version of $\mathbf{H}$ with channel coefficients multiplied by $\mathbf{I}_L$. The expression in (3.37) can be written as $\mathbf{y} = \bar{\mathbf{H}}\mathbf{S}\mathbf{b} + \mathbf{p} + \mathbf{z}$. The noise-plus-interference vectors have an autocorrelation matrix $\mathbf{R}_N = E\{(\mathbf{p}+\mathbf{n})(\mathbf{p}+\mathbf{n})^H\}$ where $E\{\cdot\}$ denotes statistical expectation and $\mathbf{R}_N \neq \alpha\mathbf{I}_L$, that is, $\mathbf{R}_N$ is not assumed to be "white". For notational simplicity, denote the and second columns of $\bar{\mathbf{H}}$ as

$$\mathbf{H}_1 = \left[\bar{\mathbf{H}}\right]_{:,1:L} = \begin{bmatrix} h_{11}\mathbf{I}_L \\ h_{21}\mathbf{I}_L \end{bmatrix} \quad \mathbf{H}_2 = \left[\bar{\mathbf{H}}\right]_{:,L+1:2L} = \begin{bmatrix} h_{12}\mathbf{I}_L \\ h_{22}\mathbf{I}_L \end{bmatrix} \tag{3.38}$$

which allows (3.37) to be written as

$$\mathbf{y} = \mathbf{H}_1\mathbf{s}_1 b_1 + \mathbf{H}_2\mathbf{s}_2 b_2 + \mathbf{p} + \mathbf{n}. \tag{3.39}$$

A pair of SINR-maximizing filter vectors are applied and information symbols recovered by minimum-distance detection

$$\hat{b}_1 = \underset{b \in \mathcal{A}}{\arg\min} \left|\mathbf{w}_1^H \mathbf{y} - b\right|^2 \tag{3.40}$$

$$\hat{b}_2 = \arg\min_{b \in \mathcal{A}} \left| \mathbf{w}_2^H \mathbf{y} - b \right|^2 \tag{3.41}$$

3.6.2.2 Output SINR Maximization

The pre-detection SINR at the output of each maximum-SINR filter will be

$$\mathrm{SINR}_1 = \mathbf{s}_1^T \mathbf{H}_1^H \mathbf{R}_{/1}^{-1} \mathbf{H}_1 \mathbf{s}_1 \tag{3.42}$$

where $\mathbf{R}_{/1} = \mathbf{R}_N + \mathbf{H}_2 \mathbf{s}_2 \mathbf{s}_2^T \mathbf{H}_2^H$ denotes the "exclude-1" autocorrelation matrix. The objective of the design problem is to choose a set of signatures $(\mathbf{s}_1, \mathbf{s}_2)$ which maximizes the sum of each symbol's SINR

$$\mathrm{sumSINR} = \mathrm{SINR}_1 + \mathrm{SINR}_2 \tag{3.43}$$

which is made challenging by the fact that $\mathbf{R}_{/1}$ contains $\mathbf{s}_2$ and therefore SINR_1 is a function of both $\mathbf{s}_1$ and $\mathbf{s}_2$. The expression can be expanded by inverting $\mathbf{R}_{/1}^{-1}$

$$\mathbf{R}_{/1}^{-1} = \mathbf{R}_N^{-1} - \frac{\mathbf{R}_N^{-1} \mathbf{H}_2 \mathbf{s}_2 \mathbf{s}_2^T \mathbf{H}_2^H \mathbf{R}_N^{-1}}{1 + \mathbf{s}_2^T \mathbf{H}_2^H \mathbf{R}_N^{-1} \mathbf{H}_2^H \mathbf{s}_2} \tag{3.44}$$

and using this result to rewrite (3.42) as

$$\mathrm{SINR}_1 = \mathbf{s}_1^T \mathbf{H}_1^H \mathbf{R}_N^{-1} \mathbf{H}_1 \mathbf{s}_1 - \frac{\left| \mathbf{s}_1^T \mathbf{H}_1^H \mathbf{R}_N^{-1} \mathbf{H}_2 \mathbf{s}_2 \right|^2}{1 + \mathbf{s}_2^T \mathbf{H}_2^H \mathbf{R}_N^{-1} \mathbf{H}_2^H \mathbf{s}_2} \tag{3.45}$$

and likewise for SINR_2

$$\mathrm{SINR}_2 = \mathbf{s}_2^T \mathbf{H}_2^H \mathbf{R}_N^{-1} \mathbf{H}_2 \mathbf{s}_2 - \frac{\left| \mathbf{s}_2^T \mathbf{H}_2^H \mathbf{R}_N^{-1} \mathbf{H}_1 \mathbf{s}_1 \right|^2}{1 + \mathbf{s}_1^T \mathbf{H}_1^H \mathbf{R}_N^{-1} \mathbf{H}_1^H \mathbf{s}_1}. \tag{3.46}$$

Then the following notational simplification can be made. Denote the first term in (3.45) and (3.46) as $\mathrm{SINR}_1'(\mathbf{s}_1) \triangleq \mathbf{s}_1^T \mathbf{H}_1^H \mathbf{R}_N^{-1} \mathbf{H}_1 \mathbf{s}_1$ and $\mathrm{SINR}_2'(\mathbf{s}_2) \triangleq \mathbf{s}_2^T \mathbf{H}_2^H \mathbf{R}_N^{-1} \mathbf{H}_2 \mathbf{s}_2$, respectively.

Noting that the numerators of both second terms are equivalent, the term $\eta(\mathbf{s}_1, \mathbf{s}_2) \triangleq \left|\mathbf{s}_2^T \mathbf{H}_2^H \mathbf{R}_N^{-1} \mathbf{H}_1 \mathbf{s}_1\right|^2 = \left|\mathbf{s}_1^T \mathbf{H}_1^H \mathbf{R}_N^{-1} \mathbf{H}_2 \mathbf{s}_2\right|^2$ is defined. Finally, (3.43) can be written as

$$\text{sumSINR} = \text{SINR}_1'(\mathbf{s}_1) + \text{SINR}_2'(\mathbf{s}_2) - \left(\frac{\eta(\mathbf{s}_1, \mathbf{s}_2)}{1 + \text{SINR}_2'(\mathbf{s}_2)} + \frac{\eta(\mathbf{s}_1, \mathbf{s}_2)}{1 + \text{SINR}_1'(\mathbf{s}_1)}\right) \tag{3.47}$$

It can be seen that individually maximizing $\text{SINR}_1'(\mathbf{s}_1)$ and $\text{SINR}_2'(\mathbf{s}_2)$ will also reduce the last term in (3.47).

Chapter 4

Airborne Cognitive Networking: From Design to Deployment

4.1 Introduction

Future airborne networks will be defined by the resilience to maintain wireless connectivity in dynamic communication environments and the intelligence to adapt to varying traffic loads, RF interference, and frequent network failures. The design of airborne networks is challenged by rapidly changing network dynamics, limited energy and link-bandwidth capacity between high/low-speed mobile wireless nodes that are either geographically or hierarchically dispersed [1, 8, 9]. Existing design approaches rely on either channel/network emulations [72–74] or implementation of layered wireless network architectures on off-the-shelf radio devices [75, 76]. As a result, integration of autonomous radio reconfiguration functionalities to unmanned aerial vehicle (UAV) platforms [6] and their evaluation in real-time remains quite challenging.

Wireless links in UAV networks are subject to time-varying quality due to high mobility, distance-dependent path loss, interference, multi-path, and Doppler effects among others.

Portions of this chapter are adapted from the author's published work in [2] (©2018 IEEE), a version of which also appeared in [26].

Peer-to-peer communication is fundamental to UAV networks. Contrary to terrestrial networks, UAV wireless networks rely on distributed network control architectures that have both cognitive coexistence and intra-network interference-avoidance requirements [8]. High node mobility exposes UAV wireless links to unpredictable interference levels that are time-varying and location-dependent, therefore dynamic management of link parameters is needed for being robust to network disruptions at any time and location. Continuously changing channel and interference conditions entail new network layer designs [6], where routes in multi-hop airborne networks are jointly optimized with communication link parameters at each hop. The requirements listed above are particularly important for UAV swarms because network disruptions may prevent the delivery of sensed data to the appropriate processing nodes, lead to insufficient situational awareness for effective in-field planning, and result in delayed/lost command and control messages, thereby creating significant deviation from the desired system behavior. At best, this will increase the time and number of assets required to complete a mission; at worst, it may result in mission failure. The ability to recover from the loss of any node is necessary to resilient operation of airborne networks [9].

Airborne communication systems can significantly benefit from the integration of cognitive radio (CR)-based resource allocation schemes, which can further enhance spectrum utilization efficiency and guarantee network connectivity when airborne communication links are constrained or unavailable. A comprehensive survey regarding spectrum utilization trends and CR in aeronautical communication systems can be found in [4]. Spectrum occupancy measurements show that certain parts of the radio spectrum, particularly frequency bands allocated for air-to-ground communications, remain underutilized [77]. This is partly due to the adoption of network architectures that rely on static resource allocation. Additionally, inherent couplings between the physical (PHY), medium access control (MAC), and network (NET) layers of the network protocol stack entail control and management of shared networking resources that vary in frequency, time, and space. Multi-UAV mesh networks with information sharing and multi-hop routing introduce additional demands of overhead and require highly efficient protocols to achieve good network performance [6]. Consequently, self-optimized, reconfigurable network architectures that implement distributed, optimal, cross-layer control decisions are expected to satisfy the dynamic demands and complex cross-layer interactions of future airborne mesh networks [78].

The following sections present the first systematic analysis across the PHY, MAC, and NET layers of the network protocol stack toward the implementation and real-time validation of all-spectrum cognitive networking [24] in a software-defined radio testbed. This chapter describes the development of an "elastic" testbed comprised of cross-layer cognitively optimized links that are co-located with static/baseline non-cognitively optimized links. The "elastic" testbed consists of terrestrial and airborne integrated software/hardware platforms. Cognitive links implement a novel distributed approach for spectral efficiency maximization by jointly designing channel-access waveforms that span the entire available spectrum (i.e. all-spectrum channelization) and selecting network routes under both intra- and inter-network interference scenarios.

First, system design challenges regarding software, hardware, and baseband processing requirements at PHY, MAC, and NET layers to fulfill the needs of the proposed distributed algorithm for cross-layer interactions and cognitive decision-making are identified. Additionally, signal processing details for the implementation of the cognitive framework including frame design and time/frequency synchronization are discussed. The modular architecture of the proposed platform allows us to abstractly define networking protocols with (or without) cross-layer interactions in a high-level description language and separate verification of upper-layer networking functionalities and physical-layer designs. Proof-of-concept experimental results from both indoor and outdoor testbed deployments show that the proposed cognitive platform can withstand intentional interference at PHY and NET layers as well as enable cognitive coexistence with non cross-layer optimized networks.

The development of the “elastic” testbed enables accelerated design and validation of cross-layer protocol solutions in realistic scenarios. The main contributions of this chapter can be summarized as follows:

- **Cross-Layer System-Level Analysis.** Identification of system design challenges and requirements at PHY, MAC, and NET layers for the implementation of all-spectrum cognitive networking.

- **Distributed Network Optimization.** A computationally efficient code-waveform optimization technique and distributed network control mechanism to handle real-time waveform and routing decisions at each cognitive network node.

- **Software-Radio Reconfigurable Framework.** Development of a complete integrated software/hardware radio reconfigurable framework to enable the first field deployment of all-spectrum cognitive networking on a hybrid ground-air software-defined radio testbed.

- **Testbed Evaluation.** Experimental validation of all-spectrum cognitive networking in realistic testbed scenarios (both indoor and outdoor) and demonstration that cognitively optimized network nodes can withstand both PHY- and NET-layer interference and enable underlay spectrum coexistence with non cross-layer optimized network nodes.

4.2 Related Work

Cognitive radio has emerged as a promising technology to improve spectrum utilization efficiency in wireless networks [22, 25, 79, 80] while cognitively networked UAVs have attracted interest for public safety and next-generation first-responder applications [81, 82].

Implementation of cognitive decision making algorithms for optimal network control yet remains quite challenging [83]. This section reviews state-of-the-art work in i) airborne cognitive networking, ii) cognitive radio algorithms for (joint) optimization of resource allocation parameters at either one or multiple layers of the network protocol stack, and iii) software-defined/cognitive radio testbeds.

Airborne Cognitive Networks. The need for cognitive spectrum sensing and sharing in aeronautical communication networks is highlighted in [84]. Cognitive radio is proposed in [85] as a solution to meet future UAV communication demands, particularly latency-sensitive control and high-throughput sensor data. Work in [86] proposes to use the position of a UAV as an additional degree of freedom to protect primary user transmissions in an underlay dynamic spectrum access scheme [25]. A survey on cognitive radio for UAVs in energy-based spectrum sensing techniques is studied in [87] for broadband VHF (B-VHF) aeronautical communication systems. Cognitive algorithms for LTE-A aerial base stations for public safety applications are discussed in [88].

Cognitive Resource Allocation Algorithms.

All-spectrum cognitive networking in [24] proposes for the first time in the literature, joint distributed power, code-waveform, and route allocation in a cognitive multi-hop network. Work in the field of all-spectrum channelization considers the design of code-waveforms for secondary (ad-hoc) wideband links that cooperate [36], or simply coexist without any form of cooperation with primary (spectrum licensees) wideband [89] and narrowband [54] stations in an underlay fashion. Since the spectrum environment in a multi-hop network varies in time and space, and interference to primary stations depends on the location of the cognitive nodes, it is important to jointly and dynamically optimize PHY-layer and routing functionalities at each network node. Transmit power and spectrum sensing parameters are optimized in [90] to minimize energy consumption in a cooperative-sensing-based code-division multiple access (CDMA) cognitive network.

Outside the framework of code-waveform based cognitive channelization altogether, interesting work in the form of joint beamforming and power allocation is reported in [91], while multi-antenna cognitive beamforming and interference avoidance algorithms are described in [92,93]. Hybrid overlay/underlay CR transmission systems in [94] and [95] efficiently exploit both unused and underutilized spectrum through orthogonal-frequency-division-multiplexing (OFDM) and multicarrier-CDMA.

An extensive overview of routing techniques for multi-hop cognitive radio networks can be found in [96]. A distributed algorithm for joint routing and dynamic spectrum allocation in unused spectrum bands (i.e. "white spaces") is proposed in [49]. Distributed routing to reduce interference to primary stations and minimize route delay is proposed in [97], while [98] describes a route selection algorithm based on location information and locally available spectrum access opportunities at each node. Two classes of routing protocols in [99] aim to reduce end-to-end latency and increase energy efficiency and throughput based on cooperative routing and spectrum aggregation techniques. On-demand based routing in [100] is conducted based on clustering of nodes according to spectrum availability, power, and node stability. Finally, work in [101] describes a joint rate adaptation, channel assignment, and routing approach to maximize network resource utilization.

Software-defined/Cognitive Radio Testbeds. Indoor testbed deployments in [102–104] describe hardware and software requirements toward rapid evaluation of CR protocols in real-world conditions with software-defined radio (SDR) and Android OS devices. All-spectrum cognitive channelization around wideband and narrowband primary stations is evaluated for the first time in an indoor SDR testbed in [54]. Work in [105] describes an experimental prototype for multi-antenna cognitive beamforming, while over-the-air experiments in [106,107] evaluate a hybrid overlay/underlay CR technique. Experimental work for spectral coexistence in "white spaces" is presented in [108,109]. A software-defined CR prototype based on off-the-shelf IEEE 802.11a/b/g wireless cards is developed in [110]. A distributed algorithm for joint routing and dynamic spectrum access in "white spaces" is implemented in SDRs in [111], while [112] evaluates the algorithm in SDRs that communicate with each other through a wireless network emulation platform. Simulations and experiments on an SDR testbed in [113] evaluate the performance of different routing protocols for CR networks. Route selection schemes based on reinforcement learning and spectrum leasing are experimentally evaluated in an SDR testbed in [114].

Prior work in the field of cognitive radio emphasizes the value of software-defined radio testbeds towards rapid evaluation of new algorithms in real-world communication environments. The following sections describe a reconfigurable software/hardware framework that enables self-optimization of protocol parameters across multiple layers in response to dynamic conditions. Particularly, this chapter discusses the requirements, design considerations, and algorithmic developments towards the first field deployment of all-spectrum cognitive networking in a hybrid ground-air software-defined radio testbed. Finally, proof-of-concept results are presented that demonstrate cognitive coexistence and interference avoidance, capabilities critical to satisfy the increasing throughput demands of unmanned airborne networks while maintaining connectivity in dynamic environments.

4.3 System Overview

4.3.1 System Model

This section considers an "elastic" network comprised of cognitively cross-layer optimized wireless links that are co-located with static/baseline, non-cognitively optimized wireless links that implement a layered network protocol stack (Fig. 4.1). Traffic flows for both networks are carried over multi-hop routes and traffic demands consist of unicast sessions that are characterized by a source node s and a destination node d. Static/baseline network

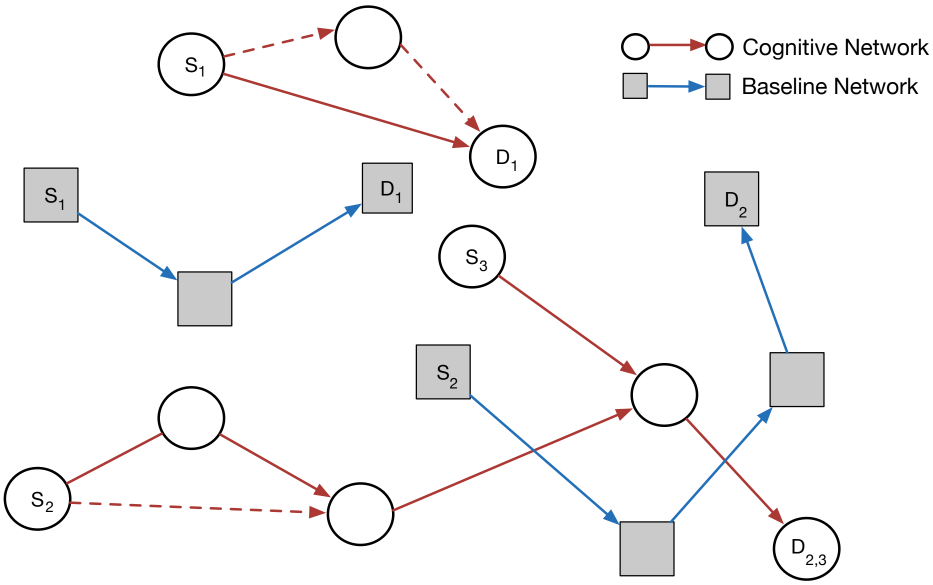

Figure 4.1: The "elastic" network: cross-layer optimized cognitive links (red-colored) are co-located with static/baseline links (blue-colored) that implement a layered network protocol stack. Solid lines depict selected routes from source s to destination d, while dashed lines depict alternate routes. ©2018 IEEE.

nodes have pre-assigned unique code-waveforms and routes, while cognitive network nodes jointly optimize modulating code-waveforms and selected routes in a continuous fashion on a hop-by-hop basis.

The transmitted signal for the link (i, j) is as given in (3.1) and (3.2). The received signal after carrier downconversion at $f_c + \Delta f_{ij}$ at the j-th cognitive receiver is written as

$$y_{ij}(t) \triangleq \sum_{m=0}^{M-1} \tilde{h}_{ij}[m] \sum_{n=0}^{N-1} b_i[n]\psi_{ij}(t - (m + nL)T_c) \cdot e^{-j2\pi\Delta f_{ij}t} + p(t) + z(t) \tag{4.1}$$

where Δf_{ij} is the carrier frequency offset (CFO) due to manufacturing imperfections between the local oscillators of the i-th transmitter and j-th receiver. Additive white Gaussian noise and interference from co-located baseline and cognitive transmitters is denoted by $z(t)$ and

$p(t)$, respectively.

Both baseline and cognitive networks implement a CDMA-based random access MAC protocol, whereby a network node accesses the channel as soon as there are packets in its queue. However, non-zero cross-correlation between different code-waveforms at co-located wireless links may result in multiple-access interference (MAI). In addition, channelization of the available bandwidth may be different at each hop in a multi-hop path, while at the same time network traffic dynamics and routing of traffic flows may frequently change. Therefore, controlling the interaction between routing and code-waveform design at the physical/link layer is of fundamental importance. Each network node maintains a separate queue for each session d for which it is either a source or an intermediate node. The queue size at the i-th network node is given in (3.10).

4.3.2 Cross-layer Cognitive Adaptation

As discussed in Section 3.2.3, a centralized throughput-optimal controller can jointly assign transmit energy, spreading code-waveforms, and routes to each node in the network though this centralized optimization is generally NP-hard. Therefore, this work uses a distributed joint waveform and route optimization algorithm driven by locally-collected information at the cognitive network nodes [24]. Assuming fixed network topology and transmit energy E_i, the i-th backlogged node first maximizes a local utility function $U_{ij} = C_{ij} \cdot \Delta Q'_{ij}$ over all feasible next hops j by optimizing modulating waveforms $\mathbf{s}_{ij}$ based on locally collected spectrum information. This formulation uses a modified definition of differential backlog

$$\Delta Q'_{ij}(t) \triangleq \begin{cases} Q'_i(t) - Q'_j(t), & \text{if } Q'_i(t) \neq Q'_j(t) \\ 1, & \text{otherwise} \end{cases} \tag{4.2}$$

where $Q'_i(t) = \sum_d Q_i^d(t)$. Then, each node will access the channel by selecting the waveform that optimizes its local utility. Particularly, the i-th backlogged node, at each decision period, implements the following algorithm:

1) Find the set of feasible next hops for each session d that are neighbors to node i.

2) Maximize link-capacity C_{ij} by optimizing code-waveforms $\mathbf{s}_{ij}$ for each of the feasible next hops.

3) Select as next hop j^* the one with maximal utility U_{ij}.

The algorithm returns the selected next hop j^* according to the queue size and capacity information reflected in the utility function U_{ij}. The optimization is carried out at each successive next hop to form a multi-hop path terminating at the destination. If the destination is in the transmission range of the transmitter (either a source or an intermediate hop for that session), the differential backlog between the transmitter and the destination is no less than the differential backlogs between the transmitter and any other nodes, because the queue length of the destination is zero. Fig. 4.2 depicts the steps of the distributed algorithm. Low computational complexity algorithms for solving the waveform optimization problem in the second step of the algorithm are proposed in Section 3.5. At the last step of the algorithm, each cognitive network (source or intermediate) node calculates utility values U_{ij} for all candidate hops and selects the hop with maximum utility.

4.4 System Design Considerations

This section describes the system design considerations and challenges related to the implementation and deployment of the proposed distributed algorithm in a large-scale software-defined testbed. Specifically, this section summarizes developments with respect to

Cognitive Code-Waveform and Routing Algorithm

```
At backlogged node $i$
for each backlogged session $d$ do
    for each candidate next hop $j$ do
        Calculate link capacity $C_{ij}$ by optimizing $\mathbf{s}_{ij}$
    end for
end for
Select next hop $j^* = \arg\max_j C_{ij} \cdot \Delta Q'_{ij}$
Return $\left[\mathbf{s}^*_{ij}, j^*\right]$
```

Figure 4.2: Pseudocode for the cognitive code-waveform and routing algorithm.

modulation and error-correction coding schemes, frame design, maximum-SINR filtering, medium access control, networking, and application layer protocols.

4.4.1 Modulation & Error Correction Encoding

Both networks may utilize different orders of phase-shift-keying (PSK) and quadrature-amplitude-modulation (QAM) schemes, such as BPSK, 4/8/16/32/64-PSK/QAM and select convolutional error-correcting codes that are punctured according to the coding rate.

4.4.2 Frame Detection & Synchronization

The byte format of the transmitted data frame is depicted in Fig. 4.3. Data frames are prefixed with NET-layer headers that contain source, next hop, and destination MAC addresses, as well as a frame number. Subsequently, the frames are appended with a 32-bit cyclic-redundancy check (CRC) for error detection and a repetitive pattern of 4-bytes that contain information regarding the whitener offset and frame length. Whitener offset information is utilized by a randomizer block at the PHY layer to XOR payload bytes with a pseudo-noise (PN) sequence to evenly distribute power across the available bandwidth. Finally, at the PHY layer, each payload data frame is appended with a randomly-generated

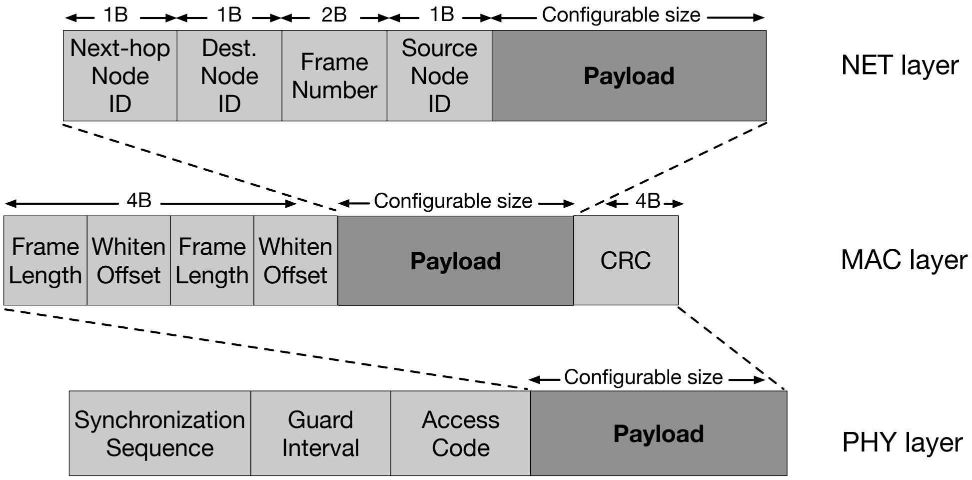

Figure 4.3: Data frame structure. ©2018 IEEE.

access code training sequence unique to each (i, j)-th link (used for fine time-synchronization and channel estimation), a guard-band interval, and a frame synchronization/detection sequence. Table 4.1 presents the PHY-layer parameters of the data link.

A synchronization/detection sequence based on chirp sequence keying (CSK) known a priori at the receiver is utilized. Chirp sequences are selected due to their superior correlation characteristics in low SINR and multipath environments [115, 116]. Frame detection sequences consisting of four sub-chirps are generated [116]. Every sub-chirp is a frequency ramp with either increasing (up-chirp) or decreasing (down-chirp) frequency in the upper or lower sideband of the channel.Table 4.2 depicts the chirp synchronization sequence parameters.

4.4.2.1 Presence of a Frame

The beginning of a data frame is detected if the peak value of the normalized cross-correlation between the received signal and the chirp synchronization sequence exceeds a predefined threshold value. Fig. 4.4 illustrates the sub-chirp pattern for link (i, j) and the output of the frame correlator with the chirp synchronization sequence from over-the-air indoor

Table 4.1: Data frame parameters

Parameter	**Variable**	**Value**
Modulation schemes	$\mathcal{A}$	PSK/QAM
Roll-off factor (SRRC)	α	0.35
Sampling frequency	F_s	1 MSps
Guard interval (in samples)	N_g	100
Code-waveform length	L	8
Code-waveform duration	T_c	4 μs
Num. of samples per code	N_{spc}	4
Num. of payload symbols	N_p	1024
Num. of access-code symbols	N_{ac}	32

Table 4.2: Chirp synchronization sequence parameters

Parameter	**Variable**	**Value**
Initial frequency	f_0	$\pm 3.15 \cdot 10^6$ Hz
Sub-chirp sampling frequency	F_{sub}	32 MSps
Frequency sweeping ratio	μ	$\pm 14.62 \cdot 10^{12}$
Num. of samples per sub-chirp	N_s	38

SDR measurements. After acquiring the beginning of a data frame, the received signal (which includes access code and payload samples) is pulse-matched filtered, sampled over the multipath-extended duration of $(NL + M - 1)T_c$ seconds, and gathered into vectors

$$\begin{aligned} \mathbf{y}_{ij}[n] \triangleq y_{ij}(kT_c), &\quad k = nL, ..., (nL + L_M - 1), \\ \text{for} &\quad n = 0, \ldots, N-1. \end{aligned} \tag{4.3}$$

with $L_M \triangleq L + M - 1$. The rest of this section considers frequency synchronized radio transceivers, thus Δf_{ij} is considered to be negligible. The chirp synchronization sequence alone cannot accurately determine timing. Therefore, upon the detection of a frame synchronization peak fine synchronization at the waveform-level is done as a separate step.

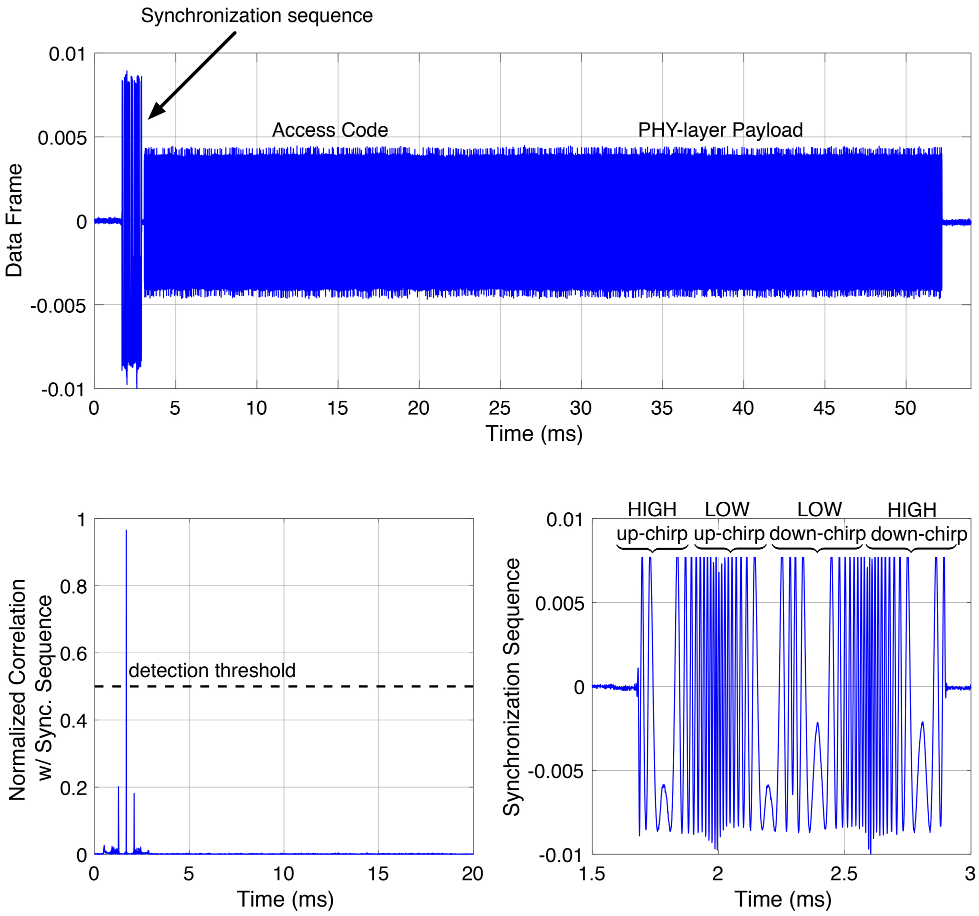

Figure 4.4: Received data frame snapshot (top). Normalized cross-correlation of the received data frame with the chirp synchronization sequence (bottom). ©2018 IEEE.

Fine timing synchronization is performed with a matched filter that cross-correlates the received symbols with the access code training sequence unique to each link and known at the receiver a priori. The same access code sequence is used to estimate multipath channel coefficients.

4.4.2.2 Absence of a Frame

If a distinct peak at the output of the frame correlator is not detected, it is assumed that the received signal contains only noise and interference ("disturbance"). Disturbance samples as measured at the j-th receiver node are similarly pulse-matched filtered and sampled

$$\begin{aligned} \mathbf{d}[n] &\triangleq p(kT_c) + z(kT_c) \\ &= \mathbf{p}[n] + \mathbf{z}[n], \quad k = nL, ..., (nL + L_M - 1) \end{aligned} \tag{4.4}$$

where $\mathbf{p}[n] \in \mathbb{C}^{L_M}$ models colored interference with autocorrelation matrix $\mathbf{R}_{\mathrm{P}} \triangleq \mathrm{E}\{\mathbf{p}[n]\mathbf{p}^H[n]\} \in \mathbb{C}^{L_M \times L_M}$ and $\mathbf{z}[n] \in \mathbb{C}^{L_M}$ denotes zero-mean additive white Gaussian noise with covariance $\sigma^2 \mathbf{I}_{L_M}$. The autocorrelation matrix of $\mathbf{d}[n]$ is defined as

$$\mathbf{R}_{\mathrm{I+N}} \triangleq \mathrm{E}\left\{\mathbf{d}[n]\mathbf{d}^H[n]\right\} = \mathbf{R}_{\mathrm{P}} + \sigma^2 \mathbf{I}_{L_M}. \tag{4.5}$$

In practice, $\mathbf{d}[n]$ is used to recursively update an estimate of the inverse autocorrelation matrix $\widehat{\mathbf{R}}_{\mathrm{I+N}}^{-1}$ as

$$\widehat{\mathbf{R}}_{\mathrm{I+N}}^{-1}[n] \triangleq \frac{1}{\beta}\left[\widehat{\mathbf{R}}_{\mathrm{I+N}}[n-1] - \frac{\widehat{\mathbf{R}}_{\mathrm{I+N}}^{-1}[n-1]\mathbf{d}[n]\mathbf{d}^H[n]\widehat{\mathbf{R}}_{\mathrm{I+N}}[n-1]}{\beta + \mathbf{d}^H[n]\widehat{\mathbf{R}}_{\mathrm{I+N}}^{-1}[n-1]\mathbf{d}[n]}\right] \tag{4.6}$$

where $\widehat{\mathbf{R}}_{\mathrm{I+N}}^{-1}[0] = c\mathbf{I}_{L_M}$, $c \ll 1$ and $\beta \in [0, 1]$ denotes a “forgetting factor”.

4.4.3 Filtering & Bit Recovery

The baseband received signal vector in (4.4) is equivalent to

$$\mathbf{y}_{ij}[n] = \mathbf{H}_{ij}\mathbf{s}_{ij}b_i[n] + \mathbf{d}[n], \quad n = 0, \cdots, N-1 \tag{4.7}$$

where $\mathbf{H}_{ij}$ is the multipath fading channel matrix between transmitter i and receiver j given by

$$\mathbf{H}_{ij} \triangleq \sum_{m=0}^{M-1} \tilde{h}_{ij}[m] \begin{bmatrix} \mathbf{0}_{m \times L} \\ \mathbf{I}_{L \times L} \\ \mathbf{0}_{(M-m-1) \times L} \end{bmatrix} \in \mathbb{C}^{L_M \times L}. \tag{4.8}$$

Assuming knowledge of the true autocorrelation matrix $\mathbf{R}_{\mathrm{I+N}}$ and multipath channel coefficients $\mathbf{H}_{ij}$, the linear filter at the receiver that exhibits maximum output SINR [53] is given by

$$\mathbf{w}_{\mathrm{max-SINR}}(\mathbf{s}_{ij}) \triangleq \frac{\mathbf{R}_{\mathrm{I+N}}^{-1}\mathbf{H}_{ij}\mathbf{s}_{ij}}{\mathbf{s}_{ij}^T\mathbf{H}_{ij}^H\mathbf{R}_{\mathrm{I+N}}^{-1}\mathbf{H}_{ij}\mathbf{s}_{ij}} \tag{4.9}$$

and will attain an SINR at the output of the filter equal to

$$\mathrm{SINR}_{ij}(\mathbf{s}_{ij}) \triangleq \mathbf{s}_{ij}^T\mathbf{H}_{ij}^H\mathbf{R}_{\mathrm{I+N}}^{-1}\mathbf{H}_{ij}\mathbf{s}_{ij} = \mathbf{s}_{ij}^T\mathbf{P}_s\mathbf{s}_{ij} \tag{4.10}$$

where $\mathbf{P}_s \triangleq \mathbf{H}_{ij}^H\mathbf{R}_{\mathrm{I+N}}^{-1}\mathbf{H}_{ij} \succ 0$. Knowledge of access code training symbols is utilized at the receiver to estimate the SINR at the output of the maximum-SINR filter. The error vector magnitude (EVM) of the soft-decoded received symbols is given by

$$\mathrm{EVM}_{ij} = \sqrt{\frac{\frac{1}{N_{ac}}\sum_{n=0}^{N_{ac}-1}\left|\mathbf{w}_{\mathrm{max-SINR}}^H(\mathbf{s}_{ij})\mathbf{y}_{ij}[n] - b_i[n]\right|^2}{\frac{1}{N_{ac}}\sum_{n=0}^{N_{ac}-1}|b_i[n]|^2}}. \tag{4.11}$$

Consequently, a quality estimate of SINR for link (i, j) is given by $\widehat{\mathrm{SINR}}_{ij} \triangleq 1/\mathrm{EVM}_{ij}^2$. Finally, the receiver detects the k-th transmitted symbol by minimizing the Euclidean distance between the maximum-SINR filtered signal

$$\widehat{b}_i[n] \triangleq \underset{b_i[n]\in\mathcal{A}}{\operatorname{argmin}} \left|\mathbf{w}^H_{\max-\mathrm{SINR}}(\mathbf{s}_{ij})\mathbf{y}_{ij}[n] - b_i[n]\right|^2 \quad \text{for} \quad n = 0, \ldots, N-1. \tag{4.12}$$

4.4.4 Medium Access Control

Each node accesses the channel using a random-access ALOHA-like CDMA-based MAC scheme for each data frame and dynamically optimizes waveforms at each cognitive link on a hop-by-hop basis based on the algorithm described in Fig. 4.2. Baseline network links are assigned to unique code-waveforms that remain fixed. The proposed protocol is efficient both in environments where carrier sensing cannot resolve the hidden/exposed terminal problem and in networks with long-distance communication, high data rates, and short frames. Additionally, no handshaking mechanism for virtual carrier sensing is utilized, thus powerful MAI from asynchronous transmissions is resolved with retransmissions of data frames that are not successfully acknowledged by the receiver.

At the MAC layer, a data frame is received successfully if the number of errors in the decoded information bits is less than or equal to the maximum number of (correctable) bit errors allowed by the FEC module. If no FEC is present, then the data frame is successfully received when all information bits are detected correctly. Subsequently, if the decoded data frame is detected correctly, an acknowledgment (ACK) frame is sent to the corresponding transmitter. Alternatively, if the received data frame contains errors, the transmitter is notified for a retransmission with a negative acknowledgment (NACK) frame. Both ACK and NACK frames contain queue size information to allow transmitting nodes to make routing decisions. Fig. 4.5 describes the structure of the ACK/NACK frames and the size of each data field in bytes.

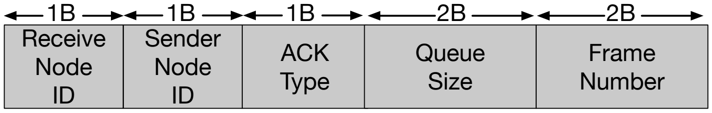

Figure 4.5: Structure of acknowledgment (ACK/NACK) frames. ©2018 IEEE.

4.4.5 Networking & Application Layers

Each network node continuously checks the queue that is maintained for each session d at the NET layer for either existing (if it is a source node) or new incoming (if it is an intermediate node) frames. Subsequently, each transmitting (source or intermediate) node in the cognitive network calculates utility values U_{ij} for each feasible next hop based on queuing information and spectrum dynamics that are received from acknowledgment and feedback/control packets (discussed in Section 4.4.6). Cognitive network nodes with higher utility U_{ij} will have higher probability to be selected for transmission. If the destination is in the transmission range of the transmitting (either source or intermediate) cognitive network node, the differential backlog between the transmitter and the destination is no less than the differential backlogs between the transmitter and any other nodes, because the queue length of the destination is zero. As a result, lightly backlogged nodes (with smaller differential backlog) and higher link capacity are selected as intermediate relays and receive most of the network traffic. On the other hand, network nodes in the baseline network consider fixed route and waveform allocation.

The proposed network node architecture can accommodate end-to-end multimedia sessions, such as digital audio and video sessions from source s to destination d. Destination network nodes implement a double-buffering architecture that enables reordering of chunks of received data frames. Consequently, the nodes compensate out-of-order frame arrivals that may appear due to dynamically selected multipath routes toward the destination network node.

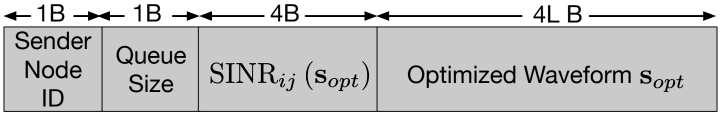

Figure 4.6: Feedback/control frame structure. ©2018 IEEE.

4.4.6 Feedback Channel

Cross-layer dynamic waveform and route adaptation is implemented in practice based on a closed-loop feedback/control link that carries the optimized waveform and post-filtering link SINRs to the transmitting (source or intermediate) cognitive network nodes. The set of feasible next hops at each cognitive network node can be obtained by either neighbor discovery protocols or from position information (e.g. GPS) of each node. Receiving (intermediate or destination) nodes, that are candidates to be selected as next hops, send feedback/control frames to an associated transmitting node at time intervals that are either preprogrammed by the user or calculated in an autonomous fashion. The structure of the feedback link frames is illustrated in Fig. 4.6. Transmitting nodes can take decisions on the modulating waveform and next hop based on locally collected utility information from neighboring nodes according to the algorithm described in Fig. 4.2. Finally, waveform and routing decisions taken at each transmitting node are broadcasted to the rest of the network. A flow chart representation of the system design discussed in this section is given in Fig. 4.7.

4.5 Hardware and Software Processing

In this section, hardware and software processing challenges are discussed for the implementation and deployment of these algorithmic developments in a large-scale cross-layer-reconfigurable software-defined radio testbed. Software implementation of the algorithmic developments described in the sections above are hosted by a software-radio framework that

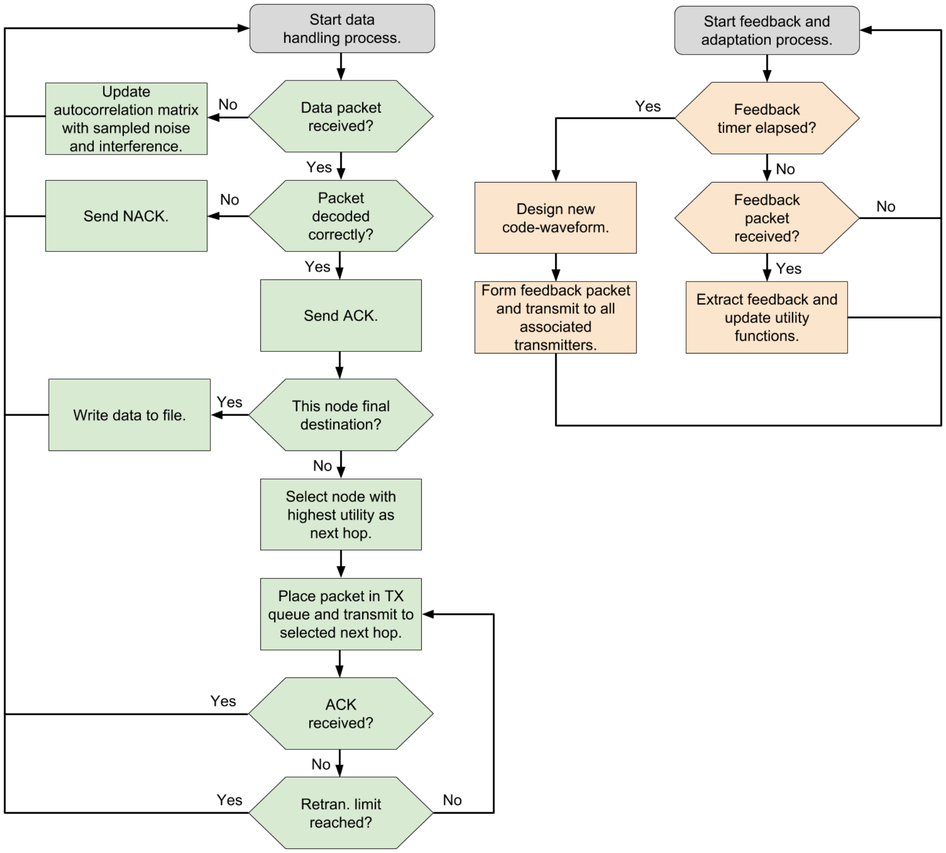

Figure 4.7: Flow chart showing the process of data reception and cognitive functions executed at each receiver node. ©2018 IEEE.

runs entirely in a GPP and enables self-optimization and real-time reconfiguration at PHY, MAC, and NET layers of the protocol stack. In its current instantiation, the framework is implemented in a host-PC and takes advantage of the modularity and flexibility of the GNU Radio open-source framework and the multi-core processing libraries supported by Python.

4.5.1 PHY-layer Baseband Processing

The GNU Radio open-source software application-programming interface (API) is used to implement new signal processing blocks and applications in C++ and Python. A collection of connected blocks with a particular flow of samples from a source towards a sink is called flowgraph. A great advantage of GNU Radio is that apart from real-time signal processing of samples from an SDR, it can also be used for PHY-layer simulations. This is easily possible by looping back the generated sample stream into the receiver without interfacing actual radio hardware. The GNU Radio framework handles tasks such as memory allocation and sample transfer between signal processing blocks in a stream-based fashion. This work relies on GNU Radio mechanisms such as stream tags and message ports to enable packet-based processing at each network node.

Stream tags offer the ability to align metadata with specific samples in a stream to denote information such as packet boundaries. A more generic asynchronous message passing mechanism uses protocol data units (PDUs) to transfer an arbitrarily large chunk of data and metadata between any set of GNU Radio modular blocks with the use of message ports. Message ports follow a publisher/subscriber model where receive queues exist at message input ports.

Fig. 4.8 provides an abstract illustration of the transmit and receive flowgraphs in GNU Radio. Multiple instances of transmit and receive flowgraphs may run in parallel at each network node. User Datagram Protocol (UDP)-type message ports are utilized to exchange PHY-layer related information with the protocol execution logic of MAC and NET-layer functionalities. More specifically, upstream information to the MAC layer is comprised of payload bytes, post-filtering SINR estimates, and optimized code-waveform designs at the receiver flowgraph. Payload bytes, waveform updates, and user-driven decisions for waveform adaptation are exchanged downstream from MAC to PHY-layer blocks at the transmitter and receiver flowgraphs.

NET-layer data frames are first inserted to the transmitter flowgraph in the form of PDUs. Subsequently, data frames are converted to stream-based samples and are appended with MAC and PHY-layer headers as described in Section 4.4.2. Prior to streaming samples to the digital-to-analog converter (DAC) and the SDR front-end device, the samples undergo

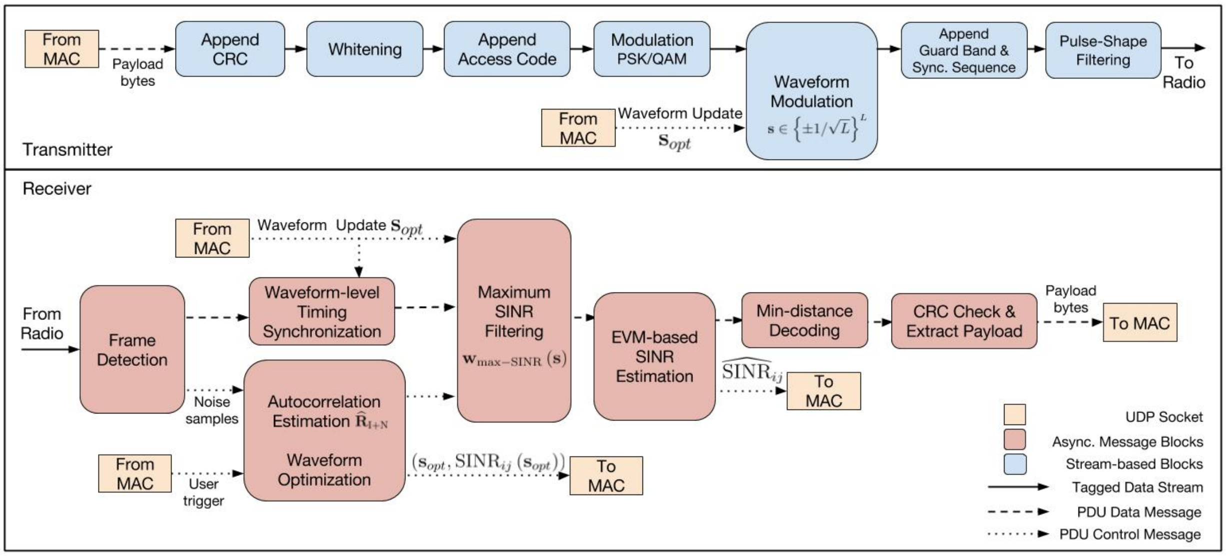

Figure 4.8: PHY- and lower-MAC (transmitter and receiver) signal processing blocks in GNU Radio. Both blocks and connections to radio front-end(s) and upper networking layers (i.e. MAC) are the same for both static and cognitive network nodes. ©2018 IEEE.

continuous functions such as waveform modulation and pulse-shape filtering. Stream tags are used to denote the beginning and the end of a data frame.

The receiver implements frame detection as a continuous streaming block that operates on the stream of the incoming samples from the analog-to-digital converter (ADC) of the SDR. Detected frames are formatted as PDUs and are passed through waveform-level synchronization, channel estimation, maximum-SINR filtering, and minimum-distance detection operations. If no data frame is detected, compound disturbance (noise and interference) samples are used to maintain an up-to-date estimate of the inverse autocorrelation matrix (as discussed in Section 4.4.2). At regular time intervals a (user-defined or autonomous) decision mechanism at the NET layer triggers the waveform optimization process. The optimized waveform and post-filtering SINR values are communicated to the upper layers to create the feedback/control link frame. The optimized waveform is fed back to both the transmitter and receiver PHY-layer in the form of a PDU to update waveform-dependent PHY-layer signal processing blocks in GNU Radio.

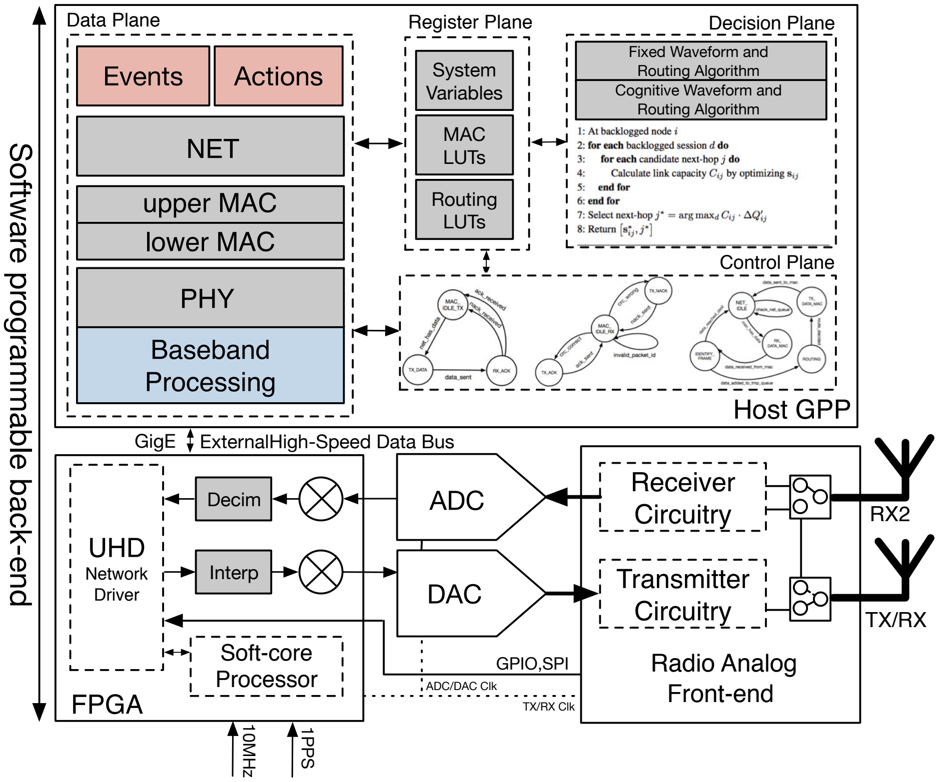

```
1: At backlogged node $i$
2: for each backlogged session $d$ do
3:     for each candidate next-hop $j$ do
4:         Calculate link capacity $C_{ij}$ by optimizing $\mathbf{s}_{ij}$
5:     end for
6: end for
7: Select next-hop $j^* = \arg\max_d C_{ij} \cdot \Delta Q'_{ij}$
8: Return $[\mathbf{s}^*_{ij}, j^*]$
```

Figure 4.9: Hardware and software architecture of the proposed cognitive software-radio platform. ©2018 IEEE.

4.5.2 Cross-Layer Processing

The software architecture of each network node is divided into four interacting planes: *decision*, *control*, *data*, and *register* [117] that enable separation of data processing, logical control, and decision-making mechanisms from the execution of the protocol stack. Fig. 4.9 depicts the software/hardware architecture of the proposed cognitive radio platform. Data processing and handling of data and control queues takes place in the *data* plane. The execution logic of data processing in the *data* plane is controlled by three execution engines that are defined in the *control* plane. Execution engines contain finite state machines (FSMs) that implement the execution logic of the transmit and receive MAC and NET-layer protocols. Fig. 4.10 depicts the three FSM designs comprised of symbolic states and

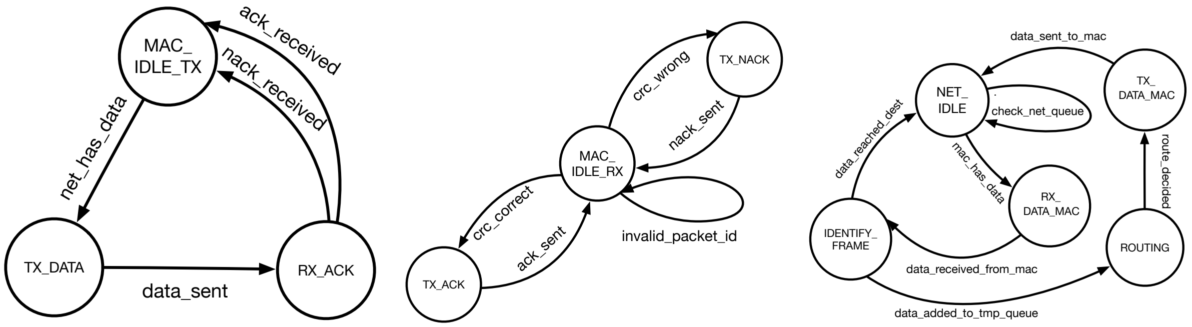

(a) Upper MAC-layer Transmit FSM.

(b) Upper MAC-layer Receive FSM

(c) NET-layer FSM

Figure 4.10: Upper MAC- and NET-layer FSM architectures executed at the each network node. State transitions are executed based on the definition of events that are depicted in the arches of the FSMs. ©2018 IEEE.

extended state transitions that are defined as a triplet of events, conditions, and actions [117]. Actions are designed to trigger *data* plane functionalities, while events occur as a result of *data* plane actions. Actions and events (as depicted in the FSM state-transitions of Fig. 4.10) are primitive building blocks that can be used to decompose multiple wireless networking protocols. As a result, the execution of the protocol stack in the *data* plane can be easily reconfigured by simply changing the order of execution of the blocks of actions and events. The *register* plane stores and manages access to system parameters and state variables at different network layers, look-up-tables (LUTs) for the implementation of different MAC and routing protocols, and control messages such as queue updates from next-hop network nodes.

The proposed software-radio framework is implemented in a host GPP using Python's multi-processing library to allow multiple processes to run in parallel by distributing processing across multiple computing resources. Queues are used to buffer and transfer data bytes between processes in a thread-safe manner. The framework is programmed in a modular manner such that multiple instances of each plane can be generated and run in parallel to handle data that may arrive from multiple network nodes. Intermediate network nodes must be capable of processing frames that may arrive from more than one neighbor network nodes at the same time. In GNU Radio separate instances of transmit and receive signal processing flowgraphs are initialized for communication with candidate next-hop neighbor nodes. Similarly, multiple instances of the *data*, *control*, *register*, and *decision* planes are initialized and process frames received from different sources in an independent fashion. In the *data* plane a dedicated handler is initialized for each UDP socket to control communication between lower-layer baseband signal processing blocks in GNU Radio and the rest of the *data* plane blocks. Streams of transmitted/received bytes are placed in a queue and handled by *data* plane/GNU Radio processes. In the same way, asynchronous waveform updates and post-filtering SINR messages are communicated to the upper-layers of the network protocol stack via dedicated handlers for UDP sockets.

4.5.3 Distributed Decision Making

The proposed software-radio framework incorporates a *decision* plane that enables on-the-fly reconfiguration of user-defined decision algorithms without affecting the execution of the protocol stack. The *decision* plane is interfaced with the *control* and *data* planes through the *register* plane and contains a set of decision algorithms for fixed and cognitive waveform and routing allocation that can be executed in parallel. Algorithms can be executed in a synchronous or asynchronous fashion and modify parameters across PHY, MAC, and NET layers of the protocol stack without influencing the on-going protocol execution logic. Both *control* and *data* planes can reconfigure their execution logic by checking the updated parameters in the *register* plane. The *decision* plane is optional upon design therefore, it may be enabled or disabled to accommodate centralized or distributed control of cross-layer optimized parameters.

4.5.4 Computational Performance

Improved computational performance through threaded operation and optimized instructions is essential for the software implementation of the proposed cross-layer optimized transceiver that is entirely hosted by a GPP. Before this project was started, there was no transmitter/receiver design available in GNU Radio that implements adaptive code-waveform-based multiple access. Therefore, it was unclear whether it was possible to realize and execute the proposed cross-layer optimized transceiver design in real-time on a normal laptop or desktop PC or if splitting functionalities between the GPP and the FPGA would be required. For small signal bandwidths, transmitted/received streams of data are processed in real-time and the inherent capabilities of GNU Radio signal processing blocks are used to distribute the load between the cores of a GPP.

Real-time processing implies that the average processing time per sample is smaller than the sample duration, thus the transceiver does not drop samples, which may lead to wrong interpretations of measurement results. To further speed up computations, the individual blocks exploit vectorized instructions that multicore CPUs provide through single-input multiple-data (SIMD) extensions like MMX, SSE, and AVX. With GNU Radio, these instructions are accessed through the vector-optimized library of kernels (VOLK) [1,28], which provides optimized implementations of common signal processing functions.

4.5.5 Scalability/Interoperability

The architectural components of the proposed software-radio framework enable either network-level simulations by re-directing the generated NET and MAC-layer frames to a UDP/TCP socket instead of GNU Radio transmitter/receiver or PHY-level simulations by looping back the generated sample stream in GNU Radio into the receiver without interfacing an actual SDR hardware. GNU Radio aids simulation setup by providing

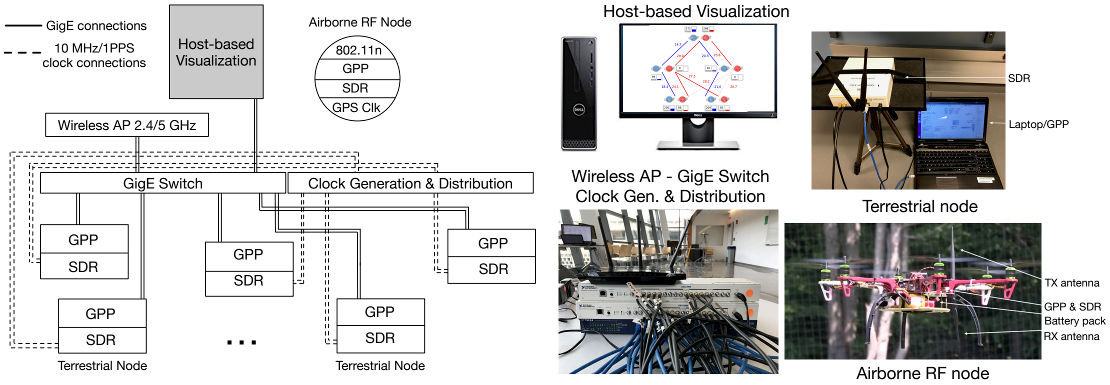

(a) (b)

Figure 4.11: Testbed implementation overview: (a) Data command and control GigE links and clock distribution connections for both terrestrial and airborne SDR platforms. (b) Assembled off-the-shelf airborne and terrestrial SDRs with data command/control, clock generation/distribution, and host-based visualization units. ©2018 IEEE.

models for hardware impairments like phase noise and clock drift, as well as propagation environments like additive white Gaussian noise (AWGN), Rayleigh, and multipath fading. Interoperability tests are conducted with different SDR platforms and GPP architectures (such as Intel i5/i7, and ARM Cortex-A15). Table 4.3 summarizes the SDR platforms and host-PC models and features that are utilized for both simulation and experimental testing.

4.6 The "Elastic" Testbed Implementation

In this section, system implementation details for the deployment of an "elastic" network testbed comprising of co-located terrestrial cognitive and baseline network nodes that operate in the presence of an airborne RF interferer are discussed. Fig. 4.11a presents a testbed schematic that depicts data command/control and clock-synchronization connections in the software-defined testbed. Fig. 4.11b provides illustrations of the testbed hardware units, which include terrestrial and airborne modular SDR, clock generation/distribution, and host-based visualization platforms. Table 4.3 lists the selected hardware platforms with further details.

4.6.1 SDR Platforms

Both cognitive and baseline network nodes in the “elastic” network are based on the Ettus Research family of Universal Software Radio Peripherals (USRPs). USRP SDRs are connected to a Linux-based host-PC with either an external high-speed Gigabit Ethernet (GigE) or USB 3.0 data interface. All models of the USRP family can interface to the proposed cognitive radio framework through the USRP Hardware Driver (UHD) software API that acts as a host communication driver for controlling the SDRs.

4.6.1.1 Terrestrial Nodes

Terrestrial nodes are based on the USRP N-series SDRs. Each SDR contains a 14-bit dual 100 MSps ADC, a 16-bit dual 400 MSps DAC, a Xilinx 3A-DSP FPGA-based motherboard, and a 40 MHz bandwidth daughterboard that supports a variable center frequency from 400 MHz to 4.4 GHz and TX power of 20 dBm. Received baseband samples at the SDR are sent to the host PC via a GigE data bus in the format of 4 bytes per complex sample, therefore the maximum data rate over GigE is $\frac{125\text{ MB/s}}{4\text{ B/sample}} = 31.25$ MSps (reduced to 25 MSps due to overhead [1]).

4.6.1.2 Airborne Nodes

Airborne network nodes require a more compact and lightweight SDR platform. Therefore, airborne nodes are equipped with USRP B-series SDRs that offer a small-form-factor, fully integrated, two-channel radio with continuous RF coverage from 70 MHz to 6 GHz. Baseband samples from the SDR are transferred to an ARM-based single-board computer through a USB 3.0 connection. Both the radio and host-PC offer a combined payload of less than 2 kg

Table 4.3: Selected Hardware Components

Type	**Model**	**Features**
Terrestrial SDR	Ettus USRP N210 & SBX-40	1 Xilinx Spartan-3A-DSP FPGA 100 MSps ADC, 400 MSps DAC GigE connectivity 1 TX/RX and 1 RX RF front-ends 40 MHz bandwidth tunable from 400 MHz to 4400 MHz
Host Computer	Toshiba Satellite/Dell Optiplex	Laptop/Desktop PCs with Intel i5/i7 Processor 4 up to 8 core CPUs, 8 up to 16 GB RAM Software configuration: Ubuntu 16.04, GNU Radio 3.7.10, UHD 3.11
Airborne SDR	Ettus USRP B210	1 Xilinx Spartan-6 XC6SLX150 FPGA 61.44 MSps ADC/DAC USB 3.0 connectivity 2 TX and 2 RX RF front ends 56 MHz RF bandwidth tunable from 70 MHz to 6.0 GHz
Airborne Host Computer	Hardkernel ODROID-XU4	ARM Cortex-A15, 2 GHz & A7 Octacore CPUs 2 GB LPDDR3 RAM PoP stacked 16 GB eMMC5.0 HS400 flash storage Software configuration: Ubuntu 16.04, GNU Radio 3.7.10, UHD 3.11
Ref. Clock Generation & Distribution	Ettus OctoClock-G CDA-2990	GPS-disciplined fully integrated timing source 8-way distribution (10 MHz/1 PPS)
Ref. Clock Distribution	Ettus OctoClock CDA-2990	8-channel time and frequency distribution circuit Requires external 10 MHz/1 PPS reference source
Switch	Netgear	24-port Gigabit Ethernet Switch
Wireless Access Point	TP-Link Panda	Dual-band 2.4/5 GHz TP-Link AC 1200 access point Dual-band 2.4/5 GHz Panda N 600 USB dongles
Airborne Vehicle Platform	Air Force Research Lab (Rome, NY)	Custom-built hex-rotor with 550 frame Requires 11200 mAh battery pack Flight time: 18 min with 2 kg payload

that can be easily mounted to the airborne vehicle platform (Table 4.3) and powered by a compact battery pack.

4.6.2 Testbed Operation

4.6.2.1 Command & Control

Portable laptop PCs are used to control terrestrial SDRs. Laptops are positioned in a central location (i.e. command & control center) and control the SDRs through a GigE switch. The GigE switch is used to route ACK/NACK frames and feedback/control frames between network nodes. A dedicated desktop PC is utilized to store and display status-update messages from the "elastic" network nodes which are transmitted periodically to the desktop PC through the GigE switch. During network deployment and testing it is also important to remotely control the SDR on the airborne interfering node. Particularly, a controller should be able to start, stop, and reconfigure PHY-layer parameters such as the code-waveform and transmission power during flight. Command and control of the SDR on the airborne node is achieved by remote access to the airborne host-PC over an 802.11n-based wireless control link. The wireless control link is established with a wireless access point on the ground and a USB-dongle on the airborne platform. The wireless control link operates at 5 GHz to avoid interference with the flight controller.

4.6.2.2 Host-based Visualization

Cognitive and baseline network nodes can periodically send status-update messages to a desktop PC to report modifications in parameters such as post-filtering link SINR, frame queue sizes, code-waveform updates, and selected routes. Status-update messages are displayed in real-time on a host-based visualization that is built in Python. Display messages are time-stamped and stored at the desktop PC for post-processing offline analysis.

A screenshot of the host-based visualization for the “elastic” network testbed in an outdoor environment is depicted in Fig. 4.16c. A bar graph next to each network node in the visualization demonstrates the number of data frames waiting for transmission in the network node queue. On the other hand, as the destination node does not have a network queue, the bar graph depicts the total number of packets that have been correctly received from the source of each session. Candidate routes in the cognitive network are depicted as dashed lines, while active routes for each session are displayed as solid lines.

4.6.3 Synchronization

To compensate for time and frequency clock drifts between terrestrial SDRs, a GPS-disciplined clock generation and distribution circuit are used. Particularly, one GPS-disciplined Ettus Research Octoclock module (as depicted in Fig. 4.11) generates and distributes high accuracy 10 MHz and 1 PPS signals to seven SDR nodes using SMA cables. The eighth output of the OctoClock is utilized as an external reference to a second OctoClock unit which can distribute clock reference signals to eight additional SDRs. Reference clock signals can discipline SDRs to a frequency stability of 0.01 ppm. Airborne SDR nodes can optionally be equipped with on-board mounted GPS-disciplined clock units that offer 10 MHz clock and 1 PPS reference signals and can achieve a global timing alignment of 50 ns in locked condition. However in the context of this work, the airborne interfering node operates without any requirement of either time or frequency synchronization to the rest of the terrestrial network nodes.

4.7 Experimental Proof-of-Concept Results

This section describes the design details of three experimental scenarios toward the validation of the “elastic” network concept in both indoor and outdoor environments. Each scenario addresses a challenging aspect of communication in UAV networks, as identified in the literature (see Section 4.1) but is also applicable to cognitive radio networks. Experimental proof-of-concept results are presented for both testbed deployments and evaluate the "elastic" testbed in terms of end-to-end network throughput performance, average post-filtering SINR at selected links, average aggregate queue size at the intermediate nodes, and selected routes.

4.7.1 Scenarios

In each scenario, two independent but co-located networks of terrestrial nodes are built. The first network operates on statically assigned waveforms and fixed routes. The second network consists of cognitively cross-layer optimized wireless links that are capable of dynamically adapting code-waveforms and routes, as discussed in Section 4.3.2. Multimedia traffic flows for both cognitive and baseline networks are carried over unicast sessions from a source node s to a destination node d. In both networks, uncoded transmissions of multimedia that are 4-QAM modulated are considered. The rest of the data-link parameters can be found in Table 4.1.

4.7.1.1 Network Coexistence

The first testbed scenario evaluates the simultaneous operation of two independent wireless networks coexisting at the same location, time, and frequency. Lack of network-wide backhaul links and centralized common control in UAV networks [8] leads to distributed self-reconfigurable solutions to avoid multiple-access interference. Baseline network nodes are initialized on a static set of code-waveforms and routes. Digital audio or video traffic sessions are carried over a layered network protocol stack. Baseline network operation is then disrupted by the deployment of a second network that is co-located in space, time, and frequency with the baseline network and is initialized to the same code-waveforms and routes. Multiple-access interference between the co-located wireless links leads to increased error rates in the received data frames, thus increases queue backlogs at both the source and intermediate network nodes. Data frames may be dropped completely if the maximum number of re-transmissions is reached by the transmitting nodes.

The objective in this scenario is to eliminate destructive interference and improve aggregate network throughput performance by jointly adapting code-waveforms and routes in the cognitive network. Particularly, the *decision* plane in the cognitive network nodes dynamically selects to switch to execution of the cross-layer optimization algorithm (as described in Fig. 4.2) upon the arrival of an external trigger. The instance when cross-layer optimization is active is referred to as coexist mode.

4.7.1.2 NET-Layer Interference

The second testbed scenario considers network congestion, created by intentionally flooding the queue of an intermediate network node in both cognitive and baseline networks with NET-layer interference. Resilient airborne network operation is achieved by autonomous route reconfiguration to bypass network disruption and successfully deliver information messages to the intended destination [9]. Random data frames, which mimic the frame format of cognitive and baseline data links, are generated but will not be correctly received and decoded. The random frames are injected in both networks at the same time. Cross-layer adaptation in the cognitive network is expected to balance traffic loads at the intermediate network nodes by jointly optimizing code-waveforms and selecting routes that maximize local utility values U_{ij} between transmitter i and receiver j. As a result, multimedia sessions in the cognitive network are expected to withstand NET-layer interference by selecting to reroute traffic around the heavily backlogged intermediate nodes. However, the same decision logic is not adopted by the baseline network nodes, therefore network throughput performance is expected to degrade significantly.

4.7.1.3 PHY-Layer Interference

Finally, the third testbed scenario considers disruption of baseline and cognitive network operation due to RF interference from either a mobile airborne or terrestrial node. Highly mobile UAV networks encounter unpredictable location-dependent interference [78] and should be capable of automatically adapting network parameters to maintain link quality. Particularly, a wideband RF interferer is introduced that transmits data frames modulated by the same (heavily correlated) code-waveform that is already utilized by other cognitive and baseline links in the testbed. An airborne RF interferer is employed during outdoor testing, while a terrestrial RF interferer is used for indoor tests. Based on simulation results for code-waveform optimization (presented in Section 3.5), cognitive network links are expected to withstand PHY-layer interference by jointly designing maximum-SINR code-waveforms and selecting routes that maximize network throughput. Depending on the power and location configuration of the RF interferer, baseline links become heavily backlogged due to destructive RF interference, thus baseline network throughput performance is expected to degrade notably.

4.7.2 Indoor Experiments

Indoor tests are conducted at the Department of Electrical Engineering at the State University of New York (SUNY) at Buffalo campus. The testbed is set up in a room of approximately 65 m^2 as depicted in Fig. 4.12. Nine nodes are used to build two co-located baseline and cognitive networks. Video traffic is carried over a single unicast session from one source network node S_1 to a destination node D_1. Baseline network traffic can be routed only through intermediate nodes I_1 and I_2 (i.e. 2-hops from the destination). Video

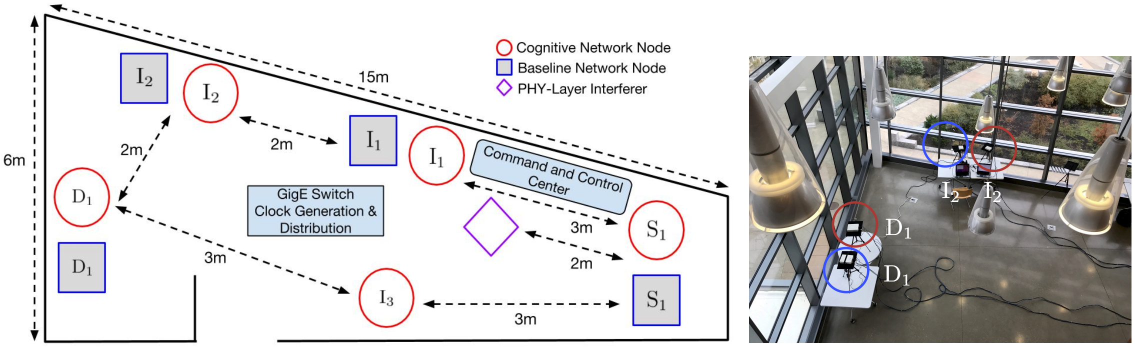

(a) Top view of the indoor testbed.

(b) Snapshot of a group of network nodes.

Figure 4.12: (a) Indoor testbed deployment at the Department of Electrical Engineering, State University of New York at Buffalo. (b) One group of intermediate (I_2) and destination (D_1) nodes from both baseline and cognitive network that are deployed in the testbed. ©2018 IEEE.

traffic in the cognitive network is offered two additional 1-hop routes to the destination either through intermediate node I_3 or intermediate node I_1. Consequently, the cognitive network is capable of routing video frames to the destination through multiple paths at the same time (e.g. destination D_1 can receive simultaneously from both nodes I_1 and I_3). A tenth node in the testbed plays the role of an RF interferer that is preconfigured to disrupt operation of the S_1–I_1 link.

4.7.2.1 Network Coexistence

Fig. 4.13 depicts locally calculated utilities for cognitive links S_1–I_1 and S_1–I_3 and the corresponding routing decisions at source node S_1 for the network coexistence scenario. Utility values U_{11} and U_{13} for the cognitive network are plotted over a total time duration of 140 s and are calculated based on feedback information from the intermediate nodes. More specifically, queuing and post-filtering SINR information are received at the source node through acknowledgment and feedback/control packets that are sent by the intermediate nodes at preconfigured time intervals of 3 s. It can be observed that if $U_{11} - U_{13} > 0$

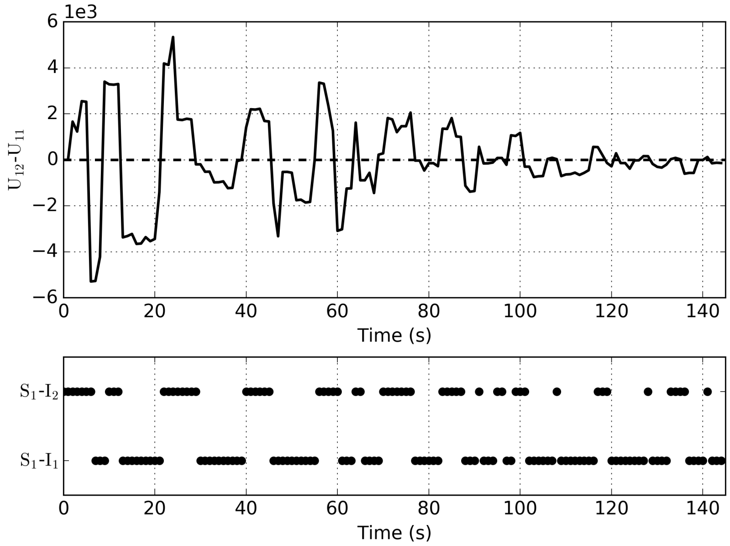

Figure 4.13: Difference of locally calculated utilities for cognitive links S_1–I_1 and S_1–I_3 (top) and corresponding routing decisions (bottom) at source node S_1 for the network coexistence scenario with coexist mode on. ©2018 IEEE.

intermediate node I_1 receives most of the traffic from source node S_1, otherwise node I_3 is selected as the next hop. Additionally, as data frames from the source node are successfully transmitted to the next hops, the magnitude of $U_{11} - U_{13}$ decreases over time.

4.7.2.2 NET-Layer Interference

Locally calculated utility values for cognitive links S_1–I_1 and S_1–I_3 and the corresponding routing decisions at source node S_1 for the second scenario of NET-layer interference are shown in Fig. 4.14. Intentional flooding of the queue of cognitive network node I_1 with 1000 frames is triggered by an external trigger at approximately $t = 25$ s. The proposed distributed adaptation algorithm implemented in the cognitive network rapidly identifies the sharp drop in utility calculated for the S_1–I_1 link and decides to reroute video traffic through intermediate node I_3. While the utility of link S_1–I_1 varies slightly from changes in post-filtering SINR due to code-waveform adaptation, the large backlog prevents U_{11} from becoming larger than U_{13} and I_1 remains inactive for the remainder of the trial.

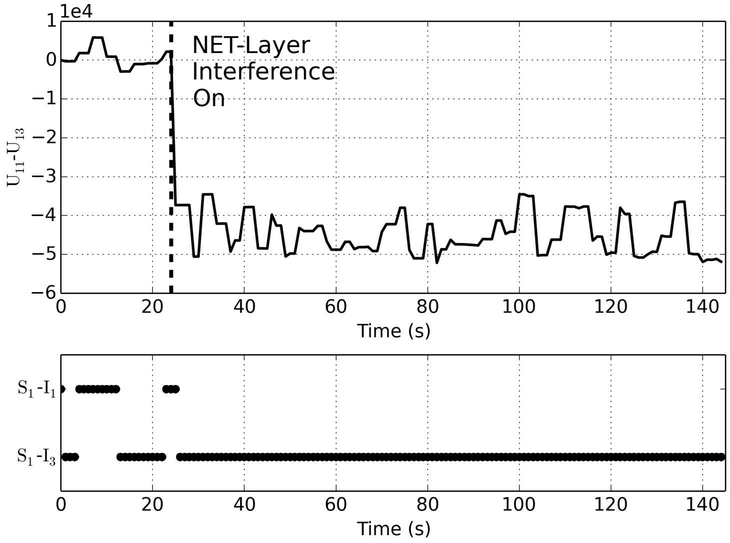

Figure 4.14: Difference of locally calculated utilities for cognitive links S_1–I_1 and S_1–I_3 (top) and corresponding routing decisions (bottom) at source node S_1 before and after NET-layer interference. ©2018 IEEE.

4.7.2.3 PHY-Layer Interference

Fig. 4.15 presents average post-filtering SINR performance for link S_1–I_1 in both cognitive and baseline networks and evaluates end-to-end network throughput performance for the third scenario of RF interference. Only for this set of experiments, traffic flows for both networks are carried over the same fixed route S_1–I_1–D_1. An RF wideband interferer is configured to transmit at the same code-waveform with co-located baseline and cognitive links S_1–I_1. The position of the interferer is depicted in Fig. 4.12a. Considering fixed routing and dynamic code-waveform adaptation at the cognitive network, the post-filtering SINR for the cognitive link S_1–I_1 is approximately 8 dB higher than the SINR of the baseline link. The RF interferer operation is activated by the user at $t = 50$ s. It can be observed that post-filtering SINR drops significantly for both links. Although the effect of RF interference is harsher for the cognitive link SINR, code-waveform adaptation protects cognitive end-to-end network throughput, which drops only by 15% compared to the baseline network throughput that drops by 90%. The notable degradation observed in the baseline network

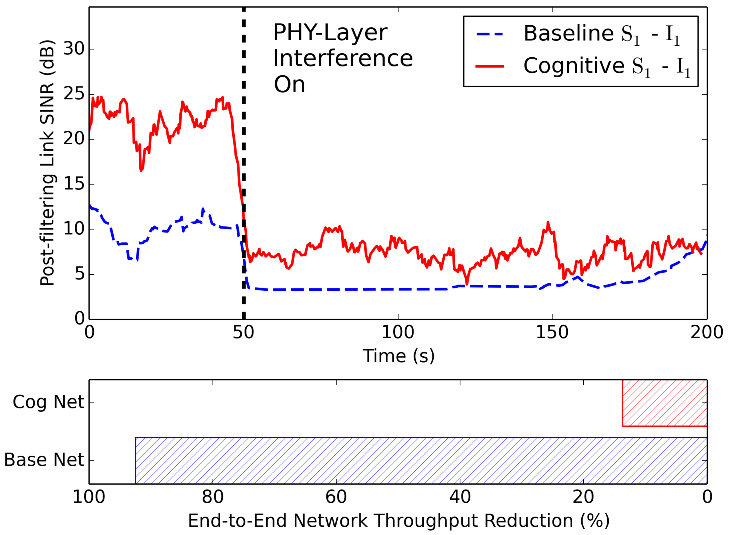

Figure 4.15: Average post-filtering SINR for the S_1–I_1 link in both cognitive and baseline networks (top) and end-to-end network throughput performance reduction (in %) for the PHY-layer interference scenario (bottom). ©2018 IEEE.

throughput performance after $t = 50\,\mathrm{s}$ is mainly due to the very low pre-detection SINR at the receiver of I_1.

4.7.3 Outdoor Experiments

Outdoor field tests are conducted at the Stockbridge Controllable Contested Environment (CCE) at Air Force Research Laboratory (AFRL) in Rome, NY. The testbed is set up inside a netted enclosure of approximately $10,000\,\mathrm{m}^3$ as depicted in Figs. 4.16a and 4.16b. Ten nodes are used to build two co-located baseline and cognitive networks and an eleventh node is mounted to an airborne vehicle platform. Digital audio and video traffic are carried over two unicast sessions from two network source nodes S_1 and S_2 to a common destination node $D_{1,2}$. Baseline network video traffic is routed through intermediate node I_1 while audio traffic is routed through intermediate node I_2. Video and audio traffic in the cognitive network is offered two additional 1-hop routes to the destination, through node I_2 and I_1, respectively. Consequently, both video and audio sessions in the cognitive network can

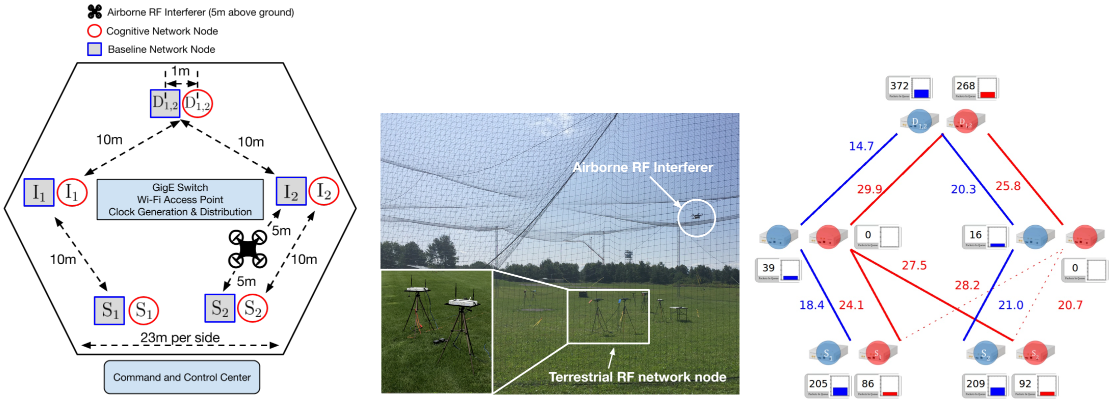

(a) Top view of the outdoor testbed.

(b) Airborne and terrestrial network nodes.

(c) Network visualization.

Figure 4.16: Outdoor testbed deployment dimensions (a) at the Stockbridge Controllable Contested Environment at Air Force Research Laboratory in Rome, NY (b). Network visualization in (c) depicts updates of post-filtering SINRs (in dB) in real time for active links. Queue information is displayed in the form of a bar-graph next to each network node. Dashed red lines illustrate feasible routes in the cognitive network. Solid blue and red lines depict selected routes in baseline and cognitive networks, respectively. ©2018 IEEE.

use the same intermediate network node(s) at the same time. Additionally, backlogged intermediate nodes can offload their data queues by transmitting data to the destination at the same time or even if they are not selected as the next hop by neither of the two source nodes (e.g. Fig. 4.16c). The eleventh node is mounted on an airborne vehicle platform, which is controlled remotely to hover at a height of approximately 5 m above ground. The position of the airborne node is depicted in Fig. 4.16a. The airborne node acts as a dedicated RF interferer that intends to disrupt communication of both terrestrial networks.

4.7.3.1 Network Coexistence

Fig. 4.17 depicts average aggregate queue size at intermediate nodes I_1 and I_2 and compares the network throughput performance of both cognitive and baseline networks for the scenario of network coexistence. Dashed lines depict aggregate queue size values over 80 s when

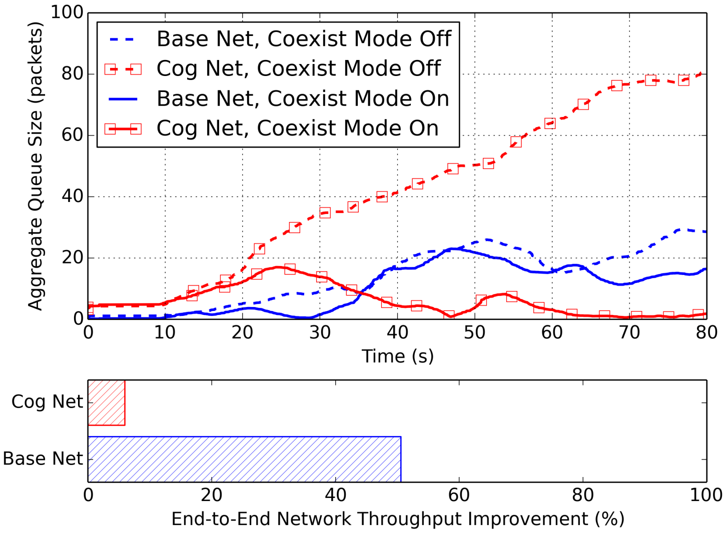

Figure 4.17: Average aggregate backlogged frames at the intermediate node queues in cognitive and baseline networks (top) and end-to-end network throughput (bottom) performance improvement (in %) for both networks before (coexist mode off) and after cross-layer adaptation (coexist mode on). ©2018 IEEE.

the two co-located networks utilize the same code-waveforms and routes (coexist mode off). Average backlog at the intermediate nodes increases due to increased multiple-access interference.

Solid lines demonstrate the effects of cross-layer adaptation (coexist mode on) and show reduced average aggregate queue size at the intermediate nodes of both networks. In line with expectations, when coexist mode is on, the queue size of the intermediate nodes in the cognitive network does not monotonically increase and remains low. Adaptation of waveform and routes favors the cognitive over the baseline network in terms of backlog and reduces RF interference to the baseline network. Consequently, the baseline network achieves 50% improvement in terms of network throughput. At the same time, the cognitive network throughput performance is improved by approximately 5%, therefore aggregate network throughput is increased by approximately 55%.

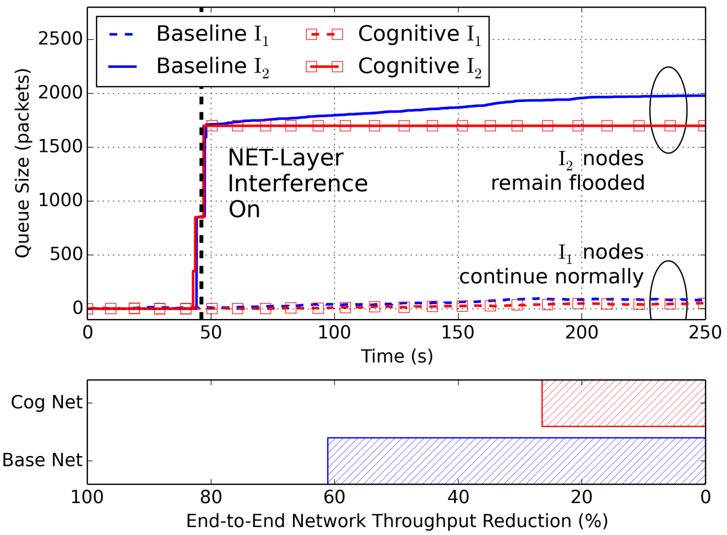

Figure 4.18: Queue size at intermediate network nodes (top) and end-to-end network throughput (bottom) performance reduction (in %) for both networks under NET-layer interference. ©2018 IEEE.

4.7.3.2 NET-Layer Interference

Instantaneous queue size at each intermediate network node and the end-to-end network throughput performance under NET-layer interference conditions for both networks is presented in Fig. 4.18. The queues of both cognitive and baseline nodes I_2 are intentionally flooded with 1600 randomly generated frames. Queue flooding is triggered by an external trigger at $t = 45\,\text{s}$. Since packets are rejected by the receiver ($D_{1,2}$), neither queue decreases and both cognitive and baseline nodes I_2 remain non-operational. The queue size of baseline node I_2 continues to increase as new video frames arrive from the baseline source node S_2. On the other hand, cognitive source node S_2 dynamically reroutes video traffic through cognitive node I_1, thus the queue size at cognitive node I_2 remains constant. End-to-end network throughput performance for the baseline network is notably degraded by 60% due to network congestion, whereas cognitive network throughput performance only drops by approximately 25%.

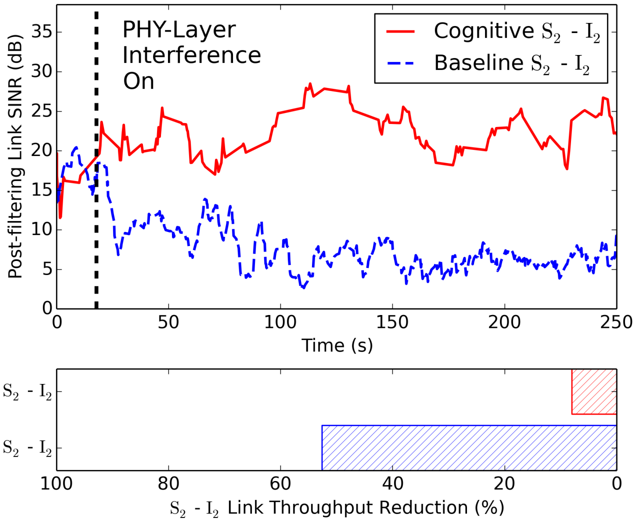

Figure 4.19: Average post-filtering SINR at the output of the maximum-SINR filter at receiver I_2 (top) and end-to-end network throughput (bottom) performance reduction (in %) for the PHY-layer interference scenario. ©2018 IEEE.

4.7.3.3 PHY-Layer Interference

Average post-filtering SINR and network throughput performance results for link S_2–I_2 in the presence of an airborne RF interferer is depicted in Fig. 4.19. An RF wideband interferer is preconfigured to operate at the same code-waveform with co-located baseline and cognitive terrestrial links S_2–I_2. The airborne interference source is activated remotely at $t = 20\,$s. The post-filtering SINR for the cognitive link S_2–I_2 remains constant after $t = 20\,$s, while the SINR of the baseline link drops by approximately 10 dB. Cross-layer waveform and routing adaptation at the cognitive network in the presence of the airborne interferer protects cognitive end-to-end network throughput which drops only by 5% compared to the baseline network throughput performance that drops by 50% .

Fig. 4.20 shows the total squared correlation (TSC) [118] between the optimized code-waveform $\mathbf{s}_{opt} \in \left\{\pm 1/\sqrt{L}\right\}^L$, $\|\mathbf{s}_{opt}\| = 1$ for cognitive link S_2–I_2 and the code-waveform of the airborne RF interferer $\mathbf{s}_I$. The code-waveform for link S_2–I_2 is optimized at preconfigured intervals of 3 s, while the code-waveform of the airborne interferer remains unchanged for

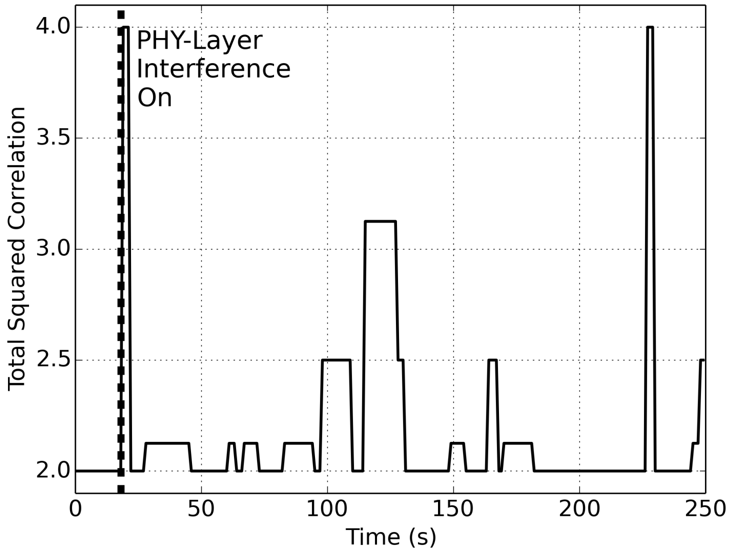

Figure 4.20: Total squared correlation between the optimized code-waveform for cognitive link S$_2$–I$_2$ and the code-waveform used by the airborne RF interferer. ©2018 IEEE.

the total duration of 250 s. Total squared correlation is defined as

$$\begin{aligned} \mathrm{TSC}\left(\mathbf{s}_{opt}, \mathbf{s}_I\right) &\triangleq \left|\mathbf{s}_{opt}^T \mathbf{s}_{opt}\right|^2 + \left|\mathbf{s}_{opt}^T \mathbf{s}_I\right|^2 + \left|\mathbf{s}_I^T \mathbf{s}_{opt}\right|^2 + \left|\mathbf{s}_I^T \mathbf{s}_I\right|^2 \\ &= 2 + 2\left|\mathbf{s}_{opt}^T \mathbf{s}_I\right|^2 . \end{aligned} \tag{4.13}$$

Consequently, if code-waveforms $\mathbf{s}_I$ and $\mathbf{s}_{opt}$ are orthogonal, $\mathbf{s}_{opt}^T \mathbf{s}_I = \mathbf{s}_I^T \mathbf{s}_{opt} = 0$ and $\mathrm{TSC}\left(\mathbf{s}_{opt}, \mathbf{s}_I\right) = 2$. Fig. 4.20 demonstrates that TSC is maximum at $t = 20$ s (i.e. airborne RF interferer is activated). Max-SINR optimization of the link S$_2$–I$_2$ results in code-waveforms with low TSC values. Since waveform optimization for link S$_2$–I$_2$ accounts for multiple-access interference from asynchronous transmissions in co-located wireless links, $\mathrm{TSC}\left(\mathbf{s}_{opt}, \mathbf{s}_I\right)$ is not minimized at all times.

4.8 Conclusion

This chapter presented a complete integrated software/hardware platform that enables the deployment of the first real-time software-defined radio testbed for prototyping spectrally efficient all-spectrum cognitive networks through cross-layer code-waveform and routing adaptation. Algorithmic developments that span the three lowest layers of the network protocol stack (PHY/MAC/NET) were presented and corresponding software, hardware, and baseband processing requirements analyzed. Distributed control mechanisms to handle real-time waveform and routing decisions at each cognitive network node were implemented. Subsequently, a programmable software/hardware radio reconfigurable framework that facilitates rapid implementation of the proposed algorithms in heterogeneous GPP-based SDR platforms was set up. The proposed framework is optimized to run on multi-core GPP architectures that equip both terrestrial and airborne platforms. Testbed operation challenges are addressed for the deployment of a hybrid ground-air testbed and evaluate all-spectrum cognitive networking in both indoor and outdoor environments. Finally, experimental results include post-filtering link SINR, queue size, utility measurements at the intermediate network nodes, and network-throughput performance comparison between baseline and cognitive networks that implement cognitive waveform and routing adaptation. Proof-of-concept results show that the proposed platform can be used to build cross-layer optimized all-spectrum networks that withstand interference at PHY and NET layers and maximize aggregate network throughput in underlay spectrum coexistence scenarios.

Chapter 5

Adaptive Receiver Design for Underwater Acoustic Communications

5.1 Introduction

In recent years, there has been active research interest in the area of underwater acoustic (UW-A) networking, which exhibits an abundance of compelling applications such as offshore exploration, tactical surveillance, pollution and marine ecology monitoring [119–121]. The underwater acoustic channel is highly dynamic and characterized by high and variable path loss, time-varying multipath, large frequency and time spreading, and limited bandwidth [13]. Underwater acoustic communication links are subject to ambient and site-specific noise from many sources. Ambient noise sources, found in most underwater environments, can come from natural or human activity including wind, seismic activity, and turbulence [122]. Site-specific noise of particular interest to this dissertation is impulsive noise encountered in warm coastal regions and primarily attributed to snapping shrimp. Snapping shrimp

---

Portions of this chapter are adapted from the author's published work in [3] (©2018 IEEE).

can be the dominant noise source across the entire frequency range of interest to acoustic communications in environments where wind noise is minimal [123].

Spread-spectrum signaling offers increased signal-to-interference-plus-noise ratio (SINR) per data symbol and robustness over the multipath UW-A channel [124]. Recent work in [125] demonstrated the SINR performance benefits of adaptive code-division channelization in a software-defined underwater acoustic testbed. Additionally, spread-spectrum communication schemes provide signals whose level can be kept below that of the noise, thus offering low-probability of detection/low-probability of intercept (LPD/LPI) capabilities [126]. For these reasons, work in this chapter will analyze spread-spectrum systems.

Although higher spreading code lengths may offer increased SINR per symbol in additive white Gaussian noise (AWGN) environments, the time-varying multipath delay spread and channel gain in the shallow UW-A channel can significantly affect SINR performance [127]. More specifically, long spreading codes may be suitable to mitigate intersymbol interference (ISI) due to long multipath spreads. However, static spreading code length allocation limits the achievable link data rate when channel characteristics change over time. At the same time, limited sample support due to UW-A channel variations may significantly affect receiver SINR performance due to poor estimates of adaptive max-SINR filters [53] at the receiver. The time-varying nature of the underwater acoustic channel typically requires the use of frequent channel re-training and tracking at the receiver, which increases the data overhead due to pilot signaling and thus reduces the overall system spectral efficiency. Therefore, blind (or semi-blind: employing very few pilots) is very attractive for communication in this challenging environment.

This chapter presents developments towards more aware and adaptive underwater communication systems. The short-data record performance of auxiliary-vector (AV) filtering [128] is leveraged to adaptively optimize spreading code lengths toward high-rate spread-spectrum underwater acoustic links. A semi-blind receiver based on L1-norm principal component analysis is developed for the impulsive noise environment in coastal waters caused by snapping shrimp.

5.2 System Model

The system model in this chapter considers K asynchronous multiplexed underwater acoustic communication users that transmit information symbols from a unit energy phase-shift keying (PSK) constellation $\mathcal{A}$. Specifically, the k-th transmitted signal is written as

$$x_k(t) = \sqrt{E_k} \sum_i b_k[i] s_k(t - iT) e^{j(2\pi f_c t + \phi_k)} \tag{5.1}$$

where $E_k > 0$ is the transmitted energy per symbol, ϕ_k the carrier phase, and f_c the carrier frequency. The i-th transmitted symbol $b_k[i] \in \mathcal{A}$ is modulated by a digital waveform $s_k(t)$ of duration T that is given by

$$s_k(t) = \sum_{l=0}^{L-1} s_k[l] g_{T_c}(t - lT_c) \tag{5.2}$$

where $\mathbf{s}_k \in \left\{ \pm 1/\sqrt{L} \right\}^L$ is a binary antipodal code of length L, and $g_{T_c}(\cdot)$ is a square-root raised cosine (SRRC) pulse with roll-off factor α and duration T_c, so that $T = LT_c$. The bandwidth of the k-th transmitted signal is $B = (1 + \alpha)/T_c$.

Assume that transmitted signals propagate over independent time-varying frequency-selective UW-A channels with M resolvable paths (assumed to be the same for all K signals), with $a_m(t)$ and $\tau_m(t)$ denoting the m-th path's time-varying amplitude coefficient and path delay, respectively. For mathematical tractability, assume that $\tau_m(t)$ can be approximated by a first-order polynomial $\tau_m(t) = \tau_m - \beta_m t$, where $\beta_m = u_m/c$, u_m is the radial velocity of the m-th path and c is the speed of sound in water. The received signal at the input of a common destination receiver is written as

$$r(t) = \sum_{k=0}^{K-1} \sum_{m=0}^{M-1} a_m(t) x_k(t(1+\beta_m) - \tau_m) + n(t) \tag{5.3}$$

where $n(t)$ is additive noise, assumed to be uncorrelated with the transmitted signals. After carrier downconversion, pulse-matched filtering, and sampling over the extended multipath symbol duration, the received signal is rewritten as

$$\mathbf{r}[i] = b_0[i]\mathbf{H}_0\mathbf{s}_0 + \sum_{k=1}^{K-1} b_k[i]\mathbf{H}_k\mathbf{s}_k + \mathbf{j} + \mathbf{n} \in \mathbb{C}^{L_M} \tag{5.4}$$

where $\mathbf{H}_k \in \mathbb{C}^{L_M \times L}$, $L_M = L + M - 1$ is a Toeplitz matrix that models multipath fading for the k-th user of interest and is assumed to be invariant over channel coherence time T_{coh}, $\mathbf{j} \in \mathbb{C}^{L_M}$ denotes the multipath-induced ISI, and $\mathbf{n} \in \mathbb{C}^{L_M}$ is additive colored Gaussian noise with covariance matrix $\mathbf{R}_\mathbf{n} \in \mathbb{C}^{L_M \times L_M}$.

5.3 Short-Data Record Adaptive Packetization

Underwater communication systems that adapt to changing channel conditions by varying parameters such as modulation, error-correction code rate, and transmit power have been proposed in [117, 129–133]. This chapter proposes to leverage the short-data record performance benefits of auxiliary-vector (AV) filtering [128] to adaptively optimize spreading code lengths toward high-rate spread-spectrum underwater acoustic links. This chapter begins with an evaluation of the bit error rate (BER) performance of adaptive max-SINR receivers [53] based on estimates of the minimum variance distortionless response (MVDR) and AV filters for data record sizes that correspond to the UW-A channel coherence time. Simulations over time-varying UW-A channels verify that the AV filter significantly outperforms the estimated MVDR filter for short sample support. Subsequently, considering that spreading rate selection is decoupled from channel stability, code length optimization such that link data rate is maximized under predefined BER constraints is proposed. The proposed adaptive packetization scheme outperforms static code length allocation, while short data record filtering enables the design of forward/data and feedback communication links that comply with channel coherence.

5.3.1 Ambient Noise Model

To begin, the problem formulation will consider only ambient noise. Ambient noise is present in nearly all underwater environments, even the deep sea. Site-specific noise will be added to the signal model later in this chapter. Ambient noise in the underwater acoustic channel is frequency-dependent and produced by sources such as turbulence, wave action, ship traffic, and thermal noise from random motion of water molecules [122]. The power spectral density (PSD) of ambient UW-A noise can be approximated as[1]

$$N_{\mathrm{AVG}}(f) = 50 - 18\log(f)\ \text{ dB re } \mu\text{Pa/Hz} \tag{5.5}$$

for frequency f in kHz [134]. As Fig. 5.1 shows, in the simulations presented in this chapter, white Gaussian noise is filtered to generate colored noise with a PSD as specified in (5.5).

5.4 Adaptive Maximum SINR Filtering

Information symbols of a particular user of interest are detected by processing the received signal $\mathbf{r}$ with a normalized linear filter $\mathbf{w}_0$. If $\mathbf{H}_0$ and $\mathbf{s}_0$ denote the multipath channel matrix and spreading code of the user of interest, respectively, the RAKE-matched filter

---

[1] The term re μPa denotes with reference to the intensity of a plane wave with RMS pressure of 1 μPa. Unless otherwise specified, this reference is considered to be at a distance of 1 m from the sound source.

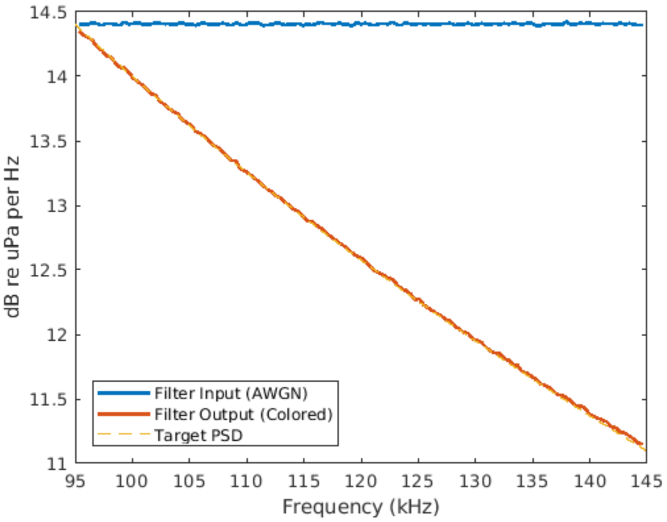

Figure 5.1: In simulation, white Gaussian noise is filtered to produce colored noise with a PSD typical of ambient UW-A noise.

(MF) is given by

$$\mathbf{w}_0^{\|\mathrm{MF}\|} = \frac{\mathbf{H}_0\mathbf{s}_0}{\|\mathbf{H}_0\mathbf{s}_0\|^2}. \tag{5.6}$$

The i-th received information symbol is then recovered by minimum distance detection $\hat{b}_0[i] = \arg\min_{b\in\mathcal{A}} \left|\mathbf{w}_0^H\mathbf{r}[i] - b\right|^2$.

5.4.1 MVDR Filtering

Assuming perfect knowledge of the input autocorrelation matrix, defined as $\mathbf{R} \triangleq \mathrm{E}\{\mathbf{r}[i]\mathbf{r}[i]^H\}$, the RAKE-type receiver that minimizes the output variance subject to the constraint that it remains distortionless in the effective direction $\mathbf{w}_0^{\|\mathrm{MF}\|}$ of the user of interest [135] (equivalent to the maximization of the output SINR) is given by

$$\mathbf{w}_0^{\|\mathrm{MVDR}\|} = \frac{\mathbf{R}^{-1}\mathbf{H}_0\mathbf{s}_0}{\mathbf{s}_0^T\mathbf{H}_0^H\mathbf{R}^{-1}\mathbf{H}_0\mathbf{s}_0}. \tag{5.7}$$

Algorithm 1 AV Filter Sequence Calculation

```
Input: $\mathbf{w}_0^{\|\text{MF}\|}$, $\widehat{\mathbf{R}}$
Output: $\{\mathbf{w}_{(0)}, \mathbf{w}_{(1)}, \mathbf{w}_{(2)}, \dots\}$
Initialization: $\mathbf{v} = \mathbf{w}_0^{\|\text{MF}\|}$, $\mathbf{w}_{(0)} = \frac{\mathbf{v}}{\|\mathbf{v}\|^2}$
for d = 1, 2, ... do
    $\mathbf{g}_d = \left(\mathbf{I} - \frac{\mathbf{v}\mathbf{v}^H}{\|\mathbf{v}\|^2}\right)\widehat{\mathbf{R}}\mathbf{w}_{(d-1)}$
    $\mu_d = \frac{\mathbf{g}_d^H \widehat{\mathbf{R}}\mathbf{w}_{(d-1)}}{\mathbf{g}_d^H \widehat{\mathbf{R}}\mathbf{g}_d}$
    $\mathbf{w}_{(d)} = \mathbf{w}_{(d-1)} - \mu_d \mathbf{g}_d$
end for
```

In practice, however, exact knowledge of the input autocorrelation matrix is not available, therefore MVDR filtering relies on a sample average estimate of the input autocorrelation matrix

$$\widehat{\mathbf{R}} = \frac{1}{N}\sum_{n=1}^{N} \mathbf{r}[n]\mathbf{r}^H[n] \tag{5.8}$$

where N is the number of signal snapshots (also called the data record or sample support) taken over a received signal duration that does not exceed channel coherence time T_{coh}. As a result, the sample-matrix-inversion (SMI) filter $\mathbf{w}_0^{\|\text{SMI}\|} = \widehat{\mathbf{R}}^{-1}\mathbf{H}_0\mathbf{s}_0/\mathbf{s}_0^T\mathbf{H}_0^H\widehat{\mathbf{R}}^{-1}\mathbf{H}_0\mathbf{s}_0$ offers an unbiased estimator of the MVDR filter. For $\widehat{\mathbf{R}}$ to be invertible with probability 1, $N \geq L_M$ data samples are required, otherwise $\widehat{\mathbf{R}}$ may be singular and $\mathbf{w}_0^{\|\text{SMI}\|}$ will not exist [136]. In fact, it is known that data records many times the size of L_M are needed to approach, reasonably well, the performance of the ideal MVDR filter. Regretfully, UW-A channel fluctuation rates significantly limit the available sample support for data rates and values of L_M that are typical in underwater acoustic communications.

5.4.2 Short Data Record AV Filtering

AV filters have shown to outperform batch-SMI and constraint-LMS implementations of the MVDR filter for limited sample support [53]. Algorithm 1 depicts the iterative generation

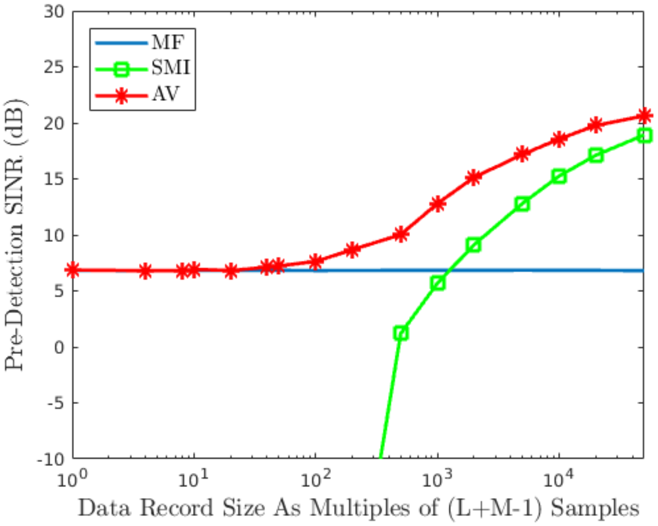

Figure 5.2: SINR performance of matched-filter, SMI, and AV linear filter receivers as a function of data record size. ©2018 IEEE.

of a sequence of AV filters $\{\mathbf{w}_{(0)}, \mathbf{w}_{(1)}, \mathbf{w}_{(2)}, \dots\}$ that converge to the SMI filter [128]. The selected AV filter

$$\mathbf{w}_0^{\|\mathrm{AV}\|} = \frac{\mathbf{w}_{(\hat{d})}}{\|\mathbf{H}_0\mathbf{s}_0\|^2} \tag{5.9}$$

maximizes the estimated J-divergence of the filter output conditional distributions [137] as follows

$$\hat{d} = \underset{d\,\in\,\{0,1,2,\dots\}}{\arg\max}\ \frac{4\mathrm{E}^2\left\{\left|\Re[\mathbf{w}_{(d)}^H\mathbf{r}]\right|\right\}}{\mathrm{Var}\left\{\left|\Re[\mathbf{w}_{(d)}^H\mathbf{r}]\right|\right\}} \tag{5.10}$$

where $\mathrm{Var}\{\cdot\}$ and $\mathrm{E}\{\cdot\}$ denote variance and expected value, respectively. Fig. 5.2 depicts the output (pre-detection) SINR performance of MF, SMI, and AV filters as a function of the number of signal snapshots used to calculate $\widehat{\mathbf{R}}$. For small sample support ($\mathrm{N} < 10^2$) the performance of the AV filter matches that of the MF. The AV filter significantly outperforms both MF and SMI filters for $10^2 \leq \mathrm{N} \leq 10^4$, while SMI filter performance is significantly degraded for $\mathrm{N} < 10^3$. As data record size grows beyond $\mathrm{N} > 10^5$ samples, the performance of the AV filter begins to converge to that of the SMI filter.

5.5 Adaptive Packetization

The adaptive system considers frame-based transmissions of N information symbols that are modulated with spreading codes of length L. The total duration of a data frame is $T_f = L \cdot N \cdot T_c$ and the link data rate for the user of interest, in symbols-per-second, is defined as $R(L) \triangleq 1/(LT_c)$.

5.5.1 Code Length Adaptation

Adaptive selection of spreading code length L to optimize link data rate over the time-varying UW-A channel presents trade-offs between reliability and throughput. Given that for fixed frame duration, channel stability is decoupled from the selection of spreading rate, longer code lengths may offer increased resilience to interference and multipath channel effects. On the other hand, shorter code lengths increase the link data rate at the expense of increased susceptibility to bit errors. The objective is to adaptively optimize the code length L of the user of interest to maximize link data rate, while satisfying a pre-defined BER constraint

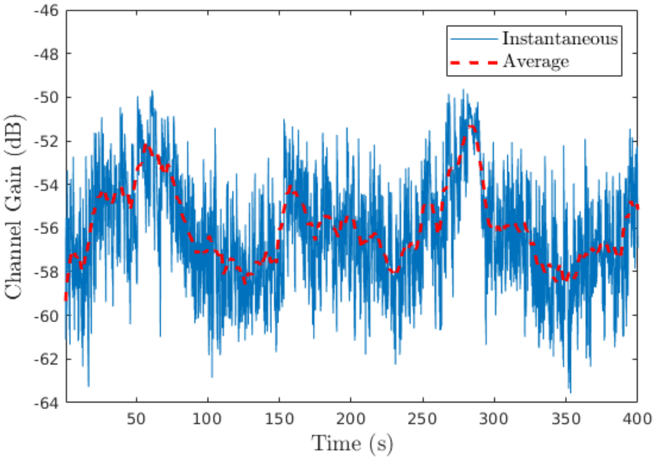

Figure 5.3: Instantaneous and average (over a 10 s window) channel gain of the simulated underwater channel versus time. ©2018 IEEE.

$$\begin{aligned} \underset{L}{\text{maximize}} \quad & R(L) \\ \text{subject to} \quad & BER(L) \leq BER_{max} \\ & L_{min} \leq L \leq L_{max}, \quad L \in \mathbb{Z} \end{aligned} \tag{5.11}$$

where L_{min} and L_{max} are the minimum and maximum allowable code lengths, respectively. Upon reception of a data frame, the receiver solves (5.11) and communicates the optimized code length to the transmitter over a wireless UW-A feedback link.

5.5.2 Feedback Considerations

Long propagation delays in the UW-A channel affect the implementation of wireless feedback links for adaptive underwater communications. For effective code length adaptation, the round-trip time (RTT) of a data frame and its associated feedback frame should not exceed the channel coherence time. Considering negligible processing time, the round-trip time is expressed (with obvious notation) as RTT $= 2T_{prop} + T_f + T_{feedback}$. Since only a few bits are required to represent the optimized code length, consider that $T_{feedback}$ is negligible as well. As a result, for a transmitter-receiver distance of d meters and $c \approx 1500\,\text{m/s}$, the speed of sound in water, the duration of the data frame T_f must satisfy

$$T_f \leq T_{coh} - \frac{2d}{c}. \tag{5.12}$$

In light of the constraint in (5.12), the AV linear filter is deployed at the receiver, to benefit from its superior performance over short data records (i.e. short data frames).

5.6 Performance Evaluation

The performance of the proposed adaptive packetization scheme is evaluated in terms of data rate, under a pre-defined BER constraint. The performance of the adaptive scheme is also compared to a fixed code length scheme.

5.6.1 Simulation Setup

Simulations in this section consider a single transmitter-receiver pair for which perfect synchronization, Doppler compensation, and channel state information availability at the receiver is assumed. Simulations are carried out using time-varying channel realizations, generated by an UW-A channel simulator [138] that follows the statistical model in [139]. The transmitter and receiver are separated by 600 m in a 10 m deep channel, with the transmitter and receiver fixed at 6 m and 8 m below the water surface, respectively. From this geometry, propagation paths and delays are calculated. Variations in the channel are introduced to account for effects such as surface scattering while ambient noise is generated according to (5.5).

Building upon past ultrasonic wideband underwater communication experiments [132, 133], the transmitted signals occupy the entire available bandwidth from 95 kHz to 145 kHz. Prior work has discussed coherence times in the range of 100 ms $-$ 2.0 s [13, 140]. For the purpose of simulation, the coherence time of small-scale channel variations is set to 1.0 s. The channel gain for the simulated UW-A channel is plotted in Fig. 5.3 as a function of time. While variations of the time-averaged (over a 10 s window) channel are on the order of several dB, the instantaneous channel gain changes over a range of $\sim$ 14 dB, thus offering an opportunity for increased throughput performance via code length adaptation. Frames of binary phase-shift keying (BPSK) symbols are considered with frame duration limited to $T_f = 200$ ms based on (5.12). As the selected frame duration is smaller than the channel coherence time, channel fading coefficients are assumed to remain constant for the entire duration of the frame.

5.6.2 Adaptive Code Length Performance

Fig. 5.4 depicts the BER performance of the AV filter for different code lengths as a function of the transmitted symbol energy E_0 in dB re μPa. As expected, longer code lengths produce lower bit error rates. Since frame duration is fixed at $T_f = 200\,\text{ms}$, the SMI filter has insufficient sample support, thus increasing transmit energy does not offer any performance gain. Frames using longer code lengths will contain fewer information symbols and provide smaller sample support. As a result, the SMI filter produces the highest BER for $L = 32$.

Subsequently, the short data record performance benefits of AV filtering are leveraged. Transmit symbol energy is fixed and a target BER of 10^{-4} is set which, for the noise and channel conditions considered here, will be satisfied with a pre-detection SINR of 10 dB. Fig. 5.5 shows that longer code lengths will achieve the target SINR for lower channel gains. Based on the relation between SINR and channel gain in Fig. 5.5, for each received frame the channel gain is estimated and the shortest code length selected that satisfies the target SINR of 10 dB, plus a small margin (1.5 dB) to account for uncertainty. A discrete set of code lengths $L \in \{8, 9, 10, 11, 12, 16, 20, 24, 28, 32\}$ is considered. Code length updates are applied to the transmitter after a simulated delay to account for the propagation time of the feedback frame. Data rate and pre-detection SINR performance for the channel instance in Fig. 5.3 is shown in Fig. 5.6. High data rates in the periods of favorable channel gain from 50 s to 70 s and from 250 s to 300 s can be observed. Simulations of $4,000$ frames are run and results averaged over 12 independent channel realizations. For comparison, consider the non-adaptive scheme of a static code length ($L = 24$). Although the average BER of both the static and adaptive schemes satisfy (within 10%) the target BER of 10^{-4}, the static

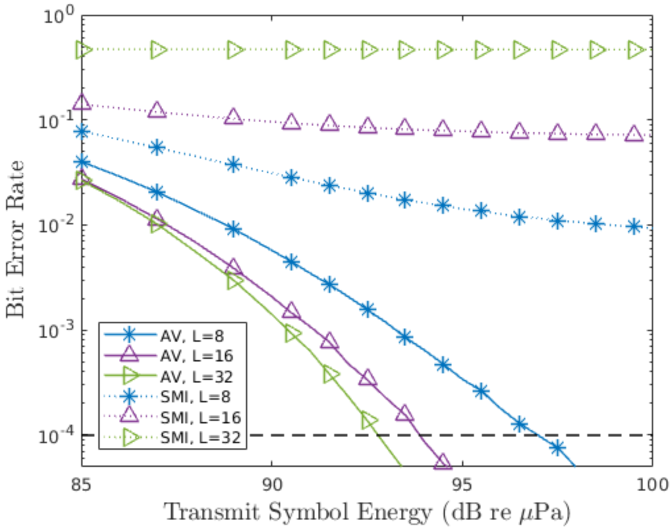

Figure 5.4: BER performance of different code lengths for AV and SMI filtering as a function of transmitted symbol energy. The dashed line denotes the target BER of 10^{-4}. ©2018 IEEE.

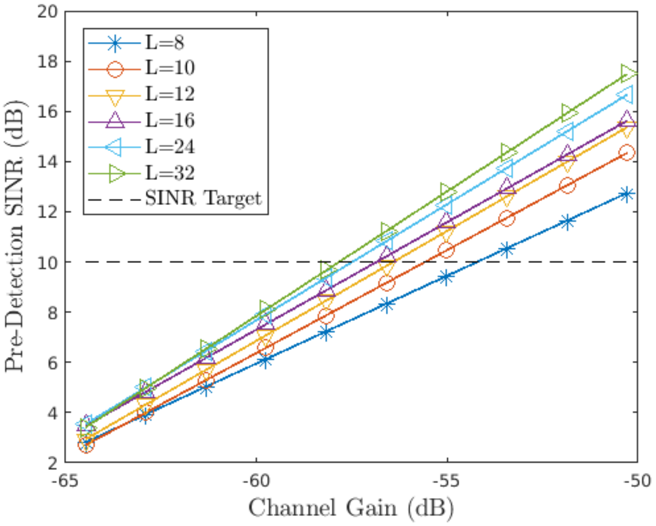

Figure 5.5: Average pre-detection SINR for AV filtering and different code lengths as a function of channel gain. The dashed line denotes the pre-detection SINR of 10 dB required to achieve the target BER of 10^{-4}. ©2018 IEEE.

scheme achieves an average throughput of 1.54 kbps and the adaptive scheme an average of 2.01 kbps, an improvement of 30.5%.

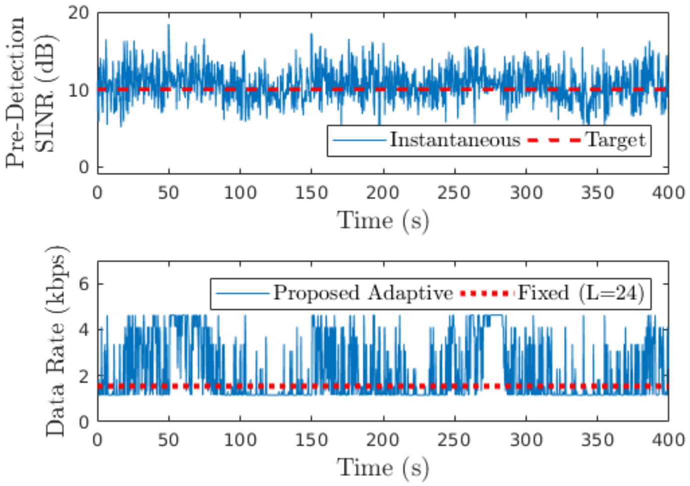

Figure 5.6: Instantaneous pre-detection SINR compared to the target SINR (top). Data rate for the adaptive and static ($L = 24$) code length communication schemes (bottom). ©2018 IEEE.

5.7 Semi-Blind Signal Recovery

Of particular interest to this chapter is the impulsive noise encountered in warm coastal regions and primarily attributed to snapping shrimp. The rapid closure of a snapper claw creates a high velocity jet of water which produces cavitation bubbles and can stun or kill prey [141]. The collapse of the bubble produces a sharp, wideband snapping sound with a peak-to-peak amplitude as high as 190 dB re μPa at 1m [142]. Shrimp noise extends well above 200 kHz [143] and can be the dominant noise source across the entire frequency range of interest to acoustic communications in environments where wind noise is minimal [123]. In warm waters, shrimp are found in sufficient density that underwater acoustic receivers encounter a permanent background crackling noise consisting of impulsive snaps [144]. As a result, communication receiver designs based on the Gaussian noise assumption may yield poor performance even at moderate signal-to-noise ratios.

The remainder of this chapter investigates blind signal recovery based on Principal-Component Analysis (PCA) and proposes a new receiver design based on L1-norm PCA

(L1-PCA). Most of the prior work on channel estimation in underwater acoustic channels uses PCA to minimize the L2-norm of the channel prediction error (i.e. the difference between the observed signal and the adaptive filter output). However, due to its L2-norm formulation, standard PCA is highly responsive to corrupted, highly deviating, irregular measurements, even when they appear in vanishingly small numbers. On the contrary, L1-PCA has exhibited significant robustness against heavy-tail, impulsive data corruptions [145]. A promising fit to recorded data has been obtained by modeling the noise with a symmetric α-stable (SαS) distribution [146–148]. Related work proposes a nonparametric sign correlation detector for operation in a shrimp noise dominated environment [144]. In [149] a sparse channel estimator-based decision feedback equalizer robust to impulsive noise is proposed. Log-likelihood ratio and maximum likelihood detectors considering an SαS noise process with memory are derived and simulated in [150, 151].

This chapter studies the performance benefits of L1-norm PCA for signal recovery in underwater environments. The sections that follow discuss generation of impulsive underwater noise and present simulations of the receiver in realistic underwater channels. Performance is compared to pilot-based and blind receiver designs in terms of bit error rate (BER).

5.7.1 Impulsive Noise Model

In calm weather conditions, noise from snapping shrimp dominates at frequencies above 2 kHz [123] and is present across two decades [143], covering nearly the entire bandwidth of acoustic transducers commonly used for underwater acoustic communications [133]. In warm coastal waters, measured underwater noise contains a number of high amplitude outliers and the noise process is well modeled by the SαS distribution. The distribution is characterized by two parameters: scale parameter γ and characteristic exponent $\alpha \in (0, 2]$

which controls the heaviness of the tails[2]. Increasing α will make the tails lighter, converging to the zero-mean Gaussian distribution for $\alpha = 2$ [152]. With the exception of a few special cases (such as the Gaussian), the probability density function of an SαS does not have a closed form expression. The characteristic function provides a convenient closed form expression

$$\phi(\theta) = \exp\left(-\gamma^{\alpha} \left|\theta\right|^{\alpha}\right) \tag{5.13}$$

from which the PDF can be calculated.

The parameters can be fit to a set of noise measurements. Values of α in the range of $1.55 - 1.9$ and γ in the range of $5 \cdot 10^4 - 1.5 \cdot 10^5\ \mu Pa$ have been reported in the literature [144, 147]. Using a package in MATLAB [153] random numbers from this distribution are drawn to create a noise vector. An example is shown in Fig. 5.7 for $\alpha = 1.82$ and $\gamma = 1.5 \cdot 10^5\ \mu Pa$ which closely matches experimental data reported in [144, Fig. 2b].

It is worthwhile to note that while the SαS distribution described here models the amplitude probability distribution quite well, measurements of shrimp noise exhibit clustering of outliers in intermittent bursts and additional techniques incorporating memory have been developed to model this behavior [148]. Since the simulations presented in this chapter are mainly concerned with average bit error rate over many independent realizations, the memoryless SαS is suitable model for this work.

---

[2] Within the literature on stable distributions there have evolved several inconsistent notations for the parameters of the distribution. This chapter chooses to follow the parameters in [152]. Other works in this area (e.g. [144]) use a different parameterization. When researching other works, the reader is encouraged to take note of how parameters are defined with respect to the characteristic function to avoid potential confusion.

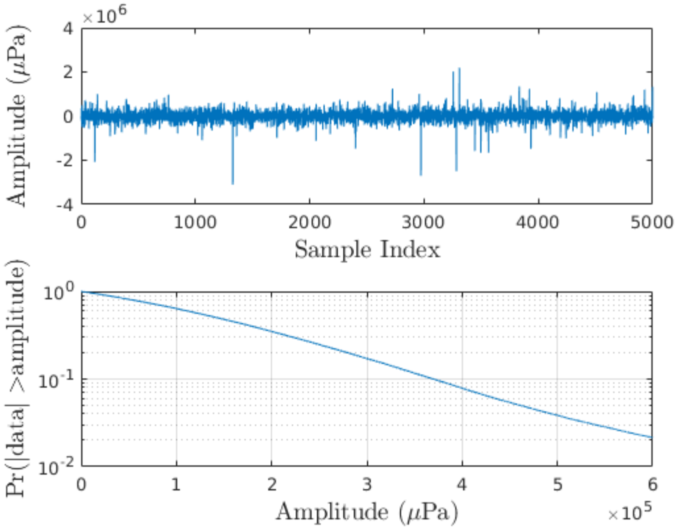

Figure 5.7: Samples generated from SαS distribution modeling snapping shrimp noise (top) and their amplitude probability density (bottom). Parameters $\alpha = 1.82$ and $\gamma = 1.5 \cdot 10^5 \mu Pa$ are used.

5.8 Adaptive Filtering

The received signal vector in (5.4) is processed by a linear filter $\mathbf{w}_0$ for the user of interest and information symbols recovered by minimum distance detection $\hat{b}_0[i] = \arg\min_{b \in \mathcal{A}} \left| \mathbf{w}_0^H \mathbf{r}[i] - b \right|^2$. A common filter choice which is simple but suboptimal when noise or interference is non-white is the matched-filter (MF)

$$\mathbf{w}_0^{\mathrm{MF}} = \mathbf{S}_0 \mathbf{h}_0. \tag{5.14}$$

where $\mathbf{S}_0 \in \left\{ \pm 1/\sqrt{L} \right\}^{L_M \times M}$ is a Toeplitz matrix that models the multipath-processed spreading-code matrix for the user-of-interest. In practice, $\mathbf{h}_0$ must be estimated from a number of pilot symbols N_{pilot} known a priori at the receiver

$$\widehat{\mathbf{h}_0} = (\mathbf{S}_0^T \mathbf{S}_0)^{-1} \mathbf{S}_0^T \frac{1}{N_{\text{pilot}}} \sum_{i=1}^{N_{\text{pilot}}} \mathbf{r}[i] b_0^*[i]. \tag{5.15}$$

Therefore, performance of the matched filter is dependent on the number of pilot symbols.

5.8.1 L2-Norm PCA Receivers

Received signal vectors are gathered into a received signal matrix $\mathbf{Y} = [\mathbf{r}[0], \mathbf{r}[1], \ldots, \mathbf{r}[N-1]] \in \mathbb{C}^{L_M \times N}$ prior to L1 and L2-PCA. Mathematically, L2-PCA finds the size-D ($1 \leq D \leq \text{rank}(\mathbf{Y})$) orthonormal basis that solves

$$\mathbf{Q}_{\text{opt}}^{\text{L2}} = \underset{\mathbf{Q} \in \mathbb{C}^{L_M \times D};\, \mathbf{Q}^H\mathbf{Q} = \mathbf{I}_D}{\text{argmax}} ||\mathbf{Q}^H \mathbf{Y}||_2 \tag{5.16}$$

where, for a matrix $\mathbf{A} \in \mathbb{C}^{M \times N}$, the L2-norm is $||\mathbf{A}||_2 \triangleq \sqrt{\sum_{m=1}^{M} \sum_{n=1}^{N} |a_{m,n}|^2}$ and $\mathbf{I}_D$ is the size-D identity matrix [145]. In this chapter, the desired output of the L2-PCA is a filter vector ($D = 1$), therefore (5.16) can be written

$$\mathbf{q}_{\text{opt}}^{\text{L2}} = \underset{\mathbf{q} \in \mathbb{C}^{L_M \times 1};\, \mathbf{q}^H\mathbf{q} = 1}{\text{argmax}} ||\mathbf{q}^H \mathbf{Y}||_2. \tag{5.17}$$

The solution to (5.17) can be formed by the dominant singular vector of $\mathbf{Y}$, obtained through singular value decomposition (SVD) of $\mathbf{Y}$ with quadratic complexity in N [154]. The SVD of $\mathbf{Y}$ is of the form

$$\mathbf{Y} = \mathbf{U}\mathbf{\Sigma}\mathbf{V}^H \tag{5.18}$$

where $\mathbf{U} \in \mathbb{C}^{(L_M \times L_M)}$ and $\mathbf{V} \in \mathbb{C}^{(N \times N)}$ are unitary matrices and $\mathbf{\Sigma} \in \mathbb{R}^{(L_M \times N)}$ contains the singular values of $\mathbf{Y}$ on the diagonal. The L2-PCA filter is constructed with $\mathbf{u} = [\mathbf{U}]_{:,1}$, the column of the matrix $\mathbf{U}$ corresponding to the largest singular value. A filter constructed from $\mathbf{u}$ will not preserve phase information, so the L2-PCA filter requires a few (as little as one) pilot symbols to correct the phase ambiguity. The phase is estimated as

$$\widehat{\phi}_0 = \angle\left(\mathbf{u}^H \mathbf{r}[0] b_0[0]\right) \tag{5.19}$$

and the L2 filter calculated as

$$\mathbf{w}_0^{\mathrm{L2}} = \exp{(j\widehat{\phi}_0)}\mathbf{u}. \tag{5.20}$$

5.8.2 L1-Norm PCA Receiver

A disadvantage of L2-PCA is its sensitivity to outliers in the received signal matrix. Received signals corrupted by impulsive shrimp noise provide just this type of outliers and can limit the performance of the L2-PCA receiver. A promising approach with increased robustness against outliers is L1-norm PCA [155, 156]. A straightforward modification of (5.17) gives the L1-PCA formulation

$$\mathbf{q}_{\mathrm{opt}}^{\mathrm{L1}} = \underset{\mathbf{q}\in\mathbb{C}^{L_M\times 1};\ \mathbf{q}^H\mathbf{q}=1}{\operatorname{argmax}} ||\mathbf{q}^H\mathbf{Y}||_1. \tag{5.21}$$

where for a matrix $\mathbf{A} \in \mathbb{C}^{M\times N}$, the L1-norm is $||\mathbf{A}||_1 \triangleq \sum_{m=1}^{M}\sum_{n=1}^{N}|a_{m,n}|$. Conceptually, by removing the squaring operation each data point is weighted less heavily and robustness to outliers is increased. The basis vector $\mathbf{q}_{\mathrm{opt}}^{\mathrm{L1}}$ is generated following the methods in [145]. As above, phase ambiguity is resolved through estimation

$$\widehat{\phi}_0 = \angle\left(\mathbf{q}_{\mathrm{opt}}^{\mathrm{L1},H}\mathbf{r}[i]b_0[i]\right) \tag{5.22}$$

and correction

$$\mathbf{w}_0^{\mathrm{L1}} = \exp{(j\widehat{\phi}_0)}\mathbf{q}_{\mathrm{opt}}^{\mathrm{L1}}. \tag{5.23}$$

5.9 Performance Evaluation

This section presents performance results obtained from simulation with realistic noise and channel conditions.

5.9.1 Simulation Setup

As in Section 5.6, simulations were carried out using time-varying channel realizations generated by an underwater acoustic channel simulator [138] following the statistical model described in [139]. Transmission occurs in a shallow water channel 20 m deep with transmitter and receiver 8 m below the surface and separated by 500 m. Propagation path gains and delays are calculated from this geometry with variations to account for effects such as transmitter and receiver drift. It is assumed that, upon reflection with the surface, each path is split into a small number (5) of intra-paths.

Ambient and snapping shrimp noise is added as described in Sections 5.3.1 and 5.7.1, respectively. Following parameters used in past ultrasonic wideband underwater communication experiments [132, 133] a bandwidth of 97.6 kHz at a center frequency of 100 kHz is used for simulation. The coherence time of the small-scale variations of the channel is assumed to be 100 ms, which is reasonable for most underwater channels [13].

Though the channel at a given time instance is modeled with a filter with 100 taps (corresponding to $\Delta f = 240Hz$), the receiver models the channel with $M = 14$ resolvable paths. The channel is considered to be quasi-static: channel coefficients are assumed to remain constant within the duration of a frame. Each frame is comprised of 500 binary-phase shift keying (BPSK) symbols, modulated by spreading codes of length $L = 29$. In this work, perfect frame detection and symbol timing synchronization are assumed to direct focus to a comparison between receivers in terms of their ability to equalize the channel and recover symbols.

5.9.2 L1/L2 Comparison

Fig. 5.8 depicts the BER performance of the L1, L2-PCA, and a pilot-based receiver with pilot symbols allocated for 25% of the transmitted frame. For a target BER, the

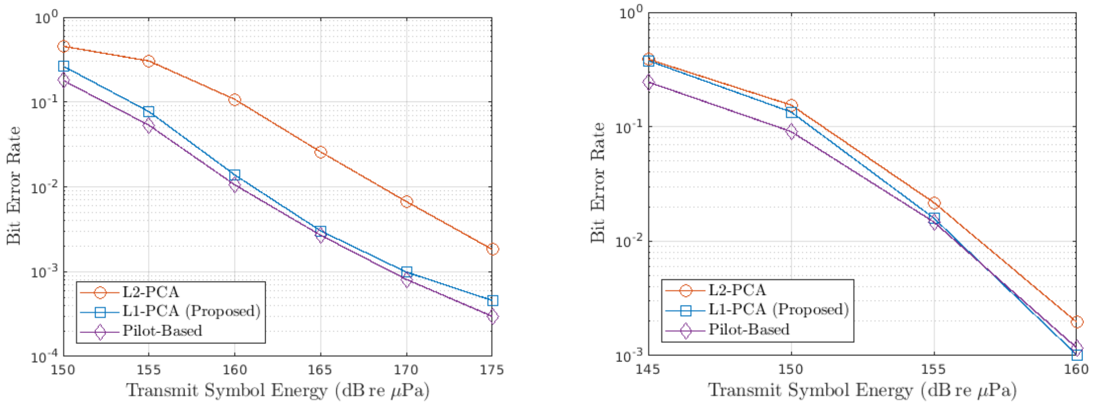

(a) BER performance versus transmitted symbol energy for SαS-modeled impulsive noise with $\alpha = 1.8$ and $\gamma = 1.5 \cdot 10^5$ μPa.

(b) BER performance versus transmitted symbol energy for SαS-modeled impulsive noise with $\alpha = 2.0$ (perfectly Gaussian) and $\gamma = 1.5 \cdot 10^5$ μPa.

Figure 5.8: Performance evaluation of the proposed L1-PCA receiver design in simulated shallow underwater acoustic channels and ambient impulsive noise conditions.

performance of the L1-PCA receiver in Fig. 5.8a falls within approximately 0.5 dB with respect to the pilot-based receiver, while the L2-PCA receiver requires an additional 10 dB of transmit symbol energy to achieve the same performance. For conceptual comparison, Fig. 5.8b depicts the BER performance for the least possible extreme case of impulsive noise conditions. At $\alpha = 2$ the noise samples follow a Gaussian distribution and there is less of a performance gap between L1-PCA and L2-PCA.

Results in Fig. 5.8 imply that when the processed data are not heavily corrupted, the solutions of L1-PCA and L2-PCA describe a nearly identical subspace. This is shown explicitly in Fig. 5.9 which plots the additional transmit symbol energy required for L1 and L2-PCA to match the performance of the pilot-based receiver at a target BER of $5 \cdot 10^{-3}$ as a function of the α parameter. A large performance difference can be observed over much of the common range of $\alpha \in [1.50 \ - \ 1.9]$. At $\alpha = 2$ the L1-PCA receiver still offers slightly superior BER performance, mainly due to the few outliers in the colored Gaussian characteristics of the underwater acoustic noise sources.

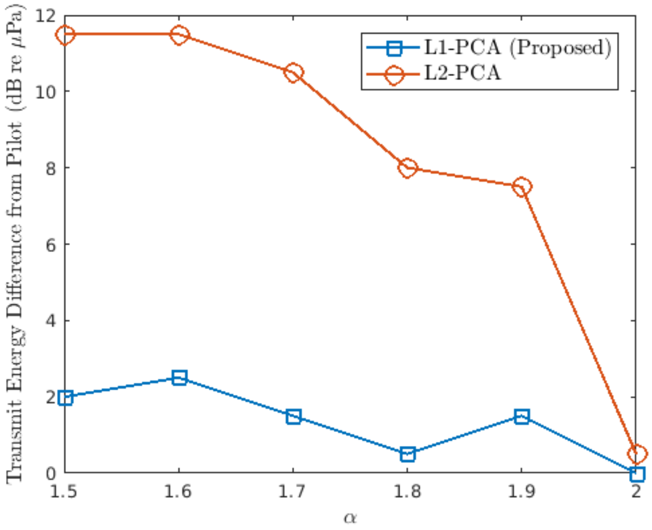

Figure 5.9: Additional transmit symbol energy required for L1 and L2-PCA to match the performance of the pilot-based receiver at a target BER of $5 \cdot 10^{-3}$ as a function of the α parameter.

5.10 Conclusion

This chapter discusses the unique challenges of underwater acoustic communications, particularly dynamic channels and impulsive noise. Adaptive max-SINR filters are evaluated in simulated UW-A channel and noise conditions and AV filtering is shown to outperform SMI and MF. An adaptive spreading code length feedback system is proposed using the AV filter to limit frame duration such that the round trip time of data packets and associated feedback does not exceed the channel coherence time. Simulation results verify the system improves throughput compared to a static code length scheme while maintaining the same bit error rate.

A receiver based on the L1-norm principal component analysis of the received signal is proposed for operation in channels dominated by shrimp noise. The performance of the semi-blind (requiring one bit for phase correction) L1-PCA receiver greatly outperforms a semi-blind L2-PCA receiver and nearly matches that of a pilot-based receiver. Results verify this holds true across the range of shrimp noise parameters reported in the literature, and even shows a slight performance increase in colored Gaussian noise. For reference, the simulation framework has been publicly released and is available online [157].

Chapter 6

Cognitive Radio for Space Communications

6.1 Introduction

Next generation space communication systems, capable of more efficient and robust communications, hold great promise to solve existing challenges with wireless communications in the space domain. Spacecraft built for scientific and human exploration are being outfitted with more numerous and increasingly complex instruments which require higher bandwidth. In the commercial sector, satellite-based services for telecommunications face additional demands for service reliability and data rate while often sharing spectrum resources with terrestrial networks and a growing number of satellite services, sometimes in different orbits. Millimeter wave frequencies, starting at 30 GHz, are the subjects of increased attention to leverage greater spectrum availability and achieve higher data rates [158, 159]. However, this attention is reflected in terrestrial communications [160] requiring new approaches to enable coexistence between emerging systems. Furthermore, space-Earth communications at these high frequencies suffer increased impairments and susceptibility to atmospheric effects, such as rain fading and gaseous absorption, and require advanced techniques to maintain both reliability and efficiency [17]. Building on increased capabilities of small satellite platforms [161], systems have been proposed using constellations [162] or clusters [163] of many satellites for telecommunications or science missions. As the number of spacecraft in Earth orbit and throughout the solar system increases, individual management of point-to-point or single-hop relay connections becomes unsustainable requiring the development of advanced in-space networking and system management tools [164].

6.1.1 Unique Aspects of Cognitive Radio for Space

Despite voluminous work in cognitive radio for terrestrial applications, it is only recently that serious attention has been given to introduce cognitive radio into space communications. Doing so may require only slight modification of techniques successfully used in terrestrial communications or may demand entirely new approaches, designed specifically to deal with the unique challenges of the space environment. There are several characteristics which make the space environment different and in some cases more challenging for cognitive radio than the terrestrial domain [165, 166]:

- Power and computational resources available on spaceborne platforms are limited compared to terrestrial base stations which are often integrated into an electrical grid.

- Few opportunities exist to maintain or upgrade systems once deployed. In many cases, the life cycle of large spacecraft can be years or even decades. Robust hardware and software is required with design typically beginning years prior to launch.

- Owing to the distances involved, space communication is characterized by large latency which makes the use of feedback channels to dynamically update parameters increasingly impractical at greater distance.

- The area served by a typical communications satellite is much larger than the area covered by a base station in terrestrial cellular networks and contains more potential sources of radio interference.

- Interference between satellite and terrestrial systems is location and elevation angle dependent. Transmissions at low elevation angles tend to cause more interference to and receive more interference from terrestrial systems. As a result, earth stations in high latitudes communicating with satellites orbiting the equator (a favorable spot for many communication satellites) suffer more interference.

- Comparatively weak signal levels make spectrum sensing more difficult than in terrestrial systems. Antennas used for space communication often have high directivity which can be useful to isolate interference between different systems. However, this makes sensing and analyzing another system's transmissions more difficult than the case of omnidirectional transmissions common in terrestrial cognitive radio.

- Some satellite allocations separate uplink (to space) and downlink (to Earth) services into separate bands. It is reasonable to assume that within these bands all traffic is unidirectional. Furthermore, in Earth observation and scientific satellites the balance between uplink and downlink traffic is highly asymmetrical with the majority of data produced on the spacecraft destined for Earth.

6.1.2 Chapter Organization

This chapter aims to present a comprehensive overview of state-of-the-art research and recent advancements in the last five years in cognitive radio for space communications. Techniques for dynamic spectrum access as well as physical-layer link management and network-level decision making are discussed. Furthermore, all sectors of space communications are considered: science missions, communication satellites, and applications beyond Earth orbit. This chapter is organized as follows. After a review of space communications in Section 6.2, space communication scenarios suitable for the application of cognitive radio are discussed in Section 6.3. Specific techniques for the realization of cognitive radio will be discussed with

Section 6.4 discussing spectrum access, Section 6.5 describing physical layer optimization techniques, and Section 6.6 detailing techniques at the network layer. In conclusion, Section 6.7 will present needs for advancement of the technology and promising areas of future study.

6.2 Overview of Space Communication

6.2.1 Space Transceiver Environments

Traditionally, the preferred location of communication satellites is in geostationary equatorial orbit (GEO). A satellite in GEO is located directly above the Equator with an orbital period matching the Earth's rotation. From the perspective of an observer on Earth, a satellite in GEO maintains a fixed position in the sky, greatly simplifying antenna pointing. More generally, geosynchronous orbit (GSO) also has an orbital period matching Earth's rotation but with any inclination (angle from the equatorial plane); that is, not necessarily directly above the Equator[1]. From an approximate altitude of $35,800\,\mathrm{km}$, a satellite in GEO can have a line-of-sight link to a large percent of Earth's surface reducing the number of spacecraft needed for wide coverage. A disadvantage of the high orbit is the large speed-of-light propagation delay resulting in high latency communications [167].

In light of this challenge, some satellite systems proposed or under current development plan to operate in lower orbits, collectively non-geosynchronous orbit (NGSO). Low Earth orbit (LEO) has altitudes ranging from $160\,\mathrm{km} - 2,000\,\mathrm{km}$ and medium Earth orbit (MEO) spans the region between LEO and GEO. In comparison with geostationary orbits, communication with satellites in NGSO offers reduced path loss and shorter propagation delays [168]. The MEO-based O3b satellite network operates at $8,000\,\mathrm{km}$ [169]. Large

---

[1] For consistency, this text will use the initialism GSO for all geosynchronous orbits, of which GEO is a subset, unless the distinction is relevant to the communication system design problem.

systems ("constellations") of many satellites in low Earth orbit are under development by companies such as SpaceX and OneWeb [14].

Outside of Earth orbit, spacecraft may orbit other planets, their moons, comets, or other bodies. A spacecraft can also maintain a stable position when placed at a Lagrange point, five of which exist in the orbital plane of two large bodies [170]. Spacecraft on the surface of other planets may communicate either directly with Earth or through a relay satellite as is the case with the Mars Science Laboratory (Curiosity) which relays some data through the Mars Reconnaissance Orbiter [171]. Rather than injecting the spacecraft into orbit, mission planners may opt for flybys of celestial bodies. Space agencies require communication with several spacecraft carrying out robotic exploration of the solar system (or even, in the case of Voyager I, interstellar space).

6.2.2 Space Communication Networks

Space communication networks can be broadly divided into those which serve to connect a data source and destination at different locations on Earth and those which exist to serve the communication needs of spacecraft.

6.2.2.1 For Terrestrial Use

The most common use of communication satellite systems is to act as a relay to send information (messages, voice, TV, Internet traffic, etc.) from one point on Earth to another (Fig. 6.1). In satellite terminology used throughout this chapter, the term downlink denotes the link from space to Earth and uplink from Earth to space. A forward link denotes the link from a service provider to a user, consisting of both an uplink to the relay satellite and downlink to the user. A return or reverse link is the opposite: carrying data from a user to the network.

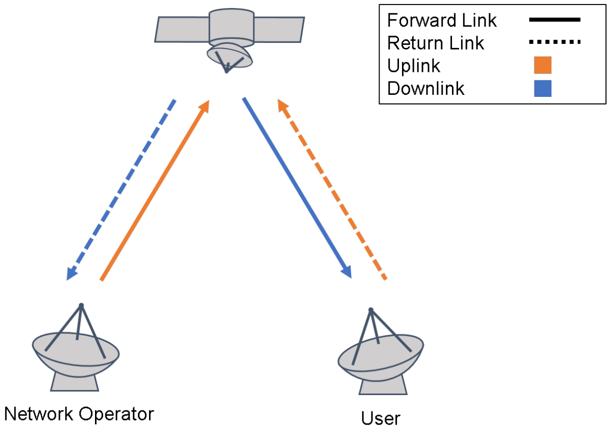

Figure 6.1: Notional diagram of satellite communications to connect two users (a network operator and user terminal) on Earth.

In satellite communication terminology (formally defined by the ITU-R in [172]), fixed-satellite service (FSS) occurs between terminals at given positions on Earth relayed through one or more satellites. Broadcast-satellite service (BSS) distributes a signal uplinked to a satellite (through a feeder link) to many fixed or mobile users. Of particular note in this case is the set of Digital Video Broadcasting - Satellite (DVB-S) standards for satellite broadcast. The second generation set of standards (DVB-S2) [173] and its extensions (DVB-S2X) [174] are considered in several works discussed in this chapter. Historically, satellite-relayed voice and data systems have operated through narrowband mobile satellite service (MSS) systems at 1.5 GHz – 2.5 GHz [175]. However, growing bandwidth demand for mobile applications has led to the development of earth stations on mobile platforms (ESOMPs) which operate within FSS systems. ESOMPs enable broadband in the vehicle-based land, maritime, and aeronautical domains [176].

6.2.2.2 For Space Use

A large number of science missions in Earth orbit communicate data directly to an earth station[2] where it is then transferred to the mission operations center over terrestrial Internet. An earth station could be purpose-built for a mission or part of a network either operated commercially or by a space agency such as the Near Earth and Deep Space Networks operated by the American National Aeronautics and Space Administration (NASA) or the European Space Tracking Network operated by the European Space Agency (ESA). Recent years have seen the development of civilian non-commercial networks of earth stations based on open-source hardware and software such as the Global Educational Network for Satellite Operations (GENSO) [177] or Satellite Networked Open Ground Station (SatNOGS) [178].

6.3 Cognitive Communications Scenarios

To begin, a variety of space communication scenarios are examined in which the cognitive radio techniques discussed in the following sections can be applied. In these applications, cognitive radio is used to allow several systems to coexist and/or improve efficiency and resilience.

6.3.1 Coexistence of Multiple Satellite Systems

Fig. 6.2a depicts a general scenario for coexistence between multiple satellite systems. The earth stations can be fixed location user terminals (though mobile stations are also possible [182]), assets for data exchange and control of spaceborne platforms, or feeder links for broadcast services. In addition to desired signals, each radio will receive interference at a level dependent on the positions of spacecraft and earth stations in a specific scenario. A

---

[2] Satellite communications literature frequently uses earth station, ground station, and earth terminal interchangeably. This work will use earth station, the preferred term in the ITU Radio Regulations [172].

Primary User	Secondary User	Comments	Reference
Terrestrial Fixed Service	Fixed Satellite Service Downlink	17.7 GHz – 19.7 GHz Band	[179, 180]
Terrestrial Fixed Service	Fixed Satellite Service Uplink	27.5 GHz – 29.5 GHz	[179–181]
Terrestrial Fixed Service	Satellite Earth Stations on Mobile Platforms	Aircraft, Ships, and Land Vehicles Considered	[182, 183]
BSS Feeder Link	FSS Downlink	17.3 GHz – 17.7 GHz	[184]
GSO Satellite(s)	NGSO Satellite(s)	Some bands consider GSO and NGSO co-primary users.	[168, 185]
Satellite(s)	Cluster of Satellites	Fusion center combines measurements.	[186]
Mobile Satellite & Terrestrial Repeaters	Terrestrial Cellular	Considers the DVB-SH standard and the 2.17 GHz – 2.22 GHz band	[187]
Meteorological Satellite Earth Station	Terrestrial Cellular	1695-1710 MHz	[188]

Table 6.1: Summary of coexistence scenarios for space communications which involve a secondary system opportunistically using spectrum in which a primary system has priority.

summary of coexistence scenarios studied in the literature is provided in Table 6.1.

If both spacecraft are communication satellites in geostationary orbit, orbital separation and antenna directivity are sufficient to make interference between the two negligible [184]. However, strong interference can occur between two earth stations [179, 189] and between an earth station and a satellite of another system [185]. In the highly directional links common in satellite communications, the level of interference will depend on the off-boresight angle[3] of the transmitter in the direction of the receiver θ_{TX}, the off-boresight angle of the receiver in the direction of the transmitter θ_{RX}, and the distance between transmitter and receiver d. In general, the interference power in dBW is

$$I_{RX} = P_{TX} + G_{TX}(\theta_{TX}) + G_{RX}(\theta_{RX}) - L(d) \tag{6.1}$$

where P_{TX} is the transmitter power in dBW and $G_{TX}(\theta_{TX})$ and $G_{RX}(\theta_{RX})$ the antenna gain of the transmitter and receiver as a function of off-boresight angle in dBi, respectively[4]. In most satellite systems, the total path loss $L(d)$ is dominated by free-space path loss

---

[3] In antenna terminology, the antenna boresight is the axis of maximum gain. Off-boresight angle refers to the angle between boresight and the direction of interest.

[4] The decibel Watt (dBW) is the power of a signal in decibels with respect to a reference level of 1 W. Antenna gains are often specified in decibels relative to isotropic (dBi) in which the reference is the uniform radiation pattern of a hypothetical isotropic antenna.

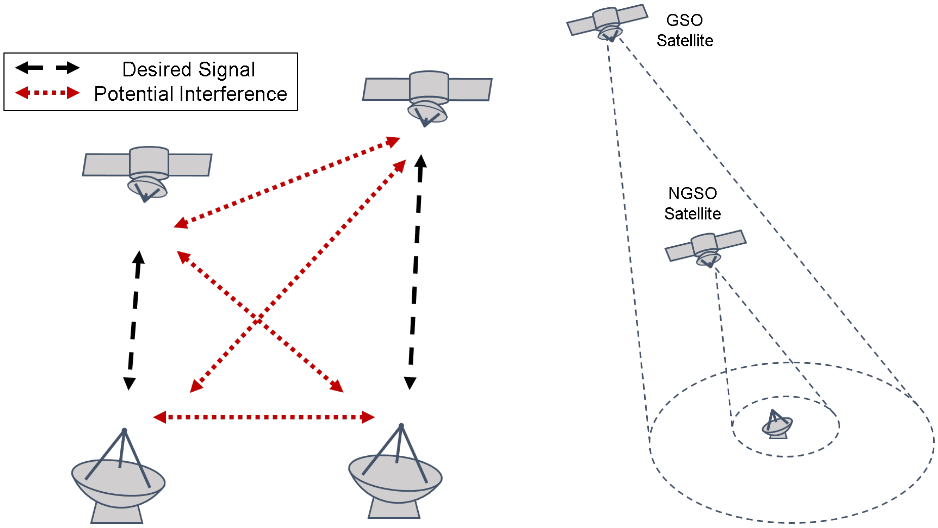

(a) (b)

Figure 6.2: (a) Desired signal (dashed) and potential interference (dotted) between two coexisting satellite systems operating at the same frequency and (b) in-line interference between a GSO and NGSO satellite.

$L_{\mathrm{fsp}}(d) = 20 \cdot \log_{10}(4\pi df/c)$ at carrier frequency f. If the transmitter is located in space and the receiver on Earth, or vice versa, the loss may also include atmospheric loss (e.g. rain fades or gaseous absorption) [17]. For the interfering link between two earth stations, losses due to terrain can be significant [18].

Coexistence of GSO and NGSO satellite systems is particularly notable in light of current and upcoming non-geosynchronous communication satellite constellations. A problem that arises from this application is in-line interference (Fig. 6.2b), caused when an NGSO satellite passes directly between a GSO satellite and earth station [168]. Additional techniques are required to mitigate interference and enable coexistence [185]. In space, inter-satellite links between multiple spacecraft are another area for application of cognitive coexistence techniques [186].

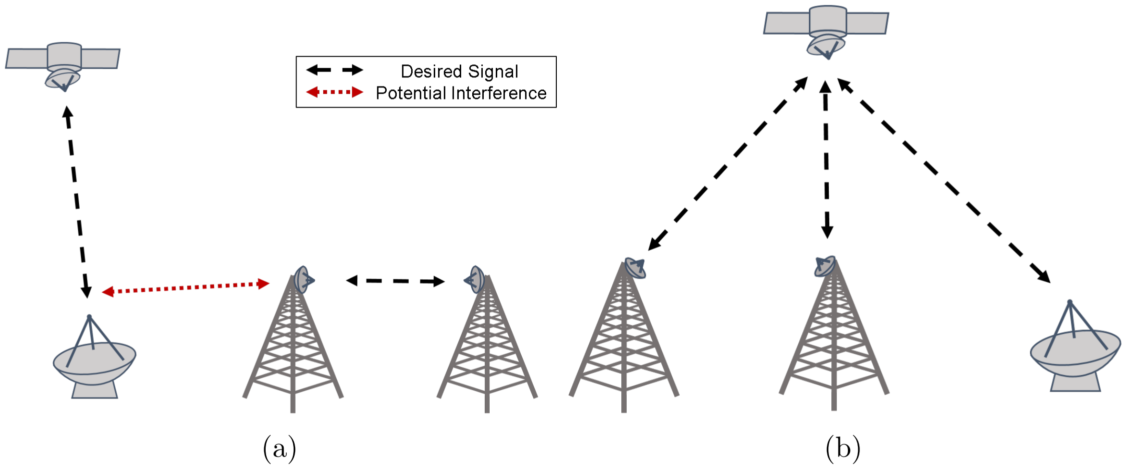

Figure 6.3: (a) Desired (dashed) and potential interference (dotted) between terrestrial and (b) satellite systems operating at the same frequency and the use of satellite as a backhaul link for terrestrial networks.

6.3.2 Coexistence of Satellite and Terrestrial Systems

Significant attention has been focused on coexistence between terrestrial and satellite systems, both for spectrum access by satellites in bands where terrestrial systems have priority and vice versa. As a motivating example, consider the shared 17.7 GHz – 19.7 GHz band which is available to both satellite as well as terrestrial fixed services (FS) such as microwave backhaul links between cellular base stations [172]. Additional restrictions in Europe designate FS as the primary system [190]. A study in [18] shows that among terrestrial fixed stations in the UK, 96% of links use only one or two channels within this band, the majority of which have bandwidth between 3.5 MHz – 55 MHz. It is reasonable to conclude that the 2 GHz of bandwidth in the 17.7 GHz – 19.7 GHz band is underutilized most of the time allowing opportunistic deployment of additional satellite systems provided they meet regulations limiting interference to existing systems.

6.3.2.1 Satellite Use of Terrestrial Spectum

Scenarios considered in [179, 191] discuss satellite services as a secondary user of spectrum allocated to terrestrial fixed service as an incumbent (Fig. 6.3a). The strongest interference is between the terrestrial links and the satellite earth stations. More specifically, in the downlink scenario, cognitive techniques may be required to protect the secondary satellite receivers from interference generated by primary terrestrial transmitters. In the uplink scenario, cognitive techniques are required to protect the primary terrestrial receivers from the potentially harmful interference of secondary satellite transmitters. Similarly, recent ITU regulations [172] allow Earth observation satellites in the 37.5 GHz – 40.5 GHz band to use terrestrial spectrum opportunistically which requires some mitigation to reduce interference [192]. Coexistence becomes more challenging when mobile platforms (i.e. ESOMPs) are considered since interference to incumbent terminals varies over time due to mobility [183].

6.3.2.2 Terrestrial Use of Satellite Spectrum

The introduction of new terrestrial technologies including fifth generation (5G) mobile wireless will require additional spectrum [193]. At the same time, a new emphasis on small cells allows low-power base stations to access spectrum in regions where traditional high-power base stations cannot exist [194, 195]. A recent FCC decision made the 1695 MHz – 1710 MHz band available for cellular use [196], but requires the new systems to avoid causing harmful interference to meteorological satellite (METSAT) earth stations (which may require power allocation strategies as discussed in [188]). Similarly, work in [187] also proposes to reuse the satellite services to handhelds (DVB-SH) band at 2.17 GHz – 2.22 GHz for terrestrial cellular use.

6.3.2.3 Cooperative Enhancement of Terrestrial System with Satellite Links

A promising application of cognitive radio is the enhancement of terrestrial systems with the addition of satellite communications. Work in [197, 198] discusses a hybrid satellite-terrestrial system which uses satellite links in place of terrestrial backhaul links between fixed locations in a cellular network (Fig. 6.3b). A hybrid satellite-terrestrial system is proposed for the IEEE 802.22 cognitive WRAN which takes advantage of the satellite's altitude as an additional spatial degree of freedom to reduce mutual interference [199]. Also within the IEEE 802.22 framework, a satellite can be used as a fusion center to combine spectrum sensing measurements and control spectrum access among a number of cognitive cellular base stations [42, 200]. The overlay spectrum sharing paradigm can also be applied to a hybrid satellite-terrestrial system. Work in [201] considers a base station which serves a network of secondary users as well as relays transmissions between a satellite and a terrestrial primary user.

6.3.3 Link Optimization In Dynamic Environments

After spectrum access is established, space communication links experience a challenging and dynamic environment. As discussed above, frequencies used in space communications can be vulnerable to attenuation by rain. The path loss and atmospheric absorption between an NGSO satellite and an earth station varies with elevation angle. Signals received at low elevation angles are weaker, having traveled a greater distance and passed through more atmosphere than when an NGSO satellite is directly overhead. In [202] an interesting case is presented in which structural features periodically block the line-of-sight between an earth station and a radio on the International Space Station causing large and rapid fluctuations in received signal strength. An area of significant interest in cognitive radio for space communications is adapting physical-layer parameters to varying conditions. In

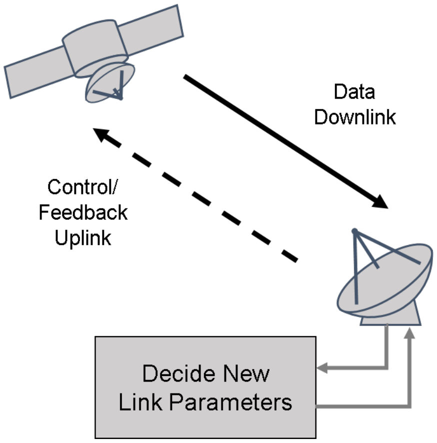

Figure 6.4: Example feedback-based system to dynamically adjust link parameters. A decision engine analyzes the quality of the data downlink (solid), decides a new set of link parameters according to some optimization metric, and communicates those parameters back to the transmitter over a control/feedback uplink (dashed).

all these cases, adaptation at the physical layer allows for high efficiency communications during favorable conditions while maintaining robust links in poor conditions.

A general representation of a link optimization system is shown in Fig. 6.4. The data receiver characterizes the received signal and uses some metric to decide a new set of parameters. Parameters adjusted can include power, modulation, error correction coding, link rate, or a multi-parameter optimization to adjust several parameters at the same time. Using a feedback link, the receiver communicates the new set of parameters to the data transmitter. The performance of such a system is dependent on the update rate and latency of the feedback loop and the ability of the receiver to intelligently select new parameters. Automatic modulation classification [203] and channel prediction [204] can help reduce the reliance on a feedback link. Furthermore, an ideal cognitive radio would be capable of learning from past performance to improve parameter selection [47, 202].

6.3.4 Intelligent Networking and System Management

A theme of future space communications architecture is the transition away from point-to-point links to an integrated space communication network. Inter-satellite links [15] allow data to be relayed between a constellation of satellites in Earth orbit [205]. Deeper in space, organizations have the long-term goal of transforming point-to-point deep space communications into an interconnected "solar system Internet" [16] with special upper layer protocols designed to handle large delays and frequent disruptions [19]. Realizing this goal requires systems that are even more complex than point-to-point links with many additional parameters to optimize. Building CR networks and using cognitive techniques at the upper layers of the protocol stack has not been explored in the same depth as physical-layer techniques in the space communications literature. Nonetheless, there exists the potential to realize large performance gains by injecting cognitive techniques into multiple functionalities of a radio network [206]. Scenarios discussed in the literature include dynamic selection of routes among spacecraft [207] and predictive scheduling of assets in a system of earth stations [208].

6.4 Dynamic Determination of Spectrum Occupancy

Critical to the success of any shared access cognitive radio system is the determination of when spectrum is available for use. Literature on cognitive space communications offers solutions in three broad themes: use of a spectrum database, spectrum sensing, and spectrum availability prediction. Techniques presented in this section allow a user to determine spectrum occupancy and estimate the level of interference caused to other (primary and/or other secondary) users.

6.4.1 Database Access

The use a of a database shared between secondary users or between primary and secondary systems is a promising approach towards managing access in a shared spectrum system. A database can contain regulatory information on which entities hold licenses and measured or reported data of how often licensees operate on a given frequency in a geographic area. For satellite communications, the database may also contain the location of earth stations and orbital parameters of satellites. These databases can be used by a secondary system and combined with sensing and predictive tools to infer spectrum occupancy. The use of a shared database can also allow a primary system more explicit control over secondary access. In the Licensed Shared Access (LSA) concept, under development for terrestrial wireless networks [209] and proposed for satellite communications [165], a set of conditions and quality of service guarantees are negotiated between a primary user and one or more approved secondaries. In cognitive communications with primary-secondary cooperation, primary systems publish information to aid spectrum sharing.As an example, consider the beamhopping satellite application discussed in [210]. A beamhopping satellite is a multibeam satellite which only uses a few of many possible RF beams at any one time in order to save power or better respond to traffic demands [211]. As proposed in [210], a shared database could be employed to inform a secondary system of the primary satellite's beamhopping pattern and allow secondary users to operate in regions covered by a primary beam that is not currently active.

Work in [18] describes the establishment of a database used by a secondary satellite system coexisting with incumbent terrestrial fixed service links. It is noted that locations of FS terminals are generally reported to regulators and could be realistically obtained by a database operator. With knowledge of the locations of FS primaries, the authors use an interference modeling engine based on ITU-R recommendations [212] and a terrain database to model interference levels at increasing distance from the fixed station. Interference levels are used to establish "cognitive zones" within which the secondary must employ cognitive radio techniques to mitigate interference (received or transmitted). Outside the cognitive zone, the interference is such that no additional techniques are needed. Detailed calculation of cognitive zones around a satellite station is presented in [184]. When connected to a spectrum database, secondary systems can then use adaptive techniques to control spectrum access and mitigate interference by adjusting power [187], frequency [213], beamforming [214], pointing [192], and other parameters. A database shared between systems can help mitigate the in-line interference problem between NGSO and GSO satellites introduced in Section 6.3.1. If a primary GSO satellite system shares the orbits, beam patterns, and locations of its earth stations, power control and other techniques can be used by the NGSO system to mitigate in-line interference [168, 185].

6.4.2 Spectrum Sensing

Database use alone may not be sufficient to detect the presence of primary users. For example, in the IEEE 802.22 cognitive WRAN standard, both the use of a spectrum database and spectrum sensing is required to sufficiently protect incumbents [43]. This section will describe spectrum sensing techniques for space communications that have been investigated in the literature. In the following section, consider a primary user signal $x(t)$ received at a secondary user terminal over a channel h, assumed to be static over a sensing time of τ seconds. The received signal $y(t)$ contains the primary user signal plus white noise $z(t)$ and is expressed as $y[n]$ after sampling at a rate f_s. For opportunistic transmission in white spaces, it is sufficient to detect the presence or absence of a primary user by solving a binary

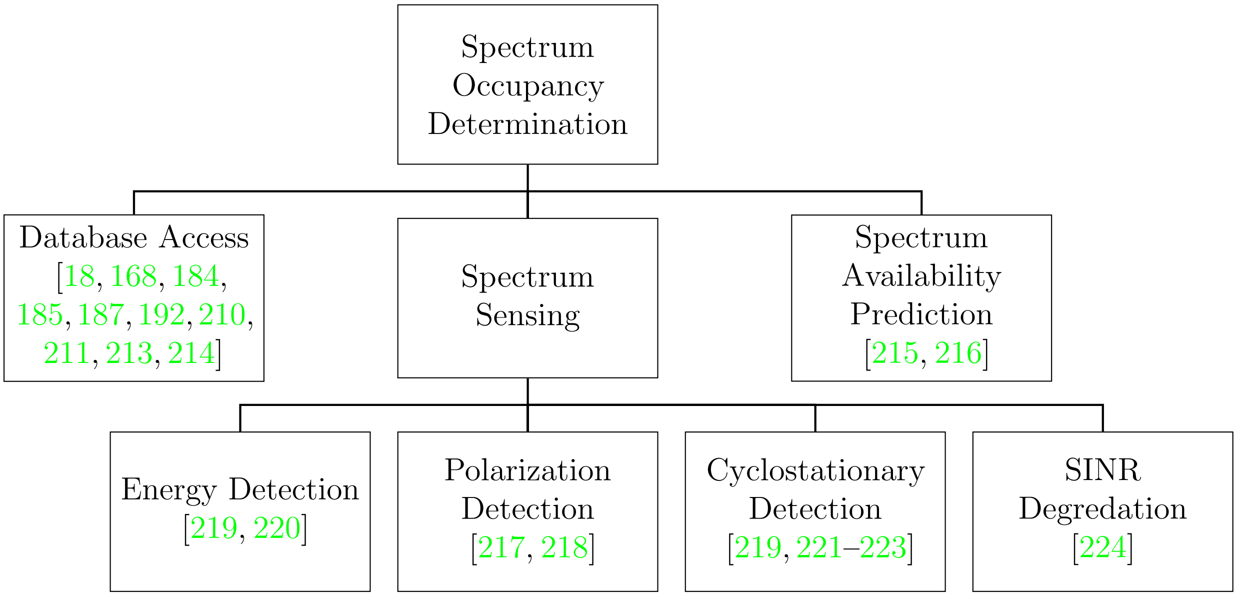

Figure 6.5: Summary of spectrum occupancy determination methods used in space communications.

hypothesis problem:

$$\begin{aligned} \mathcal{H}_0 &: y[n] = z[n] \\ \mathcal{H}_1 &: y[n] = hx[n] + z[n] \end{aligned} \tag{6.2}$$

6.4.2.1 Energy Detection

In energy detection, the test statistic

$$\mathbb{T} = \sum_{n=1}^{N} |y[n]|^2 \underset{\mathcal{H}_0}{\overset{\mathcal{H}_1}{\gtrless}} \lambda_{th} \tag{6.3}$$

is calculated over an interval of $N = \tau f_s$ samples and can be approximated as Gaussian [225]. The selection of the threshold λ_{th} is a trade-off between the probability of detection $\mathcal{P}_d = \Pr(\mathbb{T} > \lambda_{th}|\mathcal{H}_1)$ and the probability of false alarm $\mathcal{P}_f = \Pr(\mathbb{T} > \lambda_{th}|\mathcal{H}_0)$. For a signal with average power P and noise variance σ_z^2 the probability of detection is a function of the average signal-to-noise ratio (SNR)

$$\gamma = \frac{P}{\sigma_z^2} \tag{6.4}$$

$$\tag{6.5}$$

and the number of samples N [226]. However, uncertainty in the noise variance limits the probability of detection that can be achieved at a given SNR even with extremely large N, a phenomenon called an “SNR wall” [227].

In [219] the authors consider energy detection at an FSS terminal. A rise-over-thermal metric is used to set λ_{th} to achieve a high $\mathcal{P}_d$ when the interference level is 6% above the thermal noise floor, the maximum tolerable interference level per [228]. Note that the signal model in (6.2) considers that the secondary transmitter ceases transmission during this sensing period, reducing network throughput. Alternatively, secondary signals with known pilots can be transmitted and subtracted from the received signal leaving only noise and primary user transmissions [219, 220].

6.4.2.2 Polarization Detection

Energy detection can be further improved by exploiting the polarization of a signal. Antennas for terrestrial communications typically use linear (such as vertical or horizontal) polarization while satellite antennas employ circular (left-hand or right-hand) polarization [166]. Additional satellite throughput can be achieved using dual polarization to create a 2 input and 2 output multiple-input and multiple-output (2 × 2 MIMO) channel [229]. By using several orthogonally polarized antennas at a secondary receiver, polarization can be used to enhance spectrum sensing and, once detected, exploited as an additional degree of freedom for cognitive communications [217, 218]. For the case that the primary transmitter and secondary spectrum sensing receiver each have two antennas, the received signal vector $\mathbf{y} = [y_V[n] y_H[n]]^T$ can be written in terms of the channel coefficients, with the subscript H denoting horizontal polarization and V denoting vertical polarization

$$\begin{bmatrix} y_V[n] \\ y_H[n] \end{bmatrix} = \begin{bmatrix} h_{HH} & h_{HV} \\ h_{VH} & h_{VV} \end{bmatrix} \begin{bmatrix} x_V[n] \\ x_H[n] \end{bmatrix}. \tag{6.6}$$

There are several ways to design the test statistic [218]. One such choice is maximum ratio combining, in which the total test statistic is a weighted sum of individual test statistics for the vertical ($\mathbb{T}_V$) and horizontal ($\mathbb{T}_H$) cases individually.

$$\mathbb{T} = w_v \mathbb{T}_v + w_h \mathbb{T}_h \tag{6.7}$$

after which a threshold λ_{th} can be applied as before.

6.4.2.3 Cyclostationary Detection

Detection in the low SNR regime can be improved by exploiting the underlying periodic characteristics of most signals used for communication. This cyclostationary property may be introduced by the modulation, spreading, pilots, or frame structure of a signal. The cyclic spectral density (CSD) function of $x[n]$ at cycle frequency α is defined as [230, 231]

$$S_x^\alpha(f) = \sum_{m=-\infty}^{\infty} R_x^\alpha(m) e^{-j2\pi f m} \tag{6.8}$$

for cyclic autocorrelation function

$$R_x^\alpha(m) = \lim_{N\to\infty} \frac{1}{N} \sum_{n=0}^{N-1} x[n] x^*[n+m] e^{-j2\pi\alpha n}. \tag{6.9}$$

The hypothesis (6.2) can be rewritten in terms of the CSDs of the received signal, $S_y^\alpha(f)$ and transmitted signal $S_x^\alpha(f)$.

$$\begin{aligned} \mathcal{H}_0 &: S_y^\alpha(f) = S_z^\alpha(f) \\ \mathcal{H}_1 &: S_y^\alpha(f) = S_x^\alpha(f) + S_z^\alpha(f) \end{aligned} \tag{6.10}$$

Since white Gaussian noise processes exhibit no periodicity the CSD of received AWGN, $S_z^\alpha(f)$, is ideally zero for $\alpha = 0$. The test statistic can be written as

$$\mathbb{T} = \int_\alpha \int_f \left| S_y^\alpha(f) \right|^2 df d\alpha \tag{6.11}$$

with probability of detection $\mathcal{P}_d = \Pr(\mathbb{T} > \lambda_{th} | \mathcal{H}_1)$ for some threshold λ_{th}.

Cyclostationary feature detection for satellite communications has been considered in [219, 221]. A testbed for developing cyclostationary detection to be applied to satellites is described in [222]. Experimental tests are carried out in [223] where the authors try to detect the presence of satellite transmissions in a given band. Cyclostationary detection is provably able to detect signals at a much lower SNR than energy detection. In certain spectrum sensing schemes, it may be a disadvantage for the secondary system to detect signals that are weaker than would typically cause appreciable interference. It is suggested in [219] to sense the spectrum in two stages, with energy detection followed by cyclostationary detection for low SNR signals.

6.4.2.4 Compressed Sensing

A challenge for spectrum sensing in the satellite domain is that bands of interest cover a wide frequency range of several GHz but primary user signals have a bandwidth on the order of 10s of MHz. Gathering samples over a wide band presents a challenge to radio front-ends and analog-to-digital converters which are required to maintain a sampling rate greater than or equal to the Nyquist rate $f_s \geq 2(f_{max} - f_{min})$. Work in [232] proposes compressed sensing for spectrum occupancy determination at sub-Nyquist sampling rates. The authors demonstrate significant performance improvement over Fourier transform-based spectrum sensing over a wide frequency range.

6.4.2.5 SINR Degradation

Solving the binary hypothesis problem in (6.2) enables opportunistic transmissions in spectrum that is unoccupied. However, transmitting at the same time and frequency as primaries subject to interference constraints is also possible. This approach requires estimating not only the presence but the intensity of primary user transmissions to evaluate suitable bands for secondary use. The authors in [224] consider this scenario and present a joint detection and interference estimation technique for satellite primary users. Secondaries use a frame format with known pilot symbols (e.g. DVB-S2) from which the signal-to-interference-plus-noise ratio (SINR) of the link is estimated and SINR loss due to interference is tracked. A potential downside of this technique is the assumption that SINR loss is due to interference and not other effects such as rain fades which can also degrade a signal.

6.4.2.6 Fusion

Detection accuracy can be further improved by combining the results of several spectrum sensing receivers that operate at different orbits or geographical locations. This cooperative approach to spectrum sensing can compensate for the “hidden incumbent” problem which can arise if channel conditions or blockage prevent an individual secondary user from sensing the presence of a primary [233]. In cooperative spectrum sensing, a network of secondary users communicate their sensing results to be combined at a fusion center. The fusion center then either communicates the combined occupancy results back to the users or each user queries the fusion center before it accesses spectrum. In [186], this concept is applied to a cluster of secondary satellites which perform spectrum sensing to detect the presence of a primary satellite link. Each secondary communicates a 1-bit sensing result ("primary absent" or "primary present") to a fusion center (assumed to be on Earth). For maximum protection of the primary, individual sensing results are combined by an OR rule: the band is determined available only if all local results indicate the primary is absent. The individual probabilities of detection $\mathcal{P}_d^{(k)}$ and false alarm $\mathcal{P}_f^{(k)}$ of the k-th user are used to create combined probabilities

$$Q_d = 1 - \prod_{k=1}^{K} \left[1 - \mathcal{P}_d^{(k)}\right]^{w_k} \tag{6.12}$$

$$Q_f = 1 - \prod_{k=1}^{K} \left[1 - \mathcal{P}_f^{(k)}\right]^{w_k} \tag{6.13}$$

where K is the total number of local sensing results and weight $w_k \in [0, 1]$ is a normalized ($\sum_{k=1}^{K} w_k = 1$) measure of trust for the k-th local sensing result [186].

Fusion of spectrum sensing results for cognitive space communications is discussed in [232] where a fusion center combines compressed sensing results and [224] where secondary spectrum access is controlled through a network control center. The concept is also extensible to satellite-aided terrestrial networks. The use of a satellite to combine spectrum sensing results from multiple base stations is studied in [234]. A sensing/fusion center satellite can be used to distribute spectrum occupancy measurements [200] or control spectrum access [42] among base stations.

6.4.3 Spectrum Availability Prediction

Determining spectrum occupancy through sensing, database access, or a combination of the two can be challenging due to the potentially large propagation delays and intermittent link availability experienced in space communications. To address this, several works consider using spectrum sensing to not only determine current occupancy, but inform models which predict future spectrum availability.

The authors in [215] use a long short-term memory network to predict future availability by exploiting the spectral-temporal correlation of past spectrum occupancy data. In [216] the primary user activity is modeled as a Markov on-off process in which the primary user is either active or idle at a given time slot. Using 0 to denote idle and 1 to denote active, the set of transition probabilities are $\{p_{00}, p_{01}, p_{10}, p_{11}\}$ where p_{ij} denotes the transition probability from state i to state j. Energy detection is used to count the number of transitions between consecutive time slots from idle to idle, idle to busy, busy to idle, and busy to busy (denoted as n_{00}, n_{01}, n_{10}, and n_{11}). The transition probabilities are then estimated as

$$\hat{p}_{ij} = \frac{n_{ij}}{n_{i0} + n_{i1}} \tag{6.14}$$

A hazard of this approach is the potential for collisions if the primary user activity is unpredictable or changes behavior from previous observations.

6.4.4 Sensing Analysis

To provide insight into the practical application of spectrum sensing for dynamic access among spaceborne platforms, the energy detection discussion in Section 6.4.2.1 is expanded by providing simulations of the inter-satellite distances between LEO satellites at which spectrum sensing is feasible. When a satellite is transmitting, there exists a three-dimensional zone inside which another satellite can detect its transmissions. This knowledge can be exploited by the sensing satellite to dynamically access spectrum, take measurements for a spectrum use database (Section 6.4.1), or develop a model of transmitting satellite activity (Section 6.4.3). The dimensions of the zone depend on the center frequency, distance between satellites, off-boresight angle to the sensing satellite, and the required signal level at the sensing satellite.

6.4.4.1 Energy-Detection Spectrum Sensing Limitations

The SNR wall phenomenon described in [227] is caused by uncertainty in the noise variance $\sigma_z^2 \in [(1/\rho)\sigma_z^2, \rho\sigma_z^2]$ with parameter $\rho > 1$ quantifying the uncertainty. Reasonable estimates for the value of ρ are in the range of $0 - 2$ dB [235]. Under this uncertainty, the minimum number of samples N_{min} required to achieve target detection $\bar{\mathcal{P}}_d$ and false alarm $\bar{\mathcal{P}}_f$ probabilities is calculated as [219, 226]

$$N_{min} \geq \frac{\left[Q^{-1}(\bar{\mathcal{P}}_f) - Q^{-1}(\bar{\mathcal{P}}_d)\sqrt{2\gamma + 1}\right]^2}{\left[\gamma - (\rho - \frac{1}{\rho})\right]^2} \tag{6.15}$$

where $Q(x)$ is the tail distribution function of the normal distribution

$$Q(x) = \frac{1}{\sqrt{2\pi}} \int_x^\infty \exp\left(\frac{-t^2}{2}\right) dt \tag{6.16}$$

and $Q^{-1}(x)$ its inverse. With a moderate sampling rate, the SNR wall becomes the limiting factor and N_{min} can be easily satisfied for received SNR greater than the SNR wall

$$\gamma_{wall} = \frac{\rho^2 - 1}{\rho} \tag{6.17}$$

which for the worst case scenario of $\rho = 2$ dB results in $\gamma_{wall} \approx 0$ dB. This limit is used to determine a sensing zone around a transmitting satellite within which it is possible to sense transmissions (i.e. $\gamma \geq \gamma_{wall}$). Though more sophisticated methods (Sections 6.4.2.2 - 6.4.2.6) could operate at lower SNR, the results in this section serve as a starting point to develop intuition on the feasibility of in-space spectrum sensing among satellites.

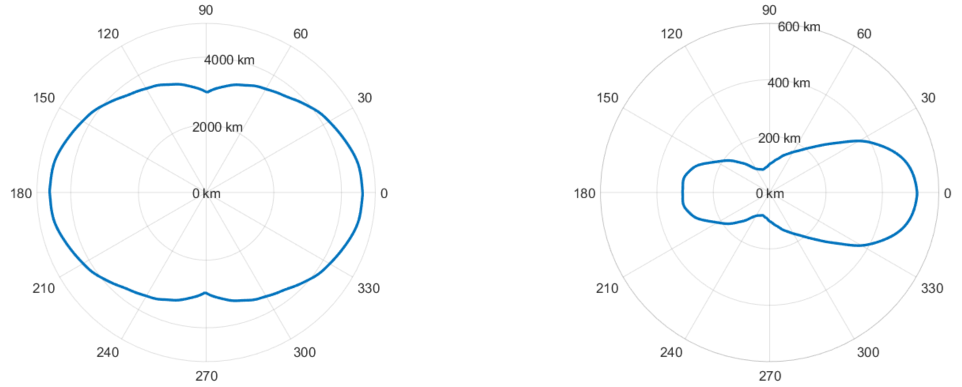

(a) (b)

Figure 6.6: Sensing zones around satellites at (a) UHF and (b) S-band as a function of off-boresight angle and distance between the primary transmitting and secondary sensing satellite.

6.4.4.2 Simulation Results

In the simulation, consider the transmitting and sensing satellites to be identical with parameters as specified in Table 6.2. The antenna boresight of the transmitting satellite is directed at Earth while the antenna boresight of the sensing satellite is pointed at the transmitting satellite. Two bands in the Amateur Satellite Service allocation regularly used by small spacecraft are considered: the ultra high frequency (UHF) band at 435 MHz – 438 MHz and the S-band allocation at 2.40 GHz – 2.45 GHz [172]. Satellites in both bands are assumed to have a noise figure of 5 dB and a transmit power of 1 W, typical for a small satellite platform. A popular UHF antenna configuration is a deployable dipole [236]. The simulation uses the antenna pattern of a commercially available small satellite antenna [237]. At S-band, patch antennas integrated into the outer faces of the satellite body are considered [238, 239].

From Fig. 6.6a it can be observed that the UHF sensing zone is nearly uniform with a maximum distance of approximately 4600 km. In contrast, the higher directivity of the S-band antenna is reflected in the sensing zone in Fig. 6.6b. The free-space path loss at this higher frequency reduces the maximum sensing distance to approximately 520 km

Parameter	UHF	S-band
Center Frequency	435 MHz	2450 MHz
Bandwidth	15 kHz	1 MHz
Noise Figure	5 dB	5 dB
Transmit Power	1 W	1 W

Table 6.2: System parameters for sensing zone simulation.

at antenna boresight (with the sensing satellite directly in line between the transmitting satellite and Earth) and 85 km at ±90° off-boresight. The additional directivity and path loss will limit the applicability of those terrestrial dynamic spectrum access techniques which assume all users in a given location can overhear transmissions from all other users. However, inter-satellite distances in clusters of small satellites may be as short as 2 km − 10 km which implies the possibility of in-space sensing among a cluster for medium access control [15]. At the low path loss and quasi-omnidirectional antenna patterns encountered in UHF space communications, satellites are able to sense transmissions within a wide area. Fig. 6.7 illustrates this by plotting actual orbits of operational small satellites in LEO obtained from a database [240] with the transmitting satellite chosen at random. To conclude, even in the space environment UHF links can be treated similar to omnidirectional terrestrial radios when applying dynamic access techniques. At S-band, additional path loss and directivity limits spectrum sensing opportunities, though dynamic spectrum access techniques may still be applicable within a cluster of small satellites.

6.5 Physical Layer Techniques

Adaptive and cognitive techniques at the physical (PHY) layer serve two purposes: (i) enable opportunistic access by controlling transmission parameters to coexist with primary user systems in shared spectrum and (ii) maintain robust links in dynamic channel conditions or

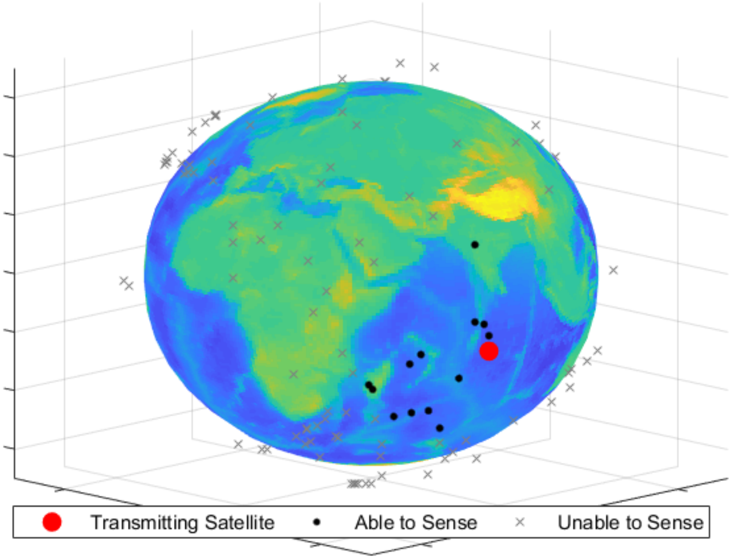

Figure 6.7: Satellites (black) within the sensing zone of a transmitting satellite (red) at UHF frequencies. Sensing satellites in orbit are able to detect transmissions over a long distance.

varying levels of interference. In the latter scenario, there need not be a primary system; a cognitive space communication platform can improve its resiliency and efficiency by adapting PHY-layer parameters even when operating on exclusively licensed spectrum.

6.5.1 Automated PHY-Layer Parameter Detection

Automatic modulation classification (AMC) is useful to a cognitive radio system in two ways. First, knowledge of an interfering signal's PHY-layer parameters can help inform specific methods to mitigate interference. Second, in cases where modulation is changed on a frame-by-frame basis in order to adapt to changing channel conditions, reliable AMC eliminates the need for a feedback loop or header information to communicate changes in modulation settings. AMC has been studied broadly in the literature (see [241] and the references within) and has recently been investigated in the context of space communications.

The goal of AMC is to correctly determine which modulation A from a set $\mathcal{A}$ of all possible candidates was used to modulate a received signal. Common to the methods discussed in this section is the process of extracting features from received signals and calculating the most probable modulation from the set of features. The authors in [203] create a feature vector by calculating the cyclic spectral density in (6.8) from a received signal. After preprocessing, the CSD-based feature vector is fed into a neural network which returns the most probable modulation scheme. In simple mathematical terms, a neural network maps an input vector $\mathbf{r}_0 \in \mathbb{R}$ to an output vector $\mathbf{r}_L \in \mathbb{R}$ by performing mappings $f(\mathbf{r};\theta)$ across L layers

$$\mathbf{r}_l = f_l(\mathbf{r}_{L-1};\theta_L), \quad l = 1,\ldots,L \tag{6.18}$$

where the set of parameters $\{\theta_1,\ldots,\theta_L\}$ is learned through a training process [46].

Other common choices of features for AMC include statistical moments and higher-order cumulants. The use of cumulant-based AMC for satellite communications is investigated in [242]. Assuming the received signal $y[n]$ is a stationary zero-mean process, its cumulants are generated as

$$C_{pq} = E\left\{y[n]^{(p-q)}y^*[n]^{(q)}\right\} \tag{6.19}$$

A feature vector of cumulants with various values of p and q are processed by neural network to produce modulation predictions. Imperfections due to the inclusion of headers and pilots, carrier frequency offset, and amplifier nonlinearity are also considered in the study. "Multiuser" AMC for satellite links is considered in [243]. In this scenario, two or more signals overlap in frequency. The authors propose the Mth-power nonlinear transformation (MPT) method for blind multiuser AMC as it is less sensitive to time and frequency synchronization issues. Taking N samples of the received signal $y[n]$, the

M^{th}-Power Nonlinear Transformation (MPT) is [244]

$$M_i\text{PT}_y(f) = N_s^{\left(\frac{-2}{M}\right)} \left| \sum_{n=0}^{N} y^M[n] e^{-j2\pi fn} \right|^{\left(\frac{2}{M}\right)} . \tag{6.20}$$

After additional processing, a set of MPTs for different values of i are assembled into a feature vector $\mathbf{\Pi}$. A candidate feature vector $\mathbf{\Pi}_{th}^{A}$ is generated from theory for each modulation candidate $A \in \mathcal{A}$. The measured $\mathbf{\Pi}$ is compared to the set of theoretical candidate feature vectors to obtain the estimated modulation

$$\hat{A} = \underset{A \in \mathcal{A}}{\operatorname{argmin}} \, ||\mathbf{\Pi} - \mathbf{\Pi}_{th}^{A}|| \tag{6.21}$$

The identified modulation can then be used for interference mitigation or parameter adjustment.

6.5.2 Dynamic Power Allocation

A common example of adaptive and intelligent techniques for link optimization is dynamic power allocation. While the transmit power of a signal can be changed in response to varying channel conditions, much of the cognitive space communications literature uses power control to mitigate the interference to a primary or co-primary user. A decentralized game theory solution to power allocation among small satellites communicating with a master satellite is considered in [245]. Each of K satellites acts independently to set a power level $P_k \in \mathbb{R}$ between 0 (off) and P_{max} with the goal of maximizing a utility function

$$u_k = r_k(\mathbf{p})/P_k - \beta P_k \tag{6.22}$$

where $r_k(\mathbf{p})$ is the throughput of the k-th satellite, which is proportional to SINR and therefore depends on the power allocations of all satellites in the network $\mathbf{p} = [P_0 \, P_1 \, P_K]$. A pricing factor β mitigates aggressive behavior.

Interference mitigation by power control between primary and secondary systems generally involves solving (6.1) for P_{TX} so as to keep I_{RX} below a pre-defined threshold. In space, the loss between radios is dominated by free space path loss. However, much of the literature considers coexistence of satellite and terrestrial systems. Terrain models combined with guidelines for loss calculations [212, 246] can be used to estimate the interference a primary is subjected to for a given transmit power level [182, 187]. However, database access can also be used. Work in [197, 213] proposes sharing the channel state information (CSI) of signals received at a primary with the secondary network. Exact knowledge of CSI would provide very accurate power control, though the authors in each work analyze alternative approaches for the case of incomplete information. The sharing scenario between secondary terrestrial base stations and primary meteorological satellite receivers in [188] does not consider full CSI to be available, but assumes the mean and variance of channel gains are known. Over a large secondary network there will likely be (i) many mobile users with both high channel gain to a base station and low channel gain to the primary receiver and (ii) enough users such that the variance of interference received at the primary is small. Taking advantage of the averaging effect of many allocated users, the authors propose power allocation that will meet the interference constraint on average with little likelihood of violating it at any given time.

6.5.3 User Channel Selection

In [247], a genetic iterative algorithm assigns users to channels taking into consideration the availability of channels and the potential increase in capacity by reallocating a user. The application of deep reinforcement learning to allocate channels among earth stations in a multibeam satellite system is discussed in [248]. Noting that co-channel interference largely depends on the relative location of user terminals, and in order to exploit the advantages of convolutional neural networks (CNNs) for image processing, the system state is represented by a series of images. An image is created for each channel with a pixel representing the presence/absence of an existing or new user terminal. From the series of images, the CNN approximates the probability of blockage for each choice of channel to be allocated to the new user.

6.5.4 Waveform Optimization

The adaptive coding and modulation feature of the DVB-S2 standard provides a mechanism to dynamically adjust the data rate of a link to account for time-varying effects like rain fading. In favorable channel conditions, high-order modulations and high-rate (low-redundancy) forward error correction (FEC) are used to increase spectral efficiency and data rate. In poor channel conditions, lower order modulation allows recovery at lower SNR and low rate FEC provides additional redundant bits to correct errors and maintain connectivity. The system operator must determine which set of modulation and code rate to use for given channel conditions. Experimental results in [202] show the benefit of using a neural network to make this decision. In the scenario described, SNR variation is primarily due to line-of-sight blockage and multipath fading from the structural features of the ISS. From the current value of signal strength measured at the earth station, the neural network selects the modulation and coding to maximize data rate while maintaining a target link margin. The transmitter is updated with the new parameters through a feedback link (Fig. 6.4). A feedback system using adaptive modulation for a satellite in GSO is considered in [204]. To combat out-of-date channel information due to the large propagation delay, Kalman filters are used to predict the impact of rain fading. At each time instance, the filter incorporates the latest SNR measurements and predicts future SNR several seconds in advance. Modulation is selected based on the predicted SNR with the goal of maintaining BER below a target threshold.

6.5.5 Joint Multi-Parameter Optimization

A typical space communication link has many parameters to adjust and large performance gains can be realized by optimizing parameters jointly rather than individually. In the joint carrier allocation and beamforming scheme proposed in [249], weight vectors are applied to focus the response of a receive antenna array on an FSS satellite of interest while mitigating interference from nearby BSS feeder links. A rate matrix $\mathbf{R}$ is formed where the $[\mathbf{R}]_{m,k}$ denotes the achievable data rate for the m-th available carrier frequency at the k-th FSS receiver after optimizing SINR through beamforming. The sum-rate of the system is maximized by the optimization

$$\begin{aligned} &\max_{\mathbf{A}} ||\text{vec}(\mathbf{F} \odot \mathbf{R})||_1 \\ &\text{s.t.} \quad \sum_{k=1}^{K} [\mathbf{F}]_{:,k} = 1 \end{aligned} \tag{6.23}$$

where $\odot$ is the Hadamard product, $\text{vec}(\cdot)$ the vectorization operator, $||\cdot||_1$ the L1-norm, and $\mathbf{F}$ an allocation matrix with $[\mathbf{F}]_{m,k} = 1$ if the m-th carrier is assigned to the k-th user, and 0 otherwise. The constraint in (6.23) that the sum of each column of $\mathbf{F}$ must equal 1 enforces exclusive allocation of only one user to each carrier frequency. The assignment problem can be solved in polynomial time using well-known combinatorial optimization methods (i.e. the Hungarian algorithm).

Additional solutions to the problem of maximizing the throughput of a secondary system while protecting a primary system from harmful interference consider joint rate and power allocation [181], joint power, carrier, and bandwidth [180], and joint channel selection and power allocation [213]. Joint beamforming and power allocation is used to minimize power while maintaining quality of service in a hybrid satellite-terrestrial system in [201]. Waveform design and power allocation is combined in [250] for opportunistic satellite transmissions in white spaces.

Q-learning, a reinforcement learning technique, is used to optimize a set of radio parameters across a set of space communication objectives in [47]. Reinforcement learning aims to maximize rewards for actions taken when the radio is in a given state. The quality of a state-action pair is mapped to a reward with a Q-function. The Q-function relevant to the space communication scenario described in [47] is

$$Q_{t+1}(s_t, u_t) = Q_t(s_t, u_t) + \alpha_t r_{t+1} \tag{6.24}$$

where $Q_t(s_t, u_t)$ is the quality of the combination of state s_t and action u_t, respectively, at time t. The reward r_{t+1} is associated with the transition from state s_t to s_{t+1} and the learning rate parameter $\alpha_t \in [0, 1)$ controls how quickly new information is integrated. The authors propose a system with multiple goals of: minimizing bit error rate BER, minimizing power consumption P, maximizing throughput R, and keeping bandwidth W constant. The reward r_{t+1} and next state s_{t+1} are a weighted sum of these four goals with weights determined by mission profile. For example, a power saving mode may prioritize minimizing power while a launch/reentry mode may make minimizing BER a priority. The action $\bar{u}_t = (R_t, M_t, E_{b,t})$ is the set of chosen bit rate R_t, modulation order M_t, and bit energy $E_{b,t}$. The authors note that adjusting one parameter may impact several goals (e.g. increasing modulation order will increase throughput and bit error rate). The parameter $\epsilon \in (0, 1)$ balances the trade-off between exploring new actions and exploiting previous knowledge to choose actions likely to produce the maximum payoff. With probability $1-\epsilon$ the radio will take action $u_t = \text{argmax}_{\bar{u}} Q_t(s_t, \bar{u})$ (exploit) and with probability ϵ will take an action randomly (explore). In the time-critical operations environment of space communications, the time spent exploring potential rewards can be detrimental to mission performance. Extensions of this work [251, 252] integrate a deep neural network for 'virtual exploration' to predict expected rewards for certain actions and eliminate time spent exploring poor-reward actions over-the-air.

6.6 Network and System Management Techniques

Finally, cognitive techniques are also valuable at the network and higher layers of the protocol stack. For example, Q-routing, a reinforcement learning-based routing algorithm [253], can be applied to route selection within a multi-hop network of spacecraft in deep space [207]. In this work, $Q_a(d,b)$ is the time that node a estimates it will take to deliver a packet to final destination d by routing it through intermediate node b. Node a choses the next-hop to minimize total estimated delay

$$\bar{b} = \min_{b \,\in\, \text{neighbors of } a} Q_a(d,b). \tag{6.25}$$

In response, node $\bar{b}$ sends its estimate of the remaining time to the destination over its selected next-hop $\bar{c}$

$$Q_{\bar{b}}(d,\bar{c}) = \min_{c \,\in\, \text{neighbors of } \bar{b}} Q_{\bar{b}}(d,c) \tag{6.26}$$

which is used by a to update its own delivery time estimate

$$Q_a(d,\bar{b}) = (1-\alpha) Q_a(d,\bar{b}) + \alpha \left[Q_{\bar{b}}(d,\bar{c}) + t_a + t_{a\to b} \right] \tag{6.27}$$

where t_a denotes the time spent in node a's queue, $t_{a \to b}$ the propagation time from a to b, and α is the learning rate, respectively. Exploration of new routes is accomplished by forcing each node to transmit over a random link some percentage of the time. In this manner, delivery time estimates are incrementally improved by propagating one-hop delays backwards through the network. The authors in [207] also propose incorporating measured delay-tolerant network metrics such as retransmission requests over a given link to increase decision accuracy.

Experiments involving intelligent routing of data packets from a spacecraft to handle user constraints and time-varying physical-layer link parameters is detailed in [206]. A cognitive agent probes properties of each link available to the spacecraft, such as latency and/or throughput and responds to user-defined constraints attached to data packets. For example, the agent would likely select a direct-to-Earth link for user data with a "low latency" constraint or a high-bandwidth link through a relay satellite for user data with a "high throughput" constraint.

The most expansive application of cognitive radio network technology is automation and management of operational aspects of an entire communication system. In [254] access to NASA's Tracking and Data Relay Satellite System (TDRSS) of seven relay satellites is managed through dynamic service requests initiated by the user spacecraft as opposed to manual coordination from a mission operations center. In such a schedule-based system, a cognitive agent could be used to optimize the selection of allocations and earth stations in response to user requests [208].

6.7 Future Directions

There is great promise and still much to be explored in cognitive space communications. In light of present research this chapter concludes by identifying needs and suggesting areas for future investigation:

- The field of machine learning is rapidly changing, providing opportunities to potentially realize large gains by applying recently developed techniques to cognitive space communications. The performance of a learning algorithm often depends on the size of the data set used to train it. In certain machine learning problems, data set size is more important than the choice of algorithm [255,256]. It is worthwhile for researchers to focus on space communication problems for which large data sets exist or can be generated. Operators of communication systems may consider growing a data set by recording additional parameters and measurements of their system for further analysis.

- Cognitive techniques must be sufficiently reliable to be deployed in expensive or critical missions. This requires extensive testing and validation. For certain algorithms, it may be valuable to run cognitive algorithms in "shadow mode" (operating alongside legacy systems but without applying its decisions) [206]. Furthermore, cognitive algorithms must be evaluated with the resource constraints of spaceborne platforms in mind. Realistic impairments and limitations on sensing, processing, storage, and information sharing must be considered during design and simulation. Beyond simulation, deploying algorithms to testbeds in emulated or actual space environments (e.g. [257]) can advance maturity of the technology.

- Cross-layer interactions must be well understood in cognitive radio networks. Questions as to how dynamic spectrum access and rapidly varying parameters at the physical layer will affect upper layer routing, transport, and application functionalities remains an open question. The ultimate goal of an iCR requires awareness, adaptivity, and cognition across all layers of the protocol stack.

- While many of the techniques in this chapter have discussed RF communication, there is growing interest in free space optical technologies for space communications [258]. Laser-based communication presents its own challenges [259] and the potential exists to integrate cognitive radio into future systems [260].

- From the current literature, dynamic spectrum access using shared databases (Section 6.4.1) appears to be the most well studied and mature technique in the satellite communications domain. Additional work is needed to gather comprehensive databases, interference measurements, coordinate between operators, establish regulatory frameworks, and build operational systems capable of realizing the large predicted performance gain.

Chapter 7

Summary & Conclusion

This dissertation presented novel software-defined radio designs that incorporate adaptive and intelligent wireless communication protocols specifically applicable to several highly challenging environments. Included in this work was a detailed discussion of software-defined radio architecture, platforms, design trade-offs, and future directions compiled from insight gained over years of lab development and field testing with this technology. A hierarchy of cognitive radio functionalities across the protocol stack was used to frame discussion of cognitive radio aspects and applications. Thorough analysis of cognitive radio for space communications was presented along with conceptual simulations and suggestions for future directions. The problem of optimizing all-spectrum code-waveforms in coexistence and contention scenarios was studied and several algorithms to design SINR-maximizing waveforms were proposed. Simulation results show that under certain conditions, waveform design based on single-bit flipping achieves performance close to that of exhaustive search at much lower complexity. An extension of the waveform design problem to a multiple antenna system was offered.

The design and development of a first-of-its-kind large-scale deployment of all-spectrum cognitive networking in a hybrid ground-air environment was demonstrated. A systematic analysis across the physical, medium access control, and network layers of the protocol stack was presented towards the practical realization of the system on software-defined radio platforms. Experimental results demonstrate the cognitive network's superior ability to withstand interference at the physical and network layers compared to a static baseline network. In the underwater domain, a novel feedback-based adaptive spread-spectrum system for underwater acoustic communications was presented. The superior performance of the AV filter in the UW-A environment compared to other adaptive filters was shown through simulation in realistic noise and channel conditions. Results demonstrated the ability of the adaptive feedback system to increase throughput while meeting the same quality-of-service constraints as a static system. The advantage of L1-PCA over L2-PCA for processing outlier-prone data such as signals in warm coastal waters corrupted by impulsive noise (e.g. from snapping shrimp) was discussed. Simulation results demonstrated that a semi-blind (with only one pilot bit for phase correction) system employing a receiver based on L1-PCA will approach the performance of a pilot-based receiver.

Several conclusions drawn from the work in this dissertation can be applied towards new efforts. Software-defined radio is critical to wireless communications research as it allows for rapid technology development and prototyping moving all the way from simulation to hardware-in-the-loop testing in real RF environments. Modern commercial SDR platforms offer varied processing options and most applications can benefit from a heterogeneous approach leveraging the advantages of both GPPs and FPGAs. Care should be taken in the design of practical radio functionalities (e.g. synchronization) that are often overlooked in high-level design but are crucial to system performance. Considerations should be made towards control information exchange requirements including the routes and medium used and the impact of control overhead on system performance. As proven in this dissertation, cross-layer optimization can yield significant performance benefits. When designing for extreme communication scenarios, the unique challenges of the environment should be considered during problem formulation: whether it's impulsive noise from snapping shrimp or strong physical-layer interference from external sources. Digital signal processing for communication is most effective when algorithms are designed to adapt to changing conditions thereby balancing the trade-off between maximizing efficiency and maintaining connectivity.

Though this dissertation discussed communication in three unique environments: air, underwater, and space, the work presented here shares common themes applicable to communication system design as a whole. In conclusion, the flexibility of software-defined radio paired with adaptive and intelligent algorithms can enable communications in environments where inflexible static systems fail making the design of efficient and robust communication systems capable of supporting the next generation of wireless communications possible.

Appendix A

Proof of Equation (3.33)

Consider the positive semidefinite channel-processed autocorrelation matrix $\mathbf{P}_s \in \mathbb{C}^{L\times L}$. Dropping the subscript for simplicity, the matrix can be written as $\mathbf{P} = \Re\{\mathbf{P}\} + \mathrm{j}\Im\{\mathbf{P}\}$.

The imaginary part of any complex Hermitian matrix is a skew-symmetric matrix, thus $\Im\{\mathbf{P}\} = -\Im\{\mathbf{P}\}^T$. For any binary vector $\mathbf{s} \in \left\{\pm 1/\sqrt{L}\right\}^L$ it holds that

$$\mathbf{s}^T\Im\{\mathbf{P}\}\mathbf{s} = \mathbf{s}^T\Im\{\mathbf{P}\}^T\mathbf{s} = -\mathbf{s}^T\Im\{\mathbf{P}\}\mathbf{s} \tag{A.1}$$

therefore

$$\mathbf{s}^T\Im\{\mathbf{P}\}\mathbf{s} = 0. \tag{A.2}$$

The real part of any complex Hermitian matrix is a symmetric matrix. As such we can write in quadratic form

$$\mathbf{s}^T\mathbf{P}\mathbf{s} = \mathbf{s}^T\Re\{\mathbf{P}\}\mathbf{s} = \sum_{l=1}^{L}\sum_{k=1}^{L} s[l]s[k]\left[\Re\{\mathbf{P}\}\right]_{k,l} \tag{A.3}$$

or equivalently

$$\mathbf{s}^T\mathbf{P}\mathbf{s} = \frac{1}{L}\operatorname{Tr}\left(\Re\left\{\mathbf{P}\right\}\right) + \sum_{k} 2s[k]\left(\sum_{l>k} s[l]\Re\left\{[\mathbf{P}]_{k,l}\right\}\right). \tag{A.4}$$

Bibliography

[1] G. Sklivanitis, A. Gannon, S. N. Batalama, and D. A. Pados, “Addressing next-generation wireless challenges with commercial software-defined radio platforms,” *IEEE Commun. Mag.*, vol. 54, no. 1, pp. 59–67, Jan. 2016, ©2016 IEEE. Reprinted with permission.

[2] G. Sklivanitis *et al.*, “Airborne cognitive networking: design, development, and deployment,” *IEEE Access*, 2018, to appear, ©2018 IEEE. Reprinted with permission.

[3] A. Gannon, S. Balakrishnan, G. Sklivanitis, D. A. Pados, and S. N. Batalama, “Short data record filtering for adaptive underwater acoustic communications,” in *Proc. IEEE Sensor Array and Multichannel Signal Processing Workshop (SAM)*, Sheffield, England, Jul. 2018, pp. 316 – 320, ©2018 IEEE. Reprinted with permission.

[4] P. Jacob, R. P. Sirigina, A. S. Madhukumar, and V. A. Prasad, “Cognitive radio for aeronautical communications: A survey,” *IEEE Access*, vol. 4, pp. 3417–3443, 2016.

[5] R. Seker, M. Moallemi, J. Yapp, M. Towhidnejad, and R. Klein, “Performance issues in aircraft access to the national airspace swim program,” in *Proc. Integrated Commun. Navigation Surveillance Conf. (ICNS)*, Apr. 2014, pp. D3–1–D3–9.

[6] Y. Saleem, M. H. Rehmani, and S. Zeadally, “Integration of cognitive radio technology with unmanned aerial vehicles: Issues, opportunities, and future research challenges,” *J. Netw. Comput. Appl.*, vol. 50, no. Supplement C, pp. 15 – 31, 2015.

[7] L. Ribeiro, S. Giles, R. Katkin, T. Topiwala, and M. Minnix, “Challenges and opportunities to integrate UAS in the national airspace system,” in *Proc. Integrated Commun. Navigation Surveillance Conf. (ICNS)*, Apr. 2017, pp. 6C3–1–6C3–13.

[8] Y. Zeng, R. Zhang, and T. J. Lim, “Wireless communications with unmanned aerial vehicles: Opportunities and challenges,” *IEEE Commun. Mag.*, vol. 54, no. 5, pp. 36–42, May 2016.

[9] K. J. Kwak *et al.*, “Airborne network evaluation: Challenges and high fidelity emulation solution,” *IEEE Commun. Mag.*, vol. 52, no. 10, pp. 30–36, Oct. 2014.

[10] R. B. Wynn *et al.*, “Autonomous underwater vehicles (AUVs): Their past, present and future contributions to the advancement of marine geoscience,” *Marine Geology*, vol. 352, pp. 451 – 468, 2014.

[11] E. Bernard, F. Gonzàlez, C. Meinig, and H. Milburn, “Early detection and real-time reporting of deep-ocean tsunamis,” in *Proc. Int. Tsunami Symp.*, Seattle, WA, Aug. 2001, pp. 97–108.

[12] J. C. Ho and A. M. Michalak, “Challenges in tracking harmful algal blooms: A synthesis of evidence from lake erie,” *J. Great Lakes Res.*, vol. 41, no. 2, pp. 317 – 325, 2015.

[13] M. Stojanovic and J. Preisig, “Underwater acoustic communication channels: Propagation models and statistical characterization,” *IEEE Commun. Mag.*, vol. 47, no. 1, pp. 84–89, 2009.

[14] C. Henry. (2017, Oct.) SpaceX, OneWeb detail constellation plans to Congress. SpaceNews. [Online]. Available: http://spacenews.com/spacex-oneweb-detail-constellation-plans-to-congress/

[15] R. Radhakrishnan *et al.*, “Survey of inter-satellite communication for small satellite systems: Physical layer to network layer view,” *IEEE Commun. Surveys Tuts.*, vol. 18, no. 4, pp. 2442–2473, 2016.

[16] C. D. Edwards, M. Denis, and L. Braatz, “Operations concept for a solar system internetwork,” in *Proc. IEEE Aerosp. Conf.*, Mar. 2011, pp. 1–9.

[17] A. D. Panagopoulos, P.-D. M. Arapoglou, and P. G. Cottis, “Satellite communications at Ku, Ka, and V bands: Propagation impairments and mitigation techniques,” *IEEE Commun. Surveys Tuts.*, vol. 6, no. 3, pp. 2–14, 2004.

[18] W. Tang, P. Thompson, and B. Evans, “Frequency band sharing between satellite and terrestrial fixed links in the Ka band: A database approach,” *Proc. IEEE Int. Conf. Commun. (ICC)*, pp. 1–8, 2015.

[19] S. Burleigh *et al.*, “Delay-tolerant networking: an approach to interplanetary internet,” *IEEE Commun. Mag.*, vol. 41, no. 6, pp. 128–136, Jun. 2003.

[20] J. Mitola, “Software radio architecture,” *IEEE Commun. Mag.*, vol. 33, no. 5, pp. 26–38, May 1995.

[21] J. Mitola and G. Maguire, “Cognitive radio: making software radios more personal,” *IEEE Personal Commun. Mag.*, vol. 6, no. 4, pp. 13–18, 1999.

[22] S. Haykin, “Cognitive radio: brain-empowered wireless communications,” *IEEE J. Sel. Areas Commun.*, vol. 23, no. 2, pp. 201–220, Feb. 2005.

[23] J. Mitola, *Cognitive Radio Architecture: The Engineering Foundations of Radio XML.* Hoboken, NJ: Wiley, 2006.

[24] L. Ding *et al.*, “All-spectrum cognitive networking through joint distributed channelization and routing,” *IEEE Trans. Wireless Commun.*, vol. 12, no. 11, pp. 5394–5405, Nov. 2013.

[25] A. Goldsmith, S. Jafar, I. Maric, and S. Srinivasa, “Breaking spectrum gridlock with cognitive radios: An information theoretic perspective,” *Proc. IEEE*, vol. 97, no. 5, pp. 894–914, May 2009.

[26] G. Sklivanitis, “Software-defined architectures for spectrally efficient cognitive networking in extreme environments,” Ph.D. dissertation, State University of New York at Buffalo, 2017.

[27] D. Estathiou, J. Fridman, and Z. Zvonar, “Recent developments in enabling technologies for software defined radio,” *IEEE Commun. Mag.*, vol. 37, no. 8, pp. 112–117, Aug. 1999.

[28] T. Rondeau, N. McCarthy, and T. O’Shea, “SIMD programming in GNU radio: Maintainable and user-friendly algorithm optimization with VOLK,” in *Proc. Wireless Innov. Forum Conf. Commun. Technol. Softw. Defined Radio (WInnComm SDR)*, Jan. 2013, pp. 101–110.

[29] C. Moy and M. Raulet, “High-level design methodology for ultra-fast software defined radio prototyping on heterogeneous platforms,” *Advances Electron. Telecommun.*, vol. 1, no. 1, pp. 67–85, Apr. 2010.

[30] J. Malsbury and M. Ettus, “Simplifying FPGA design with a novel network-on-chip architecture,” in *Proc. Workshop Software Radio Implementation Forum (SRIF)*, 2013, pp. 45–52.

[31] R. Etkin, A. Parekh, and D. Tse, “Spectrum sharing for unlicensed bands,” in *Proc. IEEE Int. Symp. New Frontiers Dynamic Spectrum Access Netw. (DySPAN)*, 2005, pp. 251–258.

[32] M. Song, C. Xin, Y. Zhao, and X. Cheng, “Dynamic spectrum access: from cognitive radio to network radio,” *IEEE Wireless Commun.*, vol. 19, no. 1, pp. 23–29, Feb. 2012.

[33] G. Ganesan and Y. Li, “Cooperative spectrum sensing in cognitive radio networks,” in *Proc. IEEE Int. Symp. New Frontiers Dynamic Spectrum Access Netw. (DySPAN)*, 2005, pp. 137–143.

[34] N. Devroye, M. Vu, and V. Tarokh, “Cognitive radio networks,” *IEEE Signal Process. Mag.*, vol. 25, no. 6, pp. 12–23, Nov. 2008.

[35] R. Rajbanshi, A. M. Wyglinski, and G. J. Minden, “An efficient implementation of NC-OFDM transceivers for cognitive radios,” in *Proc. Int. Conf. Cognitive Radio Oriented Wireless Netw. Commun. (CROWNCOM)*, Jun. 2006, pp. 1–5.

[36] K. Gao, S. N. Batalama, D. A. Pados, and J. D. Matyjas, “Cognitive code-division channelization,” *IEEE Trans. Wireless Commun.*, vol. 10, no. 4, pp. 1090–1097, Apr. 2011.

[37] Y. Zhao *et al.*, “Applying radio environment maps to cognitive wireless regional area networks,” in *Proc. IEEE Int. Symp. New Frontiers Dynamic Spectrum Access Netw. (DySPAN)*, Apr. 2007, pp. 115–118.

[38] W. Su, J. D. Matyjas, and S. Batalama, “Active cooperation between primary users and cognitive radio users in heterogeneous ad-hoc networks,” *IEEE Trans. Signal Process.*, vol. 60, no. 4, pp. 1796–1805, Apr. 2012.

[39] M. D. Mueck, V. Frascolla, and B. Badic, “Licensed shared access - state-of-the-art and current challenges,” in *Proc. Int. Workshop Cognitive Cellular Systems (CCS)*, Sep. 2014, pp. 1–5.

[40] S. Haykin, D. Thomson, and J. Reed, “Spectrum sensing for cognitive radio,” *Proc. IEEE*, vol. 97, no. 5, pp. 849–877, May 2009.

[41] D. Teguig, B. Scheers, and V. L. Nir, “Data fusion schemes for cooperative spectrum sensing in cognitive radio networks,” in *Proc. Military Commun. Inform. Syst. Conf. (MCC)*, Oct. 2012, pp. 1–7.

[42] D. Gozupek, S. Bayhan, and F. Alagoz, “A novel handover protocol to prevent hidden node problem in satellite assisted cognitive radio networks,” in *Proc. Int. Symp. Wireless Pervasive Computing*, May 2008, pp. 693–696.

[43] C. Stevenson *et al.*, “IEEE 802.22: The first cognitive radio wireless regional area network standard,” *IEEE Commun. Mag.*, vol. 47, no. 1, pp. 130–138, Jan. 2009.

[44] J. Mitola, “Cognitive radio: An integrated agent architecture for software defined radio,” Ph.D. dissertation, KTH Royal Institute of Technology, 2000.

[45] S. Pattanayak, P. Venkateswaran, and R. Nandi, “Artificial neural networks for cognitive radio: A preliminary survey,” in *Proc. Int. Conf. Wireless Commun. Netw. Mobile Computing (WINCOM)*, Sep. 2012, pp. 1–4.

[46] T. O’Shea and J. Hoydis, “An introduction to deep learning for the physical layer,” *IEEE Trans. on Cogn. Commun. Netw.*, vol. 3, no. 4, pp. 563–575, Dec. 2017.

[47] P. Ferreira *et al.*, “Multi-objective reinforcement learning for cognitive radio–based satellite communications,” in *Proc. AIAA Int. Commun. Satellite Syst. Conf.*, Cleveland, OH, Oct. 2016.

[48] K.-L. A. Yau, P. Komisarczuk, and P. D. Teal, “Applications of reinforcement learning to cognitive radio networks,” in *Proc. IEEE Int. Conf. Commun. (ICC)*, May 2010, pp. 1–6.

[49] L. Ding, T. Melodia, S. N. Batalama, J. D. Matyjas, and M. J. Medley, "Cross-layer routing and dynamic spectrum allocation in cognitive radio ad hoc networks," *IEEE Trans. Veh. Technol.*, vol. 59, no. 4, pp. 1969–1979, May 2010.

[50] T. W. Rondeau, B. Le, D. Maldonado, D. Scaperoth, and C. W. Bostian, "Cognitive radio formulation and implementation," in *Proc. Int. Conf. Cognitive Radio Oriented Wireless Netw. Commun. (CROWNCOM)*, June 2006, pp. 1–10.

[51] M. J. Neely, E. Modiano, and C. E. Rohrs, "Dynamic power allocation and routing for time varying wireless networks," in *Proc. IEEE Conf. Computer Commun. (INFOCOM)*, vol. 1, Mar. 2003, pp. 745–755.

[52] L. Tassiulas and A. Ephremides, "Stability properties of constrained queueing systems and scheduling policies for maximum throughput in multihop radio networks," *IEEE Trans. Autom. Control*, vol. 37, no. 12, pp. 1936–1948, Dec. 1992.

[53] A. Kansal, S. N. Batalama, and D. A. Pados, "Adaptive maximum SINR RAKE filtering for DS-CDMA multipath fading channels," *IEEE J. Sel. Areas Commun.*, vol. 16, no. 9, pp. 1765–1773, Dec. 1998.

[54] G. Sklivanitis *et al.*, "All-spectrum cognitive channelization around narrowband and wideband primary stations," in *Proc. IEEE Global Commun. Conf. (GLOBECOM)*, Dec. 2015, pp. 1–7.

[55] T. Clancy and W. Arbaugh, "Measuring interference temperature," in *Proc. Virginia Tech. MPRG Symp. Wireless Personal Commun. (MPRG)*, Jun. 2006.

[56] G. N. Karystinos and D. A. Pados, "Adaptive assignment of binary user spreading codes in DS-CDMA systems," in *Proc. SPIE*, vol. 4395, 2001.

[57] C. W. Sung and H. Y. Kwan, "Heuristic algorithms for binary sequence assignment in DS-CDMA systems," in *Proc. IEEE Annu. Int. Symp. Personal, Indoor, Mobile Radio Commun. (PIMRC)*, vol. 5, Sep. 2002, pp. 2327–2331.

[58] G. N. Karystinos and D. A. Pados, "Rank-2-optimal adaptive design of binary spreading codes," *IEEE Trans. Inf. Theory*, vol. 53, no. 9, pp. 3075–3080, Sep. 2007.

[59] P. P. Markopoulos, S. Kundu, S. Chamadia, and D. A. Pados, "Efficient L1-norm principal-component analysis via bit flipping," *IEEE Trans. Signal Process.*, vol. 65, no. 16, pp. 4252–4264, Aug. 2017.

[60] S. Kundu, P. P. Markopoulos, and D. A. Pados, "Fast computation of the L1-principal component of real-valued data," in *Proc IEEE Int. Conf. Acoustics, Speech, Signal Process. (ICASSP)*, May 2014, pp. 8028–8032.

[61] Z. Liu and D. A. Pados, "LDPC codes from generalized polygons," *IEEE Trans. Inf. Theory*, vol. 51, no. 11, pp. 3890–3898, Nov. 2005.

[62] G. Foschini and M. Gans, "On limits of wireless communications in a fading environment when using multiple antennas," *Wireless Pers. Commun.*, vol. 6, no. 3, pp. 311–335, 1998.

[63] A. Moustakas, S. Simon, and A. Sengupta, "MIMO capacity through correlated channels in the presence of correlated interferers and noise: A (not so) large N analysis," *IEEE Trans. Inf. Theory*, vol. 49, no. 10, pp. 2545–2561, Oct. 2003.

[64] D. Gesbert, H. Bolcskei, D. Gore, and A. Paulraj, "Outdoor MIMO wireless channels: models and performance prediction," *IEEE Trans. Commun.*, vol. 50, no. 12, pp. 1926–1934, Dec. 2002.

[65] A. Hedayat, H. Shah, and A. Nosratinia, "Analysis of space-time coding in correlated fading channels," *IEEE Trans. Wireless Commun.*, vol. 4, no. 6, pp. 2882–2891, Nov. 2005.

[66] J. Akhtar and D. Gesbert, "Spatial multiplexing over correlated MIMO channels with a closed-form precoder," *IEEE Trans. Wireless Commun.*, vol. 4, no. 5, pp. 2400–2409, Sep. 2005.

[67] B. Lu, X. Wang, and K. Narayanan, "LDPC-based space-time coded OFDM systems over correlated fading channels: Performance analysis and receiver design," *IEEE Trans. Commun.*, vol. 50, no. 1, pp. 74–88, 2002.

[68] V. Tarokh, H. Jafarkhani, and A. Calderbank, "Space-time block coding for wireless communications: performance results," *IEEE J. Sel. Areas Commun.*, vol. 17, no. 3, pp. 451–460, Mar. 1999.

[69] R. Chen, J. Andews, and R. Health, "Multiuser space-time block coded MIMO with downlink precoding," in *Proc. IEEE Int. Conf. Commun. (ICC)*. IEEE, 2004, pp. 2689–2693.

[70] S. Serbetli and A. Yener, "MIMO-CDMA systems: signature and beamformer design with various levels of feedback," *IEEE Trans. Signal Process.*, vol. 54, no. 7, pp. 2758–2772, Jul. 2006.

[71] P. Amihood, E. Masry, L. B. Milstein, and J. G. Proakis, "Performance analysis of high data rate MIMO systems in frequency-selective fading channels," *IEEE Trans. Inf. Theory*, vol. 53, no. 12, pp. 4615–4627, Dec. 2007.

[72] J. Ahrenholz, C. Danilov, T. R. Henderson, and J. H. Kim, "CORE: A real-time network emulator," in *Proc. IEEE Military Commun. Conf. (MILCOM)*, Nov. 2008, pp. 1–7.

[73] J. Ahrenholz, T. Goff, and B. Adamson, "Integration of the CORE and EMANE network emulators," in *Proc. IEEE Military Commun. Conf. (MILCOM)*, Nov. 2011, pp. 1870–1875.

[74] B. Newton, J. Aikat, and K. Jeffay, "Simulating large-scale airborne networks with NS-3," in *Proc. Workshop NS-3 (WNS3)*, May 2015, pp. 32–39.

[75] J. Modares, N. Mastronarde, and K. Dantu, "UB-ANC emulator: An emulation framework for multi-agent drone networks," in *Proc. IEEE Int. Conf. Simulation, Modeling, Programming Autonomous Robots (SIMPAR)*, Dec. 2016, pp. 252–258.

[76] T. X. Brown, B. Argrow, C. Dixon, and S. Doshi, "Ad hoc UAV ground network (AUGNet)," in *Proc. AIAA 3rd "Unmanned Unlimited" Tech. Conf., Workshop and Exhibit*, 2004, pp. 29–39.

[77] M. Hoyhtya *et al.*, "Spectrum occupancy measurements: A survey and use of interference maps," *IEEE Commun. Surveys Tuts.*, vol. 18, no. 4, pp. 2386–2414, 2016.

[78] E. W. Frew and T. X. Brown, "Airborne communication networks for small unmanned aircraft systems," *Proc. IEEE*, vol. 96, no. 12, pp. 2008–2027, Dec. 2008.

[79] I. F. Akyildiz, W.-Y. Lee, and K. R. Chowdhury, "CRAHNs: Cognitive radio ad hoc networks," *Ad Hoc Netw.*, vol. 7, no. 5, pp. 810–836, Jul. 2009.

[80] A. Bagwari and G. S. Tomar, "Comparison between adaptive double-threshold based energy detection and cyclostationary detection technique for cognitive radio networks," in *Proc. Int. Conf. and Computational Intelligence Commun. Netw.*, Sep. 2013, pp. 182–185.

[81] C. Wietfeld and K. Daniel, "Cognitive networking for UAV swarms," *Handbook of Unmanned Aerial Vehicles*, pp. 749–780, 2015.

[82] G. Ding *et al.*, "An amateur drone surveillance system based on the cognitive internet of things," *IEEE Commun. Mag.*, vol. 56, no. 1, pp. 29–35, Jan. 2018.

[83] M. E. Tanab and W. Hamouda, "Resource allocation for underlay cognitive radio networks: A survey," *IEEE Commun. Surveys Tuts.*, vol. 19, no. 2, pp. 1249–1276, 2017.

[84] Y. Wang, "Cognitive radio for aeronautical air-ground communication," in *Proc. IEEE/AIAA Digital Avionics Syst. Conf.*, Oct. 2008, pp. 2.B.4–1–2.B.4–8.

[85] J. Kakar and V. Marojevic. (2017) Waveform and spectrum management for unmanned aerial systems beyond 2025. ArXiv preprint. [Online]. Available: http://arxiv.org/abs/1708.01664

[86] H. Ghazzai, M. B. Ghorbel, A. Kadri, M. J. Hossain, and H. Menouar, "Energy-efficient management of unmanned aerial vehicles for underlay cognitive radio systems," *IEEE Trans. Green Commun. Netw.*, vol. 1, no. 4, pp. 434–443, Dec. 2017.

[87] R. Fantacci and A. Tani, "Performance evaluation of a spectrum-sensing technique for cognitive radio applications in B-VHF communication systems," *IEEE Trans. Veh. Technol.*, vol. 58, no. 4, pp. 1722–1730, May 2009.

[88] S. Chandrasekharan *et al.*, "Designing and implementing future aerial communication networks," *IEEE Commun. Mag.*, vol. 54, no. 5, pp. 26–34, May 2016.

[89] M. Li *et al.*, "Cognitive code-division links with blind primary-system identification," *IEEE Trans. Wireless Commun.*, vol. 10, no. 11, pp. 3743–3753, Nov. 2011.

[90] N. Janatian, S. Sun, and M. Modarres-Hashemi, "Joint optimal spectrum sensing and power allocation in CDMA-based cognitive radio networks," *IEEE Trans. Veh. Technol.*, vol. 64, no. 9, pp. 3990–3998, Sep. 2015.

[91] Y. Xu, X. Zhao, and Y. C. Liang, "Robust power control and beamforming in cognitive radio networks: A survey," *IEEE Commun. Surveys Tuts.*, vol. 17, no. 4, pp. 1834–1857, 2015.

[92] Y. Noam and A. J. Goldsmith, "Blind null-space learning for MIMO underlay cognitive radio with primary user interference adaptation," *IEEE Trans. Wireless Commun.*, vol. 12, no. 4, pp. 1722–1734, Apr. 2013.

[93] B. Gopalakrishnan and N. D. Sidiropoulos, "Cognitive transmit beamforming from binary CSIT," *IEEE Trans. Wireless Commun.*, vol. 14, no. 2, pp. 895–906, Feb. 2015.

[94] V. Chakravarthy *et al.*, "Novel overlay/underlay cognitive radio waveforms using SD-SMSE framework to enhance spectrum efficiency - Part I: Theoretical framework and analysis in AWGN channel," *IEEE Trans. Commun.*, vol. 57, no. 12, pp. 3794–3804, Dec. 2009.

[95] F. Jasbi and D. K. C. So, "Hybrid overlay/underlay cognitive radio network with MC-CDMA," *IEEE Trans. Veh. Technol.*, vol. 65, no. 4, pp. 2038–2047, Apr. 2016.

[96] M. Cesana, F. Cuomo, and E. Ekici, "Routing in cognitive radio networks: Challenges and solutions," *Ad Hoc Netw.*, vol. 9, no. 3, pp. 228 – 248, 2011.

[97] Q. Zhu, Z. Yuan, J. B. Song, Z. Han, and T. Basar, "Interference aware routing game for cognitive radio multi-hop networks," *IEEE J. Sel. Areas Commun.*, vol. 30, no. 10, pp. 2006–2015, Nov. 2012.

[98] Y. Liu, L. X. Cai, and X. S. Shen, "Spectrum-aware opportunistic routing in multi-hop cognitive radio networks," *IEEE J. Sel. Areas Commun.*, vol. 30, no. 10, pp. 1958–1968, Nov. 2012.

[99] S. Ping, A. Aijaz, O. Holland, and A. H. Aghvami, "SACRP: A spectrum aggregation-based cooperative routing protocol for cognitive radio ad-hoc networks," *IEEE Trans. Commun.*, vol. 63, no. 6, pp. 2015–2030, Jun. 2015.

[100] M. Zareei *et al.*, “On-demand hybrid routing for cognitive radio ad-hoc network,” *IEEE Access*, vol. 4, pp. 8294–8302, Nov. 2016.

[101] F. Tang and J. Li, “Joint rate adaptation, channel assignment and routing to maximize social welfare in multi-hop cognitive radio networks,” *IEEE Trans. Wireless Commun.*, vol. 16, no. 4, pp. 2097–2110, Apr. 2017.

[102] T. R. Newman, S. M. S. Hasan, D. Depoy, T. Bose, and J. H. Reed, “Designing and deploying a building-wide cognitive radio network testbed,” *IEEE Commun. Mag.*, vol. 48, no. 9, pp. 106–112, Sep. 2010.

[103] D. Raychaudhuri *et al.*, “Overview of the ORBIT radio grid testbed for evaluation of next-generation wireless network protocols,” in *Proc. IEEE Wireless Commun. Netw. Conf. (WCNC)*, vol. 3, Mar. 2005, pp. 1664–1669.

[104] M. Danieletto, G. Quer, R. R. Rao, and M. Zorzi, “CARMEN: A cognitive networking testbed on android OS devices,” *IEEE Commun. Mag.*, vol. 52, no. 9, pp. 98–107, Sep. 2014.

[105] R. Iwata, V. Va, K. Sakaguchi, and K. Araki, “Experiment on MIMO cognitive radio using tx/rx beamforming,” in *Proc. IEEE Annu. Int. Symp. Personal, Indoor, Mobile Radio Commun. (PIMRC)*, Sep. 2013, pp. 2871–2875.

[106] R. Zhou *et al.*, “Software defined radio implementation of SMSE based overlay cognitive radio,” in *Proc. IEEE Int. Symp. New Frontiers Dynamic Spectrum Access Netw. (DySPAN)*, Apr. 2010, pp. 1–2.

[107] P. Rose *et al.*, “Demonstration of hybrid overlay/underlay waveform generator with spectrally compliant cognitive capability via SD-SMSE framework,” in *Proc. IEEE Consumer Commun. Netw. Conf. (CCNC)*, Jan. 2016, pp. 258–259.

[108] G. Nychis, R. Chandra, T. Moscibroda, I. Tashev, and P. Steenkiste, “Reclaiming the white spaces: Spectrum efficient coexistence with primary users,” in *Proc. Seventh Conf. Emerging Networking Experiments and Technologies (CoNEXT)*, 2011, pp. 1:1–1:12.

[109] H. Rahul, N. Kushman, D. Katabi, C. Sodini, and F. Edalat, “Learning to share: Narrowband-friendly wideband networks,” in *Proc. Conf. Data Commun. (SIGCOMM)*, 2008, pp. 147–158.

[110] K. Hong, S. Sengupta, and R. Chandramouli, “SpiderRadio: A cognitive radio implementation using IEEE 802.11 components,” *IEEE Trans. Mobile Comput.*, vol. 12, no. 11, pp. 2105–2118, Nov. 2013.

[111] L. Ding *et al.*, “Software-defined joint routing and waveform selection for cognitive ad hoc networks,” in *Proc. IEEE Military Commun. Conf. (MILCOM)*, Oct. 2010, pp. 1454–1459.

[112] S. Soltani *et al.*, "Distributed cognitive radio network architecture, SDR implementation and emulation testbed," in *Proc. IEEE Military Commun. Conf. (MILCOM)*, Oct. 2015, pp. 438–443.

[113] L. Sun, W. Zheng, N. Rawat, V. Sawant, and D. Koutsonikolas, "Performance comparison of routing protocols for cognitive radio networks," *IEEE Trans. Mobile Comput.*, vol. 14, no. 6, pp. 1272–1286, Jun. 2015.

[114] A. R. Syed *et al.*, "Route selection for multi-hop cognitive radio networks using reinforcement learning: An experimental study," *IEEE Access*, vol. 4, pp. 6304–6324, 2016.

[115] S. W. Huang, G. Sklivanitis, D. A. Pados, and S. N. Batalama, "Underwater acoustic communications using quasi-orthogonal chirps," in *Proc. Asilomar Conf. Signals, Syst., and Comput.*, Oct. 2017, pp. 1749–1753.

[116] F. Wunsch, H. Jakel, and F. K. Jondral, "Performance evaluation of IEEE 802.15.4 OQPSK and CSS PHY in the presence of interference," in *Proc. IEEE 82nd Veh. Techn. Conf. (VTC Fall)*, Sep. 2015, pp. 1–5.

[117] E. Demirors, G. Sklivanitis, T. Melodia, and S. N. Batalama, "RcUBe: Real-time reconfigurable radio framework with self-optimization capabilities," in *Proc. 12th Annu. IEEE Int. Conf. Sens., Commun., Netw. (SECON)*, Jun. 2015, pp. 28–36.

[118] G. N. Karystinos and D. A. Pados, "The maximum squared correlation, sum capacity, and total asymptotic efficiency of minimum total-squared-correlation binary signature sets," *IEEE Trans. Inf. Theory*, vol. 51, no. 1, pp. 348–355, Jan. 2005.

[119] I. F. Akyildiz, D. Pompili, and T. Melodia, "Underwater acoustic sensor networks: Research challenges," *Ad hoc networks*, vol. 3, no. 3, pp. 257–279, 2005.

[120] T. Melodia, H. Kulhandjian, L.-C. Kuo, and E. Demirors, "Advances in underwater acoustic networking," *Mobile Ad Hoc Networking: Cutting Edge Directions*, vol. 852, 2013.

[121] M. Stojanovic, "Acoustic (underwater) communications," in *Encyclopedia of Telecommunications*. Wiley, 2003.

[122] R. J. Urick, *Principles of Underwater Sound*, 3rd ed. McGraw-Hill, 1983.

[123] J. R. Potter, L. T. Wei, and M. Chitre, "High-frequency ambient noise in warm shallow waters," in *Sea Surface Sound*, Jul. 1997.

[124] E. M. Sozer, M. Stojanovic, and J. G. Proakis, "Underwater acoustic networks," *IEEE J. Ocean. Eng.*, vol. 25, no. 1, pp. 72–83, 2000.

[125] G. Sklivanitis, E. Demirors, S. N. Batalama, T. Melodia, and D. A. Pados, "Receiver configuration and testbed development for underwater cognitive channelization," in *Proc. Asilomar Conf. Signals, Systems, and Computers*, 2014, pp. 1594–1598.

[126] R. Diamant and L. Lampe, "Low probability of detection for underwater acoustic communication: A review," *IEEE Access*, vol. 6, pp. 19 099–19 112, 2018.

[127] B. Tomasi, G. Toso, P. Casari, and M. Zorzi, "Impact of time-varying underwater acoustic channels on the performance of routing protocols," *IEEE J. Ocean. Eng.*, vol. 38, no. 4, pp. 772–784, 2013.

[128] D. A. Pados and G. N. Karystinos, "An iterative algorithm for the computation of the MVDR filter," *IEEE Trans. Signal Process.*, vol. 49, no. 2, pp. 290–300, 2001.

[129] L. Wan *et al.*, "Adaptive modulation and coding for underwater acoustic OFDM," *IEEE J. Ocean. Eng.*, vol. 40, no. 2, pp. 327–336, Apr. 2015.

[130] R. Ahmed and M. Stojanovic, "Joint power and rate control for packet coding over fading channels," *IEEE J. Ocean. Eng.*, vol. 42, no. 3, pp. 697–710, Jul. 2017.

[131] A. Radosevic, R. Ahmed, T. M. Duman, J. G. Proakis, and M. Stojanovic, "Adaptive OFDM modulation for underwater acoustic communications: Design considerations and experimental results," *IEEE J. Ocean. Eng.*, vol. 39, no. 2, pp. 357–370, Apr. 2014.

[132] E. Demirors, G. Sklivanitis, G. E. Santagati, T. Melodia, and S. N. Batalama, "Design of a software-defined underwater acoustic modem with real-time physical layer adaptation capabilities," in *Proc. Int. Conf. Underwater Netw. Syst. (WUWNet)*, 2014, pp. 25:1–25:8.

[133] ——, "A high-rate software-defined underwater acoustic modem with real-time adaptation capabilities," *IEEE Access*, vol. 6, pp. 18 602–18 615, 2018.

[134] M. Stojanovic, "Acoustic communication," in *Springer Handbook of Ocean Engineering.* Springer, 2016, ch. 15, pp. 359–386.

[135] S. Haykin, *Adaptive Filter Theory*, 3rd ed. Prentice Hall, 2002.

[136] E. J. Kelly, "An adaptive detection algorithm," *IEEE Trans. Aerosp. Electron. Syst.*, vol. 22, no. 2, pp. 115–127, Mar. 1986.

[137] H. Qian and S. N. Batalama, "Data record-based criteria for the selection of an auxiliary vector estimator of the MMSE/MVDR filter," *IEEE Trans. Commun.*, vol. 51, no. 10, pp. 1700–1708, 2003.

[138] P. Qarabaqi and M. Stojanovic, "Acoustic channel modeling and simulation," [Online]. Available: http://millitsa.coe.neu.edu/?q=projects.

[139] ——, “Statistical characterization and computationally efficient modeling of a class of underwater acoustic communication channels,” *IEEE J. Ocean. Eng.*, vol. 38, no. 4, pp. 701–717, 2013.

[140] P. J. Bouvet, Y. Auffret, and C. Aubry, “On the analysis of orthogonal chirp division multiplexing for shallow water underwater acoustic communication,” in *Proc. OCEANS Conf.*, Jun. 2017, pp. 1–5.

[141] M. Versluis, B. Schmitz, A. von der Heydt, and D. Lohse, “How snapping shrimp snap: Through cavitating bubbles,” *Science*, vol. 289, no. 5487, pp. 2114–2117, 2000.

[142] W. W. L. Au and K. Banks, “The acoustics of the snapping shrimp synalpheus parneomeris in kaneohe bay,” *The Journal of the Acoustical Society of America*, vol. 103, no. 1, pp. 41–47, 1998.

[143] D. H. Cato and M. J. Bell, “Ultrasonic ambient noise in australian shallow waters at frequencies up to 200 kHz,” MRL Technical Report MRL-TR-91-23, Materials Research Laboratory, Australia, Tech. Rep., Feb. 1992.

[144] M. A. Chitre, J. R. Potter, and S. H. Ong, “Optimal and near-optimal signal detection in snapping shrimp dominated ambient noise,” *IEEE J. Ocean. Eng.*, vol. 31, no. 2, pp. 497–503, Apr. 2006.

[145] N. Tsagkarakis, P. P. Markopoulos, G. Sklivanitis, and D. A. Pados, “L1-norm principal-component analysis of complex data,” *IEEE Trans. Signal Process.*, vol. 66, no. 12, pp. 3256–3267, Jun. 2018.

[146] M. W. Legg, “Non-gaussian and non-homogeneous poisson models of snapping shrimp noise,” Ph.D. dissertation, Curtin University of Technology, Faculty of Science and Engineering, Department of Imaging and Applied Physics., 2010.

[147] M. Chitre, “Underwater acoustic communications in warm shallow water channels,” Ph.D. dissertation, Dept. of Electrical and Computer Engineering, National University of Singapore, 2006.

[148] A. Mahmood and M. Chitre, “Modeling colored impulsive noise by markov chains and alpha-stable processes,” in *Proc. OCEANS Conf.*, May 2015.

[149] K. Pelekanakis and M. Chitre, “Robust equalization of mobile underwater acoustic channels,” *IEEE J. Ocean. Eng.*, vol. 40, no. 4, pp. 775–784, Oct. 2015.

[150] A. Mahmood, H. Vishnu, and M. Chitre, “Model-based signal detection in snapping shrimp noise,” in *Proc. IEEE Underwater Commun. Netw. Conf. (UComms)*, Aug. 2016, pp. 1–5.

[151] A. Mahmood and M. Chitre, "Uncoded acoustic communication in shallow waters with bursty impulsive noise," in *Proc. IEEE Underwater Commun. Netw. Conf. (UComms)*, Aug. 2016, pp. 1–5.

[152] J. P. Nolan, *Stable Distributions - Models for Heavy Tailed Data*. Boston: Birkhauser, 2018, in progress, Chapter 1 online at http://fs2.american.edu/jpnolan/www/stable/stable.html.

[153] M. Veillette, "Alpha-stable distributions in matlab," [Online]. Available: http://math.bu.edu/people/mveillet/html/alphastablepub.html.

[154] G. H. Golub and C. F. VanLoan, *Matrix Computations*, 3rd ed. Baltimore, MD: The Johns Hopkins University Press, 1996.

[155] P. P. Markopoulos, G. N. Karystinos, and D. A. Pados, "Some options for L1-subspace signal processing," in *Proc. Int. Symp. Wireless Commun. Syst. (ISWCS)*, Aug. 2013, pp. 1–5.

[156] ——, "Optimal algorithms for L1-subspace signal processing," *IEEE Trans. Signal Process.*, vol. 62, no. 19, pp. 5046–5058, Oct. 2014.

[157] A. Gannon, S. Balakrishnan, and G. Sklivanitis, "Auxiliary-vector based short data record filtering for underwater acoustic communications," [Online]. Available: https://github.com/adamgann/av-uwa.

[158] K. McCarthy, F. Stocklin, B. Geldzahler, D. Friedman, and P. Celeste, "NASA's evolution to Ka-band space communications for near-earth spacecraft," in *Proc. AIAA SpaceOps Conf.*, Reston, VA, Apr. 2010.

[159] N. L. Gallou and D. Mignolo, "Beyond Ka-band: Leveraging Q/V band to ensure the provision and future growth of broadband satellite communications," in *Proc. IET Seminar Beyond Ka-Band*, Nov. 2011, pp. 1–58.

[160] Y. Niu, Y. Li, D. Jin, L. Su, and A. V. Vasilakos, "A survey of millimeter wave communications (mmWave) for 5G: opportunities and challenges," *Wireless Netw.*, vol. 21, no. 8, pp. 2657–2676, Nov. 2015.

[161] H. Heidt, J. Puig-Suari, A. Moore, S. Nakasuka, and R. Twiggs, "Cubesat: A new generation of picosatellite for education and industry low-cost space experimentation," *AIAA/USU Conf. Small Satellites*, Aug. 2000.

[162] Z. Qu, G. Zhang, H. Cao, and J. Xie, "LEO satellite constellation for internet of things," *IEEE Access*, vol. 5, pp. 18 391–18 401, 2017.

[163] S. Nag, C. K. Gatebe, and O. de Weck, "Observing system simulations for small satellite formations estimating bidirectional reflectance," *Int. J. Appl. Earth Observation Geoinformation*, vol. 43, pp. 102–118, Dec. 2015.

[164] J. Mukherjee and B. Ramamurthy, “Communication technologies and architectures for space network and interplanetary internet,” *IEEE Commun. Surveys Tuts.*, vol. 15, no. 2, pp. 881–897, 2013.

[165] M. Hoyhtya *et al.*, “Database-assisted spectrum sharing in satellite communications: A survey,” *IEEE Access*, vol. 5, 2017.

[166] S. K. Sharma, S. Chatzinotas, and B. Ottersten, “Satellite cognitive communications: Interference modeling and techniques selection,” in *Proc. 6th Advanced Satellite Multimedia Systems Conference (ASMS) and 12th Signal Processing for Space Communications Workshop (SPSC)*, Sep. 2012, pp. 111–118.

[167] F. Vatalaro, G. Corazza, C. Caini, and C. Ferrarelli, “Analysis of LEO, MEO, and GEO global mobile satellite systems in the presence of interference and fading,” *IEEE J. Sel. Areas Commun.*, vol. 13, no. 2, pp. 291–300, 1995.

[168] S. K. Sharma, S. Chatzinotas, and B. Ottersten, “In-line interference mitigation techniques for spectral coexistence of GEO and NGEO satellites,” *Int. J. Satellite Commun. Netw.*, vol. 34, no. 1, pp. 11–39, Jan. 2016.

[169] M. Williamson, “Connecting the other three billion,” *Engineering & Technology*, vol. 4, no. 4, pp. 70–73, Feb. 2009.

[170] H. D. Curtis, *Orbital Mechanics for Engineering Students.* Elsevier, 2014.

[171] D. Bell *et al.*, “MRO relay telecom support of mars science laboratory surface operations,” in *Proc. IEEE Aerosp. Conf.*, Mar. 2014, pp. 1–10.

[172] ITU-R, “Radio Regulations, Volume 1,” 2016.

[173] *Digital Video Broadcasting (DVB); Second generation framing structure, channel coding and modulation systems for Broadcasting, Interactive Services, News Gathering and other broadband satellite applications; Part 1: DVB-S2*, European Telecommunications Standards Institute Std. ETSI EN 302 307-1, Rev. 1.4.1, 2014.

[174] *Digital Video Broadcasting (DVB); Second generation framing structure, channel coding and modulation systems for Broadcasting, Interactive Services, News Gathering and other broadband satellite applications; Part 2: DVB-S2 Extensions (DVB-S2X)*, European Telecommunications Standards Institute Std. ETSI EN 302 307-2, Rev. 1.1.1, 2014.

[175] P. Chini, G. Giambene, and S. Kota, “A survey on mobile satellite systems,” *Int. J. Satellite Commun. Netw.*, vol. 28, no. 1, pp. 29–57, 2009.

[176] E. G. Cuevas and V. Weerackody, “Technical characteristics and regulatory challenges of communications satellite earth stations on moving platforms,” *Johns Hopkins APL Technical Digest*, vol. 33, no. 1, pp. 37–51, 2015.

[177] K. Leveque, J. Puig-Suari, and C. Turner, "Global educational network for satellite operations (GENSO)," *AIAA/USU Conf. Small Satellites*, Aug. 2007.

[178] D. J. White *et al.*, "SatNOGS: Satellite networked open ground station," *Engineering Faculty Publications*, 2015. [Online]. Available: https://scholar.valpo.edu/engineering_fac_pub/40

[179] S. Maleki, S. Chatzinotas, J. Krause, K. Liolis, and B. Ottersten, "Cognitive zone for broadband satellite communications in 17.3-17.7 GHz band," *IEEE Wireless Commun. Lett.*, vol. 4, no. 3, pp. 305–308, Jun. 2015.

[180] E. Lagunas, S. K. Sharma, S. Maleki, S. Chatzinotas, and B. Ottersten, "Resource allocation for cognitive satellite communications with incumbent terrestrial networks," *IEEE Trans. on Cogn. Commun. Netw.*, vol. 1, no. 3, pp. 305–317, sep 2015.

[181] E. Lagunas *et al.*, "Power and rate allocation in cognitive satellite uplink networks," in *Proc. IEEE Int. Conf. Commun. (ICC)*, May 2016, pp. 1–6.

[182] V. Weerackody, "Spectrum sharing of VMES terminals with fixed service stations," in *Proc. IEEE Military Commun. Conf. (MILCOM)*, 2016, pp. 612–617.

[183] S. Chatzinotas *et al.*, "Cognitive approaches to enhance spectrum availability for satellite systems," *Int. J. Satellite Commun. Netw.*, vol. 35, no. 5, pp. 407–442, Sep. 2017.

[184] S. Maleki *et al.*, "Cognitive spectrum utilization in Ka band multibeam satellite communications," *IEEE Commun. Mag.*, vol. 53, no. 3, pp. 24–29, Mar. 2015.

[185] A. Pourmoghadas, S. K. Sharma, S. Chatzinotas, and B. Ottersten, "On the spectral coexistence of GSO and NGSO FSS systems: power control mechanisms and a methodology for inter-site distance determination," *Int. J. Satellite Commun. Netw.*, vol. 35, no. 5, pp. 443–459, Sep. 2017.

[186] M. Jia, X. Liu, Z. Yin, Q. Guo, and X. Gu, "Joint cooperative spectrum sensing and spectrum opportunity for satellite cluster communication networks," *Ad Hoc Netw.*, vol. 58, pp. 231–238, Apr. 2017.

[187] M. Hoyhtya, "Secondary terrestrial use of broadcasting satellite services below 3 GHz," *Int. Journal Wireless Mobile Netw.*, vol. 5, no. 1, pp. 1–14, 2013.

[188] M. A. Clark and K. Psounis, "Equal interference power allocation for efficient shared spectrum resource scheduling," *IEEE Trans. Wireless Commun.*, vol. 16, no. 1, pp. 58–72, Jan. 2017.

[189] M. Hoyhtya, "Frequency sharing between FSS and BSS satellites in the 17.3–18.4 GHz band," in *Proc. Advances Wireless Optical Commun. (RTUWO)*, Nov. 2015, pp. 176–179.

[190] ERC/DEC/(00)07, “The shared use of the band 17.7-19.7 GHz by the fixed service and earth stations of the fixed-satellite service,” 2000.

[191] K. Liolis *et al.*, “Cognitive radio scenarios for satellite communications: The CoRaSat approach,” in *Proc. Future Netw. Mobile Summit*, Jul. 2013, pp. 1–10.

[192] S. Tani *et al.*, “An adaptive beam control technique for Q band satellite to maximize diversity gain and mitigate interference to terrestrial networks,” *IEEE Trans. Emerg. Topics Comput.*, 2017.

[193] E. Dahlman *et al.*, “5G wireless access: requirements and realization,” *IEEE Commun. Mag.*, vol. 52, no. 12, pp. 42–47, Dec. 2014.

[194] F. Guidolin and M. Nekovee, “Investigating spectrum sharing between 5G millimeter wave networks and fixed satellite systems,” in *Proc. IEEE Global Commun. Conf. (GLOBECOM)*, Dec. 2015, pp. 1–7.

[195] M. Hoyhtya, “Sharing FSS satellite C band with secondary small cells and D2D communications,” in *Proc. IEEE Int. Conf. Commun. (ICC)*, Jun. 2015, pp. 1606–1611.

[196] Federal Communications Commission, “Coordination procedures in the 1695–1710 MHz and 1755–1780 MHz bands,” 2014.

[197] S. Vassaki, M. I. Poulakis, A. D. Panagopoulos, and P. Constantinou, “Power allocation in cognitive satellite terrestrial networks with QoS constraints,” *IEEE Commun. Lett.*, vol. 17, no. 7, pp. 1344–1347, Jul. 2013.

[198] X. Artiga *et al.*, “Spectrum sharing in hybrid terrestrial-satellite backhaul networks in the Ka band,” in *Proc. European Conf. Netw. and Commun. (EuCNC)*, Jun. 2017, pp. 1–5.

[199] S. Kandeepan, L. De Nardis, M.-G. Di Benedetto, A. Guidotti, and G. E. Corazza, “Cognitive satellite terrestrial radios,” in *Proc. IEEE Global Commun. Conf. (GLOBECOM)*, Dec. 2010, pp. 1–6.

[200] Y. Feng, B. Jiao, and L. Song, “Satellite-based spectrum sensing for dynamic spectrum sharing in ground-located CRNs,” *Wireless Personal Commun.*, vol. 57, no. 1, pp. 105–117, Mar. 2011.

[201] C. Yuan, M. Lin, J. Ouyang, and Y. Bu, “Beamforming schemes for hybrid satellite-terrestrial cooperative networks,” *Int. Journal Electron. Commun.*, vol. 69, no. 8, pp. 1118–1125, Aug. 2015.

[202] J. Downey, D. Mortensen, M. Evans, J. Briones, and N. Tollis, “Adaptive coding and modulation experiment using NASA’s space communication and navigation testbed,” in *Proc. AIAA Int. Commun. Satellite Syst. Conf.*, Cleveland, OH, Oct. 2016.

[203] G. J. Mendis, J. Wei, and A. Madanayake, "Deep belief network for automated modulation classification in cognitive radio," in *Proc. Cognitive Commun. Aerosp. Appl. Workshop*, Jun. 2017, pp. 1–5.

[204] P. V. R. Ferreira, R. Metha, and A. M. Wyglinski, "Cognitive radio-based geostationary satellite communications for Ka-band transmissions," in *Proc. IEEE Global Conf. Signal Inform. Process. (GlobalSIP)*, Dec. 2014, pp. 1093–1097.

[205] F. Walter and M. Feldmann, "Dynamic discovery of ground stations in ring road networks," in *Proc. IEEE Int. Conf. Wireless Space Extreme Environments (WiSEE)*, Sep. 2016, pp. 93–98.

[206] G. J. Clark, W. Eddy, S. K. Johnson, D. E. Brooks, and J. L. Barnes, "Architecture for cognitive networking within NASA's future space communications infrastructure," in *Proc. AIAA Int. Commun. Satellite Syst. Conf.*, Cleveland, OH, Oct. 2016.

[207] R. Dudukovich, A. Hylton, and C. Papachristou, "A machine learning concept for DTN routing," in *Proc. IEEE Int. Conf. Wireless Space Extreme Environments (WiSEE)*, Oct. 2017, pp. 110–115.

[208] J. Barnes and W. Eddy, "Machine learning for space communications service management tasks," in *Proc. Cognitive Commun. Aerosp. Appl. Workshop*, Jun. 2017, pp. 1–4.

[209] M. Matinmikko *et al.*, "Overview and comparison of recent spectrum sharing approaches in regulation and research: From opportunistic unlicensed access towards licensed shared access," in *Proc. IEEE Int. Symp. New Frontiers Dynamic Spectrum Access Netw. (DySPAN)*, Apr. 2014, pp. 92–102.

[210] S. K. Sharma, S. Chatzinotas, and B. Ottersten, "Cognitive beamhopping for spectral coexistence of multibeam satellites," *Int. J. Satellite Commun. Netw.*, vol. 33, no. 1, pp. 69–91, 2015.

[211] J. Anzalchi *et al.*, "Beam hopping in multi-beam broadband satellite systems: System simulation and performance comparison with non-hopped systems," in *Proc. 5th Advanced Satellite Multimedia Syst. Conf. and 11th Signal Process. Space Commun. Workshop*, Sep. 2010, pp. 248–255.

[212] *Prediction procedure for the evaluation of interference between stations on the surface of the Earth at frequencies above about 0.1 GHz*, ITU-R Std. P.452-16, 2015.

[213] X. Zhu *et al.*, "Resource allocation in spectrum-sharing cloud based integrated terrestrial-satellite network," *Proc. 13th Int. Wireless Commun. Mobile Computing Conf. (IWCMC)*, pp. 334–339, 2017.

[214] S. K. Sharma, S. Chatzinotas, and B. Ottersten, "Transmit beamforming for spectral coexistence of satellite and terrestrial networks," in *Proc. Int. Conf. Cognitive Radio Oriented Wireless Netw. Commun. (CROWNCOM)*, Jul. 2013, pp. 275–281.

[215] L. Yu, Q. Wang, Y. Guo, and P. Li, "Spectrum availability prediction in cognitive aerospace communications: A deep learning perspective," in *Proc. Cognitive Commun. Aerosp. Appl. Workshop*, Jun. 2017, pp. 1–4.

[216] Y. Shi and Y. E. Sagduyu, "Spectrum learning and access for cognitive satellite communications under jamming," in *Proc. IEEE Conf. Commun. Netw. Security (CNS)*, Oct. 2016, pp. 472–479.

[217] S. K. Sharma, S. Chatzinotas, and B. Ottersten, "Spectrum sensing in dual polarized fading channels for cognitive SatComs," in *Proc. IEEE Global Commun. Conf. (GLOBECOM)*, Dec. 2012, pp. 3419–3424.

[218] ——, "Exploiting polarization for spectrum sensing in cognitive satcoms," in *Proc. Int. Conf. Cognitive Radio Oriented Wireless Netw. Commun. (CROWNCOM)*, Jun. 2012, pp. 36–41.

[219] S. K. Sharma, S. Maleki, S. Chatzinotas, J. Grotz, and B. Ottersten, "Implementation issues of cognitive radio techniques for Ka-band (17.7 - 19.7 GHz) SatComs," in *Proc. 7th Advanced Satellite Multimedia Syst. Conf. and 13th Signal Process. Space Commun. Workshop (ASMS/SPSC)*, Sep. 2014, pp. 241–248.

[220] S. Maleki *et al.*, "Cognitive radio for Ka band satellite communications," in *Proc. AIAA Int. Commun. Satellite Syst. Conf.*, San Diego, CA, Aug. 2014.

[221] Y. H. Yun and J. H. Cho, "An orthogonal cognitive radio for a satellite communication link," in *Proc. IEEE Annu. Int. Symp. Personal, Indoor, Mobile Radio Commun. (PIMRC)*, Sep. 2009, pp. 3154–3158.

[222] B. M. Khan, M. Mustaqim, B. A. Khawaja, and S. ShabeehUlHusnain, "Spectrum sensing in satellite cognitive radios: Blind signal detection technique," *Microwave Optical Technol. Lett.*, vol. 58, no. 6, pp. 1377–1384, Jun. 2016.

[223] F. Dimc, G. Baldini, and S. Kandeepan, "Experimental detection of mobile satellite transmissions with cyclostationary features," *Int. J. Satellite Commun. Netw.*, vol. 33, no. 2, pp. 163–183, Mar. 2015.

[224] V. Icolari, A. Guidotti, D. Tarchi, and A. Vanelli-Coralli, "An interference estimation technique for satellite cognitive radio systems," in *Proc. IEEE Int. Conf. Commun. (ICC)*, Jun. 2015, pp. 892–897.

[225] M. López-Benítez and F. Casadevall, "Improved energy detection spectrum sensing for cognitive radio," *IET Commun.*, vol. 6, no. 8, p. 785, 2012.

[226] Y. C. Liang, Y. Zeng, E. C. Y. Peh, and A. T. Hoang, "Sensing-throughput tradeoff for cognitive radio networks," *IEEE Trans. Wireless Commun.*, vol. 7, no. 4, pp. 1326–1337, Apr. 2008.

[227] R. Tandra and A. Sahai, "SNR walls for signal detection," *IEEE J. Sel. Topics Signal Process.*, vol. 2, no. 1, pp. 4–17, Feb. 2008.

[228] *Procedure for determining if coordination is required between geostationary-satellite networks sharing the same frequency bands*, ITU-R Std. S.738, 1992.

[229] P.-D. Arapoglou *et al.*, "MIMO over satellite: A review," *IEEE Commun. Surveys Tuts.*, vol. 13, no. 1, pp. 27–51, 2011.

[230] W. M. Jang, "Blind cyclostationary spectrum sensing in cognitive radios," *IEEE Commun. Lett.*, vol. 18, no. 3, pp. 393–396, Mar. 2014.

[231] W. A. Gardner, A. Napolitano, and L. Paura, "Cyclostationarity: Half a century of research," *Signal Process.*, vol. 86, no. 4, pp. 639 – 697, 2006.

[232] F. Li, Z. Li, G. Li, F. Dong, and W. Zhang, "Efficient wideband spectrum sensing with maximal spectral efficiency for LEO mobile satellite systems," *Sensors*, vol. 17, no. 1, p. 193, Jan. 2017.

[233] I. F. Akyildiz, B. F. Lo, and R. Balakrishnan, "Cooperative spectrum sensing in cognitive radio networks: A survey," *Physical Commun.*, vol. 4, no. 1, pp. 40–62, Mar. 2011.

[234] S. Bayhan, G. Gur, and F. Alagoz, "Satellite assisted spectrum agility concept," in *Proc. IEEE Military Commun. Conf. (MILCOM)*, Oct. 2007, pp. 1–7.

[235] S. Shellhammer and G. Chouinard, "Spectrum sensing requirements summary," IEEE, Tech. Rep. 802.22-06/0089, 2006.

[236] K. Schraml, A. Narbudowicz, S. Chalermwisutkul, D. Heberling, and M. J. Ammann, "Easy-to-deploy LC-loaded dipole and monopole antennas for cubesat," in *Proc. 11th European Conf. on Antennas Propagation (EUCAP)*, Mar. 2017, pp. 2303–2306.

[237] *UHF Antenna*, Endurosat, 2017, rev 1.3. [Online]. Available: https://www.endurosat.com/products/cubesat-uhf-antenna/

[238] A. Nascetti, E. Pittella, P. Teofilatto, and S. Pisa, "High-gain S-band patch antenna system for earth-observation cubesat satellites," *IEEE Antennas Wireless Propag. Lett.*, vol. 14, pp. 434–437, 2015.

[239] E. Pittella *et al.*, "Reconfigurable S-band patch antenna system for cubesat satellites," *IEEE Aerosp. Electron. Syst. Mag.*, vol. 31, no. 5, pp. 6–13, May 2016.

[240] "Norad two-line element sets current data," CelesTrak. [Online]. Available: https://www.celestrak.com/NORAD/elements/

[241] O. Dobre, A. Abdi, Y. Bar-Ness, and W. Su, "Survey of automatic modulation classification techniques: classical approaches and new trends," *IET Commun.*, vol. 1, no. 2, p. 137, 2007.

[242] A. Smith, M. Evans, and J. Downey, "Modulation classification of satellite communication signals using cumulants and neural networks," in *Proc. Cognitive Commun. Aerosp. Appl. Workshop*, Jun. 2017, pp. 1–8.

[243] V. Gouldieff, J. Palicot, and S. Daumont, "Blind modulation classification for cognitive satellite in the spectral coexistence context," *IEEE Trans. Signal Process.*, vol. 65, no. 12, pp. 3204–3217, Jun. 2017.

[244] ——, "Blind digital modulation classification based on M-th power nonlinear transformation," in *Proc. IEEE Global Conf. Signal Inform. Process. (GlobalSIP)*, Dec. 2016, pp. 650–654.

[245] M. M. Hamidi, W. W. Edmonson, and F. Afghah, "A non-cooperative game theoretic approach for power allocation in intersatellite communication," in *Proc. IEEE Int. Conf. Wireless Space Extreme Environments (WiSEE)*, Oct. 2017, pp. 13–18.

[246] *Propagation data required for the evaluation of coordination distances in the frequency range 100 MHz to 105 GHz*, ITU-R Std. P.620-7, 2017.

[247] V. Icolari, D. Tarchi, A. Guidotti, and A. Vanelli-Coralli, "Genetic inspired scheduling algorithm for cognitive satellite systems," in *Proc. IEEE Int. Conf. Commun. (ICC)*, May 2016, pp. 1–6.

[248] S. Liu, X. Hu, and W. Wang, "Deep reinforcement learning based dynamic channel allocation algorithm in multibeam satellite systems," *IEEE Access*, vol. 6, pp. 15 733–15 742, 2018.

[249] S. K. Sharma *et al.*, "Joint carrier allocation and beamforming for cognitive SatComs in Ka-band (17.3–18.1 GHz)," in *Proc. IEEE Int. Conf. Commun. (ICC)*, Jun. 2015, pp. 873–878.

[250] M. Murroni, V. Popescu, M. Fadda, and D. Giusto, "Robust multi-rate modulation for cognitive radio communications over land mobile satellite channel at Ku-band," *Int. J. Satellite Commun. Netw.*, vol. 35, no. 5, pp. 503–515, Sep. 2017.

[251] P. V. R. Ferreira *et al.*, "Multi-objective reinforcement learning for cognitive satellite communications using deep neural network ensembles," *IEEE J. Sel. Areas Commun.*, vol. 36, no. 5, pp. 1030–1041, 2018.

[252] T. M. Hackett, S. G. Bilen, P. V. R. Ferreira, A. M. Wyglinski, and R. C. Reinhart, "Implementation of a space communications cognitive engine," in *Proc. Cognitive Commun. Aerosp. Appl. Workshop*, Jun. 2017, pp. 1–7.

[253] M. Littman and J. Boyan, "A distributed reinforcement learning scheme for network routing," Carnegie Mellon University, Pittsburgh, PA, USA, Tech. Rep., 1993.

[254] C. J. Roberts, M. Morgenstern, D. J. Israel, J. M. Borky, and T. H. Bradley, "Preliminary results from a model-driven architecture methodology for development of an event-driven space communications service concept," in *Proc. IEEE Int. Conf. Wireless Space Extreme Environments (WiSEE)*, Oct. 2017, pp. 122–127.

[255] M. Banko and E. Brill, "Scaling to very very large corpora for natural language disambiguation," in *Proc.39th Annu. Meeting Assoc. Computational Linguistics (ACL)*, 2001, pp. 26–33.

[256] A. Halevy, P. Norvig, and F. Pereira, "The unreasonable effectiveness of data," *IEEE Intell. Syst.*, vol. 24, no. 2, pp. 8–12, Mar. 2009.

[257] R. C. Reinhart and J. P. Lux, "Space-based reconfigurable software defined radio test bed aboard international space station," in *Proc. AIAA SpaceOps Conf.*, Pasadena, CA, May 2014, pp. 1–11.

[258] D. J. Israel, "Next-generation NASA earth-orbiting relay satellites: Fusing microwave and optical communications," in *Proc. IEEE Aerosp. Conf.*, Big Sky, MT, Mar. 2018.

[259] H. Kaushal and G. Kaddoum, "Optical communication in space: Challenges and mitigation techniques," *IEEE Commun. Surveys Tuts.*, vol. 19, no. 1, pp. 57–96, 2017.

[260] A. Mansour, R. Mesleh, and M. Abaza, "New challenges in wireless and free space optical communications," *Optics Lasers Eng.*, vol. 89, pp. 95 – 108, 2017.